ON LARGE EDDY SIMULATIONS OF REACTING TWO-PHASE FLOWS

A Thesis

Presented to

The Academic Faculty

by

Sreekanth Pannala

In Partial Fulfillment

of the Requirements for the Degree

Doctor of Philosophy in Aerospace Engineering

Georgia Institute of Technology

May, 2000

ON LARGE EDDY SIMULATIONS OF REACTING TWO-PHASE FLOWS

Approved:

_____

Suresh Menon, Chairman

_____

Jerry Seitzman

_____

Lakshmi N. Sankar

_____

Jeff Jagoda

_____

Marc Smith

Date Approved by Chairman _____

Dedicated to

my mother Chandrakala, my father Narayan Reddy

and

my sister Sreemala and brother Sreedhar

for their constant support and inspiration

ACKNOWLEDGMENTS

I would like to thank several people who helped me to complete this thesis. Dr. Suresh Menon was very enthusiastic about this research project, and allowed me to work on "real world" problems. My sincere thanks for all the guidance he has provided me over the course of my study. Dr. Jerry Seitzman, Dr. Jeff Jagoda, Dr. Lakshmi N. Sankar, and Dr. Marc Smith, who served on my various committees provided invaluable suggestions and recommendations which gave me new perspectives on my research.

I would like to thank Dr. Kalyan Chakravarthy, Dr. Tom Smith, Dr. Won-Wook Kim, Dr. Srinivasan Arunajatesan, Dr. Rajendran Mohanraj, Dr. Junxiao Wu, Dr. Christopher Nelson, Dr. William H. Calhoun, Dr. Graham M. Goldin, Dr. R. K. Thulasiram, Dr. Rabindra Paul, Vaidyanathan Sankaran, Christopher Stone, William Henry, Yongzhong Sun, Bin Yang, Wenzhong Gao, Hongjuan Wang - former and present members of Computational Combustion Laboratory (CCL) at Georgia Tech, who worked with me on various projects and made my work days interesting and educational. Special thanks to the faculty and students of the School of Aerospace Engineering for introducing me to the wonderful area of computational combustion and for supporting my research. My thanks are also due to wonderful colleagues at Oak Ridge National Labs (ORNL), where I worked over the last year. Without their support and constant inspiration, it would have been extremely difficult to finish this thesis.

My family has been a constant source of support and encouragement. Special thanks to Sreemala, my sister, who was with me every step during the crucial phase of

this journey and also made my stay at Georgia Tech comfortable. Last but not the least, I would like to thank all my friends who have helped me at various stages. I will remember times spent with them fondly.

TABLE OF CONTENTS

LIST OF TABLES

LIST OF ILLUSTRATIONS

NOMENCLATURE

Roman Symbols

B_M	Spalding Number
C_D	Drag Coefficient
D	Mass diffusion
D_k	Dissipation term of k^{sgs}
D(k)	Dissipation spectrum
D_{sm}	Mixture diffusion coefficient
d	Diameter
E	Total internal energy
E(k)	Energy spectrum
e	Internal energy
F_k	Contribution to k^{sgs} due to coupling force term $\dot{F}_{s,\,i}$
$\dot{F}_{s,\,i}$	Volume averaged rate of exchange of momentum
f(*l*)	Length scale pdf
H	Total enthalphy
h	Heat transfer coefficient
k^{sgs}	Subgrid kinetic energy
l	Eddy size

l_{LEM}	Characteristic subgrid length scale
m	Mass
N	Total number of species
Nu	Nusselt Number
P_k	Production term of k^{sgs}
Pr	Gas-phase Prandtl Number
p	Kinematic Pressure
p	Thermodynamic pressure
$\dot{Q}_s$	Volume averaged rate of exchange of energy
R	Gas constant
Re_{LEM}	Subgrid Reynolds Number
$R_{Lp,i}$	Particle auto-correlation coefficient
Re_p	Droplet Reynolds Number
R_u	Universal gas constant
S	Source terms
Sc	Schmidt Number
S_L	Source term to the subgrid gas-phase equations from Lagrangian tracking scheme
S_{ij}	Resolved rate-of-strain tensor
St	Stokes Number
S_ψ	Source term due to vaporization of the liquid phase

S_1	Source term to the LEM void fraction equation from Lagrangian tracking scheme
S_2	Source term from the subgrid vaporization
s	1D domain of LEM
T	Temperature
T_k	Transport term of k^{sgs}
T(k)	Transfer energy at wavenumber ’k’
u	velocity
u_i	Filtered LES velocity
u_i'	Gaussian random number multiplied by the fluctuating velocity
u_p	Particle velocity
V	Volume
v	Particle velocity
W_α	Species molecular weight
Y	Species concentration
$Y_{i,\alpha}$	Species velocity correlations
$Y_{s,F}$	Fuel mass fraction at the droplet interface
Y_α	Filtered species mass fraction
$Y_{\infty, F}$	Fuel mass fraction in the ambient gas

Greek Symbols

Δ	Grid scale
ΔU	Velocity difference between the upper and lower stream
δ_ω	Vorticity thickness
δ_L	0.1-0.9 Level thickness
ε	Turbulent dissipation energy
η	Kolmogorov scale
κ	Thermal conductivity
λ	Void fraction of the liquid
Λ	LEM event frequency parameter
μ	Viscosity
ν	Kinematic viscosity
ρ	Density
ρ_p	Particle density
ρ_s	Gas mixture density
$\dot{\rho}_s$	Volume averaged rate of exchange of mass
ν_t	Eddy viscosity
φ	Volume fraction of the gas phase
τ	Variable denoting time
τ_{ij}	Stress term

$\bar{\tau}_{ij}$	Resolved viscous stress tensor
τ_e	Eddy turn over time
τ_p	Particle response time
Ψ	Scalar mass fraction
$\overline{\dot{\omega}_\alpha}$	LES filtered species mass production term

Subscripts

avg	Average
i, j, k, l	Cartesian tensor indices
g	Gas phase
l	Liquid phase
max	Maximum
p	Droplet properties
s	Surface of the droplet
$Re_p = 0$	Quiescent conditions

Superscripts

sgs	Subgrid scale
n	Time step index

Other Symbols

δ	Partial derivative
∇	Gradient
$\nabla \times \nabla$	Cross product
~	Favre spatial/time filter
_	Mixture averaged
$\sum$	Summation
$\prod$	Product

Abbreviations

1D	One dimension
2D	Two dimensions
3D	Three dimensions
CPU	Central processing unit
CDM	Continuous droplet model
CFM	Continuous formulation method
CFD	Computational fluid dynamics
CFL	Courant-Fridrichs-Levy Number
DDM	Discrete droplet model
DNS	Direct numerical simulation

GEAE	General Electric aircraft engines
ICE	Internal combustion engines
LES	Large eddy simulation
LEM	Linear eddy model
LHF	Locally homogenous flow
MURI	Multi-university research initiative
NIST	National institute of standards and technology
pdf	Probability density function
SF	Separated flow
SGI	Silicon graphics
SLOR	Successive line over relaxation
SMD	Sauter mean diameter
SPM	Single phase model
SSF	Stochastic separated flow model

SUMMARY

A two-phase subgrid combustion model has been formulated for large-eddy simulations (LES). This approach includes a more fundamental treatment of the effects of the final stages of droplet vaporization, molecular diffusion, chemical reactions and small scale turbulent mixing than other LES closure techniques. In this thesis, the liquid droplets are tracked using the Lagrangian approach up to a pre-specified cut-off size. The phase change of the droplets both larger and smaller than the cut-off size and the subsequent mixing of the evaporated fuel with the oxidizer are modeled within the subgrid using an Eulerian two-phase model.

Two-way coupling between the gas-phase and dispersed-phase quantities (both mean and fluctuating) have been extensively studied in isotropic turbulence. Comparisons between the DNS and LES have yielded better closures for the turbulence equations in presence of dispersed phase. Finally, the new model has been implemented into the LES code to simulate temporal and spatial shear layers, which are some of the basic building blocks in understanding the complex flow-phenomena in a realistic combustor. Studies on temporal mixing layers have shown that the droplets of Stokes number of order one disperse the most. These studies also suggest that the droplets generate substantial baroclinic torque and inhibit large scale vortical motions. It is shown here that the new subgrid approach works consistently better for both infinite and finite-

rate kinetics in turbulent mixing layer even when the cut-off is increased. In contrast, conventional LES under similar conditions results in significant error when the cut-off size is increased. The spatial shear layers studied also suggest that the droplets rearrange energy from large scale vortical structures to smaller scales and this process is closely related to the transfer of energy from large scales to the small scales as observed in isotropic turbulence. The spatial mixing layer simulations were compared to earlier experiments of Hishida *et al.* and very good agreement has been obtained. The sensitivity of the new subgrid two-phase approach to droplet cut-off size has also been evaluated in the spatial mixing layers.

CHAPTER I

INTRODUCTION

Combustion efficiency, reduced emissions and stable combustion in the lean limit are some of the desirable features in the next generation gas turbine engines. To achieve these capabilities, current research is focussing on improving the liquid fuel atomization process and to increase fuel-air mixing downstream of the fuel injector. To characterize the mixing process, the details at the small scales are needed. Experimental non-intrusive techniques have some inherent limitations in terms of resolving these small-scale details. For example, the near field of a liquid fuel injector has never been properly investigated due to difficulties in carrying out measurements in dense droplet regimes. Structure of complex three-dimensional, swirling fuel-air mixing layers is also very difficult to resolve using current experimental methods.

There are some characteristics of fuel atomization and fuel-air mixing in two-phase flows that makes numerical modeling very difficult. Some of them include the unsteadiness and the highly non-linear interactions at a wide range of time and spatial scales between the two phases. Conventional steady state methods cannot be used to elucidate the finer details of fuel atomization and fuel-air mixing because these processes are highly unsteady. On the other hand, although unsteady mixing process can be studied

quite accurately using direct numerical simulation (DNS) (e.g., [1]), application of DNS is limited to low to moderate Reynolds numbers (Re) due to resolution requirements. This restriction limits the extension of conclusions drawn from DNS results to high Reynolds number complex flows typical in gas turbine combustors.

An alternative approach called large-eddy simulation (LES) has the potential for application to high Re flows. In LES, the scales larger than the grid size are computed using a time- and space-accurate scheme, while the unresolved smaller scales, which are mostly isotropic, are modeled using an eddy viscosity based subgrid model. Closure of the momentum and kinetic energy transport equations can be achieved using this method since the small scales primarily provide a dissipative mechanism for the energy transferred from the large scales. However, for combustion to occur, the species must first undergo mixing and come into molecular contact. These processes occur at the small scales which are not resolved in conventional LES approach. As a result, conventional subgrid eddy diffusivity models cannot be used to model these features. Thus, the application of LES to reacting flows requires models that can capture accurately the effects of turbulent small-scale mixing and chemical reactions.

To address these issues, a subgrid combustion model was developed and implemented within the LES formulation recently [2] [3] [4] [5]. This model separately and simultaneously treats the physical processes of molecular diffusion and small scale turbulent convective stirring. This is in contrast to probability density function closure [6] [7] which phenomenologically treats these two processes by a single model, thereby removing experimentally observed [8] [9] [10] Schmidt number variation of the flow.

The capabilities of this model have been demonstrated in the above noted studies by carrying out quantitative comparison with high-Re experimental data obtained in reacting shear layers. Application of this method to premixed combustion has also been recently demonstrated [11] [12] [13]. Results show that this method can capture thin, high-Re turbulent flames without any numerical dissipation. The predicted turbulent flame speed was also shown to be in reasonable agreement with high-Re data.

LES has been used extensively for both reacting [14] [15] [16] [17] and non-reacting flows [18] [19] [20] [21] from its first introduction by Smagorinsky [22]. However only limited work has been done in terms of its applicability to two-phase flows [23] [24]. On the other hand, the steady state methods have been used to study two-phase flows (e.g. [25] [26]). Broadly speaking, spray modeling is classified into two categories as detailed in an excellent review on sprays by Faeth [27]:

1 Locally homogenous flow (LHF) models: In these models, the gas and the liquid phases are assumed to be in dynamic and thermodynamic equilibrium. This is a limiting case and can only represent spray containing infinitely small droplets. This is because at each point in the flow field, both phases are assumed to have the same velocity and temperature and be in phase equilibrium. The basic premise here is that the rates of transport between the phases are fast compared to the characteristics flow times. The use of this model implies that the process under consideration is mixing controlled. Usually this model is a good candidate for cases in which gas or vapor is the dispersed phase like in bubbly flows and is not generally used for spray modeling where the dispersed phase is liquid.

2 Separated flow (SF) models: The effects of finite rates of transport between the phases are considered in SF models. Most of the present day studies (e.g. [23] [24]) use these models, as they are generally needed for quantitative predictions of realistic sprays. Use of these methods requires accurate treatment of the finite rate exchange of mass, momentum and energy between the phases. Current models generally average over processes which occur on scales comparable to the drop size, i.e., no attempt is made to accurately model the details of the flow field around or within individual drops due to resource (CPU as well as memory) constraints. Usually these details are incorporated through empirical expressions for droplet drag, heat and mass transfer.

The separated flow models described above are further broadly divided into "discrete droplet model" (DDM), "continuous droplet model" (CDM) [29] and "continuous formulation method" (CFM). The DDM and CFM are most commonly used to model two-phase flows and are also popularly referred to as Lagrangian and Eulerian formulations for dispersed-phase respectively.

In the Eulerian formulation, the motion of drops and gas is treated as though they are inter-penetrating continua. Here, the governing equations for both the media are similar and very easy to model but it is very difficult to incorporate the effects of a range of droplet sizes. Also there are several issues concerning the implementation of boundary conditions and coupling terms that are difficult to resolve [30].

Eulerian and Lagrangian formulations have been used to simulate two-phase flows in the past (e.g., [24] [31]). Both methods have their own merits and drawbacks

[32]; however, most state-of-the-art codes employ the Lagrangian form to capture the droplet dynamics, while the gas phase is still computed in the Eulerian form (e.g., [33]). As mentioned before, in this formulation, the effects of finite rates of transport between the phases are explicitly included and thus it yields more accurate results as required for spray combustion applications. In this formulation, the droplets are tracked explicitly using Lagrangian equations of motion, and, heat and mass transfer are computed for each droplet. The mass, momentum and heat exchange terms are then calculated and explictly included in the gas-phase equations as source terms. Due to resource constraints (computer time and memory), only a limited range of droplet sizes are computed. Droplets below an *ad hoc* prespecified cut-off size are assumed to vaporize instantaneously and become fully mixed in the gas phase. For example, KIVA [33] is one of the most popular spray combustion code and the droplets in this code are assumed to instantaneously disappear if the droplet mass reduces by three orders of magnitude from the initial state. In ALLSPD3D [34], a general purpose spray combustion code, the droplets are assumed to instantaneously vaporize if the droplet size falls below 5 microns.

This is a critical assumption and flawed. It will be shown here that the small-scale mixing process is very important for quantitative predictions. The final stages of droplet vaporization and the subsequent mixing needs to be properly resolved for accurate prediction of the combustion process. In this thesis, the gas-phase subgrid combustion methodology has been extended to allow proper simulation of the final stages of droplet evaporation and turbulent mixing.

Successful application of LES to model two-phase flows involves including the

effects of turbulence on droplet properties and also the reverse effect of droplet drag and vaporization on turbulence. Also, how the two phases interact when heat release/absorption and chemical reactions occur, is equally important and much more difficult to model. The past LES studies of Oefelein and Yang [23] have included the effect of turbulence on droplet characteristics, but the opposite was neglected. Several studies (e.g., recent ones by Mashayek [35], Boivin *et al.* [36], Miller and Bellan [37]) have showed that droplet drag and vaporization can have significant effect in modifying some of the characteristics of turbulence. These studies and the earlier efforts [38]-[42] have shown that the presence of droplets increases the turbulent kinetic energy at the small scales which in turn can increase the dissipation rate. Since the small scales are not resolved in a typical LES, it is of interest to determine whether the important features of the droplet-turbulence interaction must be taken into account for accurate simulations. In light of these studies, additional effort is still required to characterize these interactions in order to develop closures for LES equations.

In order to address this problem, several DNS studies are carried out to characterize the effects of vaporizing sprays on gas-phase flows. The interaction between the droplets and gas-phase turbulence is analyzed using energy and dissipation spectra, particle-particle and fluid-particle Lagrangian correlations, and dispersion statistics. Large eddy simulations were then carried out and compared to DNS data to determine the important features of the interaction between the phases. The new two-phase subgrid model developed in this study has been extensively validated/evaluated and then used to study two-phase temporal and spatially evolving shear layers.

1.1 Objectives of the Current Study

The focus of the present research is to develop tools for LES of unsteady two-phase flows. Special emphasis is on developing subgrid scale models that accurately capture the complex physical processes such as droplet vaporization, fuel-air mixing etc., that occur prior to actual combustion process. These models developed to account for droplet-effects on the turbulent flow, result in a fully coupled approach to simulate two-phase turbulent reacting flows.

To summarize, the present thesis has the following objectives:

1 **Develop an accurate and relatively "inexpensive" two-phase LES model for spray combustion**.

Towards this extent a new model is developed here in which the droplets above the cut-off are tracked in the Lagrangian fashion in the supergrid while the droplets below the cut-off are modeled in the subgrid. New subgrid models are developed here to achieve this goal and are described in this thesis.

2 **Characterize the effect of small scale turbulence on droplet dispersion**.

DNS studies of two-phase flow in isotropic turbulence are carried out to analyze the effect of small scale turbulence on droplet properties such as particle dispersion, particle-particle correlations, particle-fluid correlations and relative velocities.

3 **Characterize turbulence modulation in the presence of both non-vaporizing and vaporizing droplets**.

Both DNS and LES studies of the isotropic turbulence is used to analyze the role of droplets on modulating turbulence. Closures and new scaling laws for subgrid modeling are arrived at from this study. The laws obtained are then implemented in the final numerical model to simulate the problems described below.

4 **Simulate typical flow problems**.

Mixing Layers - For the last decade or so, 2-D mixing layers have served as the standard experiment for understanding the dispersion of particles (e.g., [43] [44] and [45]). The present study not only supplements these studies by addressing three-dimensional issues but also deals with both vaporization, two-way momentum coupling and scalar mixing.

Spatial shear layers - These flows are essential building blocks in most practical combustors. Even though spatial shear layers are more physical, there are inherent problems in simulating these flows such as prescribing the complete inflow conditions, Sommerfeld [26]. The problem is magnified in case of two-phase flows, where, in addition to the gas-phase information, droplet size, droplet velocity, droplet velocity-size correlations etc., have to be prescribed.

1.2 Thesis Outline

The thesis begins with the development of LES models for two-phase flows in Chapter II. It is followed by details of the subgrid models in Chapter III. Specific emphasis is given to the liquid-phase formulations as the focus of this research is to

supplement the gas-phase LES research. In Chapter IV, the numerical implementation of the LES models is discussed. The modeling approach discussed in Chapter IV is then applied to both stationary and decaying isotropic turbulence and discussed in Chapter V. The results from the simulations of temporal mixing layers are given in Chapter VI where the new subgrid two-phase flow model is compared and contrasted with conventional modeling. Finally, a series of two-phase shear layer problems are simulated and discussed in chapter VII. This thesis ends with conclusions and recommendations in Chapter VIII.

CHAPTER II

LARGE EDDY SIMULATIONS

In LES, the scales larger than the grid size are computed using a time- and space-accurate scheme, while the unresolved smaller scales, which are mostly isotropic, are modeled using an eddy viscosity based subgrid model. LES has been used for both reacting [14] [15] [16] [17] and non-reacting flows [18] [21] since its first introduction by Smagorinsky [22].

In the present LES formulation, the two-phase approach is implemented within an Eulerian-Lagrangian approach. The gas or continuous phase equations are solved on an Eulerian grid while the droplets are tracked in a Lagrangian framework. The Lagrangian approach for dispersed phase is most suitable for very dilute flows (void fractions of dispersed phase less than few percent) and this is the case with most of the liquid-fueled combustors except for the near-injector region. In the conventional Lagrangian approach, the droplets below an *ad hoc* cut-off size are assumed to instantaneously vaporize and contribute to the gas-phase equations. In the present approach, droplets larger than the cut-off size are tracked as in the usual Lagrangian approach and therefore, heat and mass transfer are explicitly computed for each droplet (or group). Here, a droplet group represents a group of droplets with a representative size, temperature, spatial location and

velocity. The range of these droplet properties depends on the computational/accuracy requirements. In the rest of this thesis, the term “droplets” refers to “droplet groups” for convenience. However, once the droplets are smaller than the cut-off, a two-phase subgrid Eulerian model is employed to include the effects of the small droplets within the LES cells. In the present study, this new approach is implemented in a zero-Mach number LES code for application to low-speed (i.e., incompressible) flows. Also, this LES methodology has been extended to compressible flows [47] [48] for eventual application to combustion problems in realistic gas turbine combustors where acoustic wave motion strongly interacts with the shear flow and the unsteady combustion process.

2.1 Gas Phase LES Equations

The incompressible Navier Stokes equations in the zero-Mach number limit are employed for most of the studies in this thesis. Zero-Mach number approach uses a series expansion in terms of Mach number to remove the acoustic component from the equations and is a well established method ([12], [49]) and more details are given in appendix A. The important advantage using this approach is the ability to model most reactive flows with varying density with reasonably large time-steps. Since the acoustic component is decoupled, the time-step requirements are not governed by the speed of sound. The methods developed here are not however restricted to low compressibility. The zero-Mach number numerical framework was chosen to evaluate/validate the new model in an efficient manner. In this thesis, the zero-Mach number equations are

modified by the presence of the droplets and the detailed derivation is given in appendix A.

To summarize, LES mass, momentum, energy and species equations in the zero-Mach number limit in dimensional form are:

$$\frac{\partial \bar{\rho}}{\partial t} + \frac{\partial \bar{\rho} \tilde{u}_i}{\partial x_i} = \dot{\rho}_s \tag{2.1}$$

$$\frac{\partial \bar{\rho} \tilde{u}_i}{\partial t} + \tilde{u}_j \frac{\partial \bar{\rho} \tilde{u}_i}{\partial x_j} = -\tilde{u}_i \bar{\rho} \frac{\partial \tilde{u}_j}{\partial x_j} - \frac{\partial \bar{p}}{\partial x_i} + \mu \frac{\partial^2 \tilde{u}_i}{\partial x_k \delta x_k} + \frac{\partial \tau_{ij}^{sgs}}{\partial x_j} + \dot{F}_{s,i} \tag{2.2}$$

$$\frac{\partial \tilde{u}_j}{\partial x_j} = \frac{\gamma - 1}{\gamma p_0} \left[\frac{1}{\gamma - 1} \frac{\partial p_0}{\partial t} + \frac{1}{\gamma - 1} \frac{p_0 \dot{\rho}_s}{\bar{\rho}} - \dot{\rho}_s e_t + \kappa \frac{\partial^2 \tilde{T}}{\partial x_i \partial x_i} + \dot{Q}_s - \bar{\rho} \dot{F}_{s,i} \tilde{u}_i \right] \tag{2.3}$$

$$\frac{\partial \bar{\rho} \tilde{Y}_\alpha}{\partial t} + \frac{\partial \left[\bar{\rho} \tilde{Y}_\alpha \tilde{u}_i - \bar{\rho} \bar{D}_\alpha \frac{\partial \tilde{Y}_\alpha}{\partial x_i} + Y_{i,\alpha}^{sgs} \right]}{\partial x_i} = \overline{\dot{\omega}_\alpha} + \dot{S}_{s,\alpha} \qquad \alpha = 1, N-1 \tag{2.4}$$

In the above equations, the source terms $\dot{\rho}_s, \dot{F}_s, \dot{Q}_s$, and $\dot{S}_{s,\alpha}$ represent, respectively, the volume-averaged rate of exchange of mass, momentum, energy and

species between the gas and the liquid phase. These terms are computed as follows [23] [27] .

$$\begin{cases} \dot{\rho}_s = -\left[\rho_p \dfrac{dV_p}{dt} + V_p \dfrac{d\rho_p}{dt}\right]_{\Delta V} \\ \dot{F}_{s,i} = -\left[\left(\rho_p \dfrac{dV_p}{dt} + V_p \dfrac{d\rho_p}{dt}\right) u_{p,i} + \rho_p V_p \dfrac{du_{p,i}}{dt}\right]_{\Delta V} \\ \dot{Q}_s = -\left[\left(\rho_p \dfrac{dV_p}{dt} + V_p \dfrac{d\rho_p}{dt}\right) e_{t,p} + \rho_p V_p \dfrac{de_{t,p}}{dt}\right]_{\Delta V} \\ \dot{S}_{s,\alpha} = -\left[\left(\rho_p \dfrac{dV_p}{dt} + V_p \dfrac{d\rho_p}{dt}\right) Y_{\alpha,p} + \rho_p V_p \dfrac{dY_{\alpha,p}}{dt}\right]_{\Delta V} \end{cases} \tag{2.5}$$

Here, $[\ ]_{\Delta V}$ stands for averaging over all the LES cell volume. $\bar{\rho}, \tilde{u}_i, \tilde{Y}_\alpha$ and $\bar{p}$ are, respectively, the density, i-th velocity component, α-th species mass fraction and the kinematic pressure, and, p_0 is the thermodynamic pressure which varies from time-step to time-step while remaining constant over space. Also, ν, λ, D and R are, respectively, the kinematic viscosity, the thermal conductivity, the mass diffusion (assumed constant and same for all species here but can be generalized) and the gas constant. V_p, ρ_p, u_p, e_p, Y_p are volume, density, velocities, total energy and species concentration of the droplets respectively. Details of obtaining these quantities are discussed in section 2.2. In Eq. 2.4,

$\overline{\dot{\omega}_\alpha}$ is the LES filtered species production/destruction term.

The above system of equations is supplemented by the equation of state for the thermodynamic pressure $p_0 = \bar{\rho} R \tilde{T}$ which can be used to obtain the temperature $\tilde{T}$. Furthermore, note that Eq. 2.3 is the equivalent energy equation in the zero-Mach number limit. In the absence of heat release and no phase change, this equation and Eq. 2.1 will be identical.

In the above equations, the subgrid stress tensor $\tau_{ij}^{sgs} = -(\widetilde{u_i u_j} - \tilde{u}_i \tilde{u}_j)$ and the species-velocity correlations $Y_{j,\alpha}^{sgs} = -(\widetilde{Y_\alpha u_j} - \tilde{Y}_\alpha \tilde{u}_j)$ require modeling. In the present LES approach, the subgrid stress term τ_{ij}^{sgs} is modeled as $\tau_{ij}^{sgs} = 2\nu_t \tilde{S}_{ij}$ where ν_t is the subgrid eddy viscosity and $\tilde{S}_{ij}$ is the resolved rate-of-strain tensor defined as $\tilde{S}_{ij} = \frac{1}{2}\left(\frac{\partial \tilde{u}_i}{\partial x_j} + \frac{\partial \tilde{u}_j}{\partial x_i}\right)$. The subgrid eddy viscosity is obtained in terms of the grid scale Δ and the subgrid kinetic energy, $k^{sgs} = (\widetilde{u_i u_i} - \tilde{u}_i \tilde{u}_i)$ as: $\nu_t = C_\nu \sqrt{k^{sgs}} \Delta$. Here, k^{sgs} is obtained by solving a transport equation as described in chapter III and C_ν is a coefficient that needs to be determined.

2.2 Liquid-phase LES Equations

Both Eulerian and Lagrangian formulations have been used to simulate two-phase flows in the past [23][31]. However, most state-of-the-art codes employ the Lagrangian form to capture the droplet dynamics, while the gas phase is computed in the Eulerian form (e.g., KIVA [33]). In this formulation, the droplets are tracked explicitly using Lagrangian equations of motion, and heat and mass transfer are computed for each droplet. The DDM introduced in chapter I has two different implementations based on the velocity field experienced by the droplets. In the DSF [28], the droplets encounter the mean gas-phase velocities. While in SSF [23][27] the instantaneous gas-phase velocities are used in calculating the droplet properties. In the DSF approach, the droplet-turbulence interaction is neglected as only the averaged gas-phase quantities are used. In the present study in order to include the droplet-turbulence interaction, the SSF formulation is used to track the droplets using Lagrangian equations of motion. The general equations for spherical droplets reduce to the form shown in Eq. 2.6 and Eq. 2.7. In arriving at these equations, effects of static pressure gradient $[m_f(Du_i/Dt)]$, virtual-mass $\left[\frac{1}{2}m_f(Du_i/Dt - dv_i/dt_p)\right]$, Basset force $\left[\frac{3}{2}d_p^2(\pi\rho\mu)^{1/2}\int_{t_{p_0}}^{t_p}\frac{d/d\tau(u_i - v_i)}{(t_p - \tau)}d\tau\right]$ and external body-forces $[(m_p - m_f)g_i]$ have been neglected as they have negligible effects when the dispersed phase density is orders of magnitude large than the gas phase [50]. Here, m_f stands for the mass displaced by the droplet. Further, the inclusion of these terms is not

expected to change the current approach.

$$\frac{dx_{p,i}}{dt} = u_{p,i} \tag{2.6}$$

$$\frac{du_{p,i}}{dt} = \frac{3}{4} C_D Re_p \frac{\mu}{\rho_p d_p^2} (u_i - u_{p,i}) \tag{2.7}$$

where the droplet properties are denoted by subscript p, d_p is the droplet diameter and u_i is the instantaneous gas phase velocity computed at the droplet location. Here, the droplet Reynolds number is: $Re_p = \frac{d_p}{\nu}[(u_i - u_{p,i})(u_i - u_{p,i})]^{1/2}$. This gas phase velocity field is obtained using both the filtered LES velocity field u_i and the subgrid kinetic energy k^{sgs}.

The approach adopted for calculating the instantaneous gas phase velocities is described in this section. This approach is an off-shoot of the original methodology proposed by Gosman and Ioannides [51] for steady-state $k-\varepsilon$ methods. Here, $u_i = \tilde{u}_i + u_i'$, where u_i' is a Gaussian random number (with zero mean and unit

variance) multiplied by the fluctuating velocity obtained from k^{sgs}. The droplet is assumed to interact with this eddy as long as the droplet is within this eddy of characteristic length (grid size), or the time elapsed has not exceeded the eddy life-time (based on the grid size and the velocity scale obtained through k^{sgs}). After that time, fluctuating velocities are recomputed based on the next sequence of Gaussian random variables, to represent the interaction with the new eddy. This approach incorporates stochastic turbulent dispersion into the formulation via the subgrid kinetic energy. As detailed later, this is not possible using the standard algebraic eddy viscosity subgrid closure.

The drag relation is arrived at empirically to match the correlations for evaporating droplets assuming they retain sphericity [52][53]. This results in the following expression for C_D.

$$C_D = \begin{cases} \dfrac{24}{Re_p}\left(1 + \dfrac{1}{6}Re_p^{\frac{2}{3}}\right) & Re_p \le 10^3 \\ 0.424 & Re_p > 10^3 \end{cases} \tag{2.8}$$

The droplet mass conservation is given by: $dm_p/dt = -\dot{m}_p$ where the mass

transfer rate for a droplet in a convective flow field is given as:

$$\frac{\dot{m}_p}{\dot{m}_{Re_p = 0}} = 1 + \frac{0.278 Re_p^{\frac{1}{2}} Sc^{\frac{1}{3}}}{\left[1 + 1.232 / Re_p Sc^{\frac{2}{3}}\right]^{\frac{1}{2}}} \tag{2.9}$$

Here, Sc is the Schmidt number and the subscript $Re_p = 0$ indicates quiescent conditions where no velocity difference exists between the gas and the liquid phases. This relationship was proposed by Faeth and Lazar [54] and has been extensively used in the past (for e.g. [23]). The governing equation for mass transfer rate under quiescent media for spherically symmetric and quasi-steady conditions reduces [29] to

$$\dot{m}_{Re_p = 0} = 2\pi \rho_s D_{sm} d_p \ln(1 + B_M) \tag{2.10}$$

where, ρ_s and D_{sm} are, respectively, the gas mixture density and the mixture diffusion coefficient at the droplet surface. Also, B_M is the Spalding number which is given as $B_M = (Y_{s,F} - Y_{\infty,F})/(1 - Y_{s,F})$. Here, $Y_{s,F}$ is the fuel mass fraction at the droplet surface computed as described in [55], while $Y_{\infty,F}$ is the fuel mass fraction in the ambient gas.

The conservation of energy of the drop (assuming uniform temperature in the droplet or equivalently infinite conductivity in the droplet) reduces to the following expression [27]:

$$m_p C_{p,p} \frac{dT_p}{dt} = h_p \pi d_p^2 (\tilde{T} - T_p) - \dot{m}_p \Delta h_v \tag{2.11}$$

The heat transfer coefficient for a droplet in a convective flow field with mass transfer is modeled following the proposed correlation by Faeth and Lazar [54] as:

$$\frac{h_p}{h_{Re_p = 0}} = 1 + \frac{0.278 Re_p^{\frac{1}{2}} Pr^{\frac{1}{3}}}{\left[1 + 1.232 / Re_p Pr^{\frac{2}{3}}\right]^{\frac{1}{2}}} \tag{2.12}$$

Here, Pr is the gas phase Prandtl number and the governing equation for heat transfer rate under quiescent medium for spherically symmetric and quasi-steady conditions reduces [29] to:

$$h_{Re_p = 0} = \kappa Nu_{Re_p = 0} / d_p \tag{2.13}$$

where the Nusselt number is obtained from the relation:

$$Nu_{Re_p = 0} = \frac{2\ln(1 + B_M)^{Le^{-1}}}{(1 + B_M)^{Le^{-1}} - 1} \tag{2.14}$$

Thus, droplets above the pre-specified cut-off size are tracked using the Lagrangian approach, and their properties are determined using the above equations. Theoretically, the droplet equations have to be integrated till the mass of the droplet reduces to really insignificant value (less than fractions of a micron so that the mass and heat transfer by vaporizing such droplets instantaneously does not alter the solution). As the droplet size reduces, the particle relaxation time (governed by Eq. 2.7 and given by $(4\rho_p d_p^2)/(3C_D Re_p \mu)$), the droplet evaporation/life time (governed by Eq. 2.10 and given by $d_p^2/(12D_{sm}\ln(1 + B_M))$) and the droplet heat-up time (governed by Eq. 2.11 and is approximately equal to $\rho_p d_p/(6h_p)$), reduce approximately as the square of the droplet size. The time-step of integration of these equations has to be less than these characteristic times for accuracy. This increases the computational cost to integrate the droplet equations in addition to carrying more number (since a larger range of droplets have to be tracked) of droplet groups. In order to have computationally feasible solutions, most of the research codes such as KIVA [33] and ALLSPD3D [34] have used an *ad hoc* basis for determining the cut-off size of the droplets. Droplets below this size are

assumed to vaporize instantaneously and contribute to the continuous phase. This assumption can lead to erroneous results. The present approach overcomes this problem, as described in Chapters II and III.

In summary, the present LES approach solves only for the momentum and energy gas-phase equations on the LES grid. Closure for the subgrid terms in these equations is achieved by using a localized dynamic model for the subgrid kinetic energy (described in Chapter III). Concurrently, the liquid phase droplet equations for a range of droplet groups are solved using the Lagrangian technique. Stochastic turbulent dispersion of the droplets is included in the present approach using the subgrid turbulent kinetic energy. This capability is not directly available in closures based on the algebraic eddy viscosity model. The phase change, the subsequent fuel-air mixing and the scalar reaction-diffusion processes are modeled within the subgrid as described in chapter III.

CHAPTER III

SUBGRID MODELS

Closure of the large eddy simulation equations for both gas and liquid phases requires interaction terms to model the effect of the subgrid terms on the resolved motion. Two types of closure are needed: a closure for momentum transport and a closure for the scalar transport (both gas and liquid phases), and both are discussed in the following sections.

3.1 The Subgrid Momentum Closure

The closure for the momentum transport is achieved by using an eddy viscosity model, which is physically reasonable since the small scales are assumed to provide dissipation for the energy transferred from the large scales. The specification of the eddy viscosity requires a length and a velocity (or a time) scale.

Many past LES studies have employed an algebraic eddy viscosity model which uses the grid size as the length scale and the resolved rate-of-strain tensor as the time scale (e.g., [21]). However, the algebraic eddy viscosity model has some serious limitations. For example, this approach requires equilibrium between turbulent kinetic

energy production and dissipation in the small scales, which is possible only if a very high resolution LES grid is employed such that only the dissipation scales are unresolved. Such high resolution simulations are not feasible in practice due to resource constraints. By solving for the subgrid kinetic energy (which also gives an appropriate velocity scale for subgrid closure), the equilibrium requirement can be relaxed and coarser grid LES is possible. Furthermore, to model turbulent dispersion of particles, the subgrid kinetic energy provides the required information that is absent in the algebraic model closure. In earlier LES studies by Wang and Squires [56], subgrid kinetic energy equation was explicitly carried to provide additional information to supply velocity variations for the Lagrangian tracking scheme of the particles.

The subgrid closure of the unresolved stresses and energy flux is achieved in the present approach by solving a transport model for the subgrid kinetic energy, k^{sgs}. Details have been reported elsewhere [18] [19]. Here, the extension of the earlier gas phase model to two-phase flows has been carried out. The general form of subgrid kinetic energy equation for two-phase flows can be written as:

$$\frac{\partial \bar{\rho} k^{sgs}}{\partial t} + \frac{\partial}{\partial x_i}(\bar{\rho}\tilde{u}_i k^{sgs}) = T_k + P_k - D_k + F_k \qquad (3.1)$$

where, $T_k = \frac{\partial}{\partial x_i}\left(\frac{\nu_t}{\sigma_k}\frac{\partial k^{sgs}}{\partial x_i}\right)$ is the transport term and $\sigma_k \approx 1$ is a constant. The other

terms, P_k and D_k are respectively, production and dissipation of k^{sgs}. The last term F_k is unique to two-phase flows and represents the work done due to the two-phase coupling force term $\dot{F}_{s,i}$. This term (similar to terms in the LES equations, 2.2) provides the coupling between the turbulent motion of the droplets and the evolution of the subgrid kinetic energy. The closure of Eq. 3.1 is obtained by using $P_k = -\tau_{ij}^{sgs}\tilde{S}_{ij}$ and $D_k = C_\varepsilon \bar{\rho}\frac{k^{sgs3/2}}{\Delta}$ where, C_ε is another coefficient that must be obtained (along with C_ν) using the dynamic procedure or specifying the values. The dynamic procedure of Kim and Menon [19] is employed in the current study and briefly described here.

Dynamic models are based on the assumption of scale similarity in the inertial subrange. Provided that enough of the inertial subrange is resolved, stresses at the spectral cut-off (corresponding to the grid size) can be related to the stresses at say twice the cut-off point, called the test grid level. This then defines a scale where explicit filtering is required. The coefficients C_ε and C_ν are dynamically determined dynamically from the following expressions:

$$C_\varepsilon = 2\hat{\Delta}_{LES}\frac{(\mu + \nu_t/\bar{\rho})d^{test}}{\langle\bar{\rho}\rangle}(k^{test})^{3/2} \tag{3.2}$$

and

$$C_\varepsilon = -\frac{L_{ij}D_{ij}}{2D_{ij}D_{ij}} \tag{3.3}$$

Test level filtered quantities are defined by:

$$k^{test} = \frac{1}{2}\left\{\frac{\langle\bar{\rho}\tilde{u}_k\tilde{u}_k\rangle}{\langle\bar{\rho}\rangle} - \frac{\langle\bar{\rho}\tilde{u}_k\rangle}{\langle\bar{\rho}\rangle}\frac{\langle\bar{\rho}\tilde{u}_k\rangle}{\langle\bar{\rho}\rangle}\right\} \tag{3.4}$$

$$d^{test} = \langle\frac{\partial\tilde{u}_i}{\partial x_j}\frac{\partial\tilde{u}_j}{\partial x_i}\rangle - \frac{\partial}{\partial x_j}\left(\frac{\langle\bar{\rho}\tilde{u}_i\rangle}{\langle\bar{\rho}\rangle}\right)\frac{\partial}{\partial x_i}\left(\frac{\langle\bar{\rho}\tilde{u}_j\rangle}{\langle\bar{\rho}\rangle}\right) \tag{3.5}$$

and

$$L_{ij} = L^*_{ij} - \frac{1}{3}L^*_{kk}\delta_{ij} \tag{3.6}$$

$$L^*_{ij} = \langle\bar{\rho}\rangle\langle\tilde{u}_i\tilde{u}_j\rangle - \langle\bar{\rho}\rangle\langle\tilde{u}_i\rangle\langle\tilde{u}_j\rangle \tag{3.7}$$

$$D_{ij} = \hat{\Delta}_{LES} \langle \bar{\rho} \rangle \sqrt{k^{test}} \left(\langle \tilde{S}_{ij} \rangle - \frac{1}{3} \tilde{S}_{kk} \delta_{ij} \right) \tag{3.8}$$

where $\hat{\Delta}_{LES} = 2\Delta_{LES}$ and $\langle \ \rangle$ denote explicit filtering at the test grid level.

The following expression

$$F_k = \widetilde{\dot{F}_{s,i} u_i} - \tilde{\dot{F}}_{s,i} \tilde{u}_i \tag{3.9}$$

represents the direct effect of two-phase coupling on k^{sgs} and requires modeling. This term is due to the contribution of the unresolved component of the particle drag term appearing in the resolved scale momentum equation (Eq. 2.2). Note that, k^{sgs} is indirectly modified due to particle motion and vaporization since the force term $\dot{F}_{s,i}$ will change the resolved velocity field (via Eq. 2.2), which in turn will change the resolved subgrid kinetic energy. Inclusion of the term F_k allows for an additional (direct) modification of the subgrid kinetic energy due to interaction between the particles and the

unresolved small scale motion. Here, the term in Eq. 3.9 is modeled as follows:

$$F_k = \langle u_i \dot{F}_{s,i} \rangle - \tilde{u}_i \langle \dot{F}_{s,i} \rangle = \langle u_i \dot{F}_{s,i} \rangle - \tilde{u}_i \dot{F}_{s,i} \tag{3.10}$$

Here, $\langle \ \rangle$ represents an average over all the droplet trajectories crossing the cell and cell volume. Note that $\langle \dot{F}_{s,i} \rangle$ is replaced by $\dot{F}_{s,i}$ as the source terms given in Eq. 2.5 are already averaged over the droplets and the cell volume. This closure is very similar to that of Chen and Pereira [25], where it was applied in a k-ε Reynolds-averaged formulation. Since all the necessary information for closure is available, this is a complete representation and no tunable constants are required.

Thus, the presence of the droplets can have a two-fold effect. The first effect is directly on the LES resolved momentum transport due to the coupling force term, $\dot{F}_{s,i}$. The second effect is the modification to the subgrid kinetic energy due to the term, Eq. 3.10, which accounts for the work done due to interaction between the particles and the small-scale unresolved turbulent field. This term is positive on average when there is transfer of energy from large scales to the small scales through droplet interaction.

3.2 The Subgrid Species Closure

The principle difficulty in reacting LES simulations is the proper modeling of the

combustion related terms involving temperature and species, for example, the convective species fluxes such as $Y_{i,\alpha}^{sgs}$ due to subgrid fluctuations and the filtered species mass production rate $\overline{\dot{\omega}_\alpha}$. Probability density function methods when applied within LES either using assumed shape [57] or evolution equation [58] may be used to close $\overline{\dot{\omega}_\alpha}$, and, in principle, any scalar correlations. However, the treatment of molecular mixing and small scale stirring using phenomenological models as in probability density function (pdf) methods have been only partially successful in predicting the mixing effects. Problems have also been noted when a gradient diffusion assumption/eddy viscosity model is used to approximate the species transport terms. Use of these type of assumptions for reactive species is dubious, as noted earlier [59] [60]. Frankel *et al*. [57] attributed the use of this assumption as the source of errors in the comparison of reacting LES simulations with DNS data.

The linear eddy mixing (LEM) model [61] treats molecular diffusion and turbulent mixing processes independently at all relevant length scales of the flow. The scalar fields are simulated within a 1-D domain which, in the context of LES, represents a 1-D slice of the subgrid flame brush. The subgrid model simulates only the effect of the small unresolved scales on the scalar fields while the larger resolved turbulent scales of the flow are simulated by the LES equations. The subgrid LEM has several advantages over conventional LES of reacting flows. In addition to providing an accurate treatment of the small-scale turbulent mixing and molecular diffusion processes, this method avoids gradient diffusion modeling of scalar transport. Thus, both co-gradient and counter-

gradient diffusion can be simulated. More details of this approach are given in the following sections.

3.2.1 The single phase model

In the baseline model, the exact reaction-diffusion equations (described in Menon [2]) are numerically solved using a finite-difference scheme in the local subgrid 1D domain using a grid fine enough to resolve the Kolmogorov ($\eta = (\nu^3/\varepsilon)^{1/4}$) and/or the Batchelor ($\eta_B = \eta \mathrm{Pr}^{-1/2}$ or $\eta \mathrm{Sc}^{-1/2}$, respectively for thermal and diffusion layers) microscales. Consequently, the production rate, $\dot{\omega}_\alpha$, can be specified in the subgrid without any modeling. Simultaneous to the deterministic evolution of the reaction-diffusion processes, turbulent convective stirring within the 1D domain is modeled by a stochastic mapping process [62]. This procedure models the effect of turbulent eddies on the scalar fields and is implemented as an instantaneous rearrangement of the scalar fields without changing the magnitudes of the individual fluid elements, consistent with the concept of turbulent stirring.

The implementation of the stirring process requires (randomly) determining the eddy size l from a length scale pdf $\mathrm{f}(l)$ in the range $\eta \le l \le l_{\mathrm{LEM}}$ where η is the Kolmogorov scale and l_{LEM} is the characteristic subgrid length scale which is currently assumed to be the local grid resolution Δ. A key feature of the stirring approach is that this range of scales is determined from inertial range scaling as in 3D turbulence for a

given subgrid Reynolds number: $Re_{LEM} = u' l_{LEM} / \nu$ where, u' is obtained from k^{sgs} as $u' = \sqrt{2/3 k^{sgs}}$. Thus, the range of eddy sizes and the stirring frequency (or event time) incorporates the fact that the small scales are 3D. This feature is one of the major reasons for the past successes of LEM in gas phase diffusion flame studies [3] [4] [5] and premixed flame studies [2] [13].

A new feature for two-phase flows needs to be considered in this formulation. The above noted stirring process uses inertial range scaling laws that do not account for the presence of droplets. If, however, droplet motion and vaporization changes the turbulent spectra in the inertial range from the well known -5/3 law of Kolmogorov, then this information needs to be incorporated. The following modifications to $f(l)$ and the event frequency have to be made to account for effect of droplets on the turbulent field. If the scaling law of the inertial range of the kinetic energy spectra is p-3 (for the standard Kolmogorov scaling law, -5/3rd law - p would be 4/3), then the distribution $f(l)$ and event frequency parameter (Λ) are given as:

$$f(l) = \frac{3 - p}{l_{lem}[(l_{lem}/\eta)^{3-p} - 1]} (l_{lem}/\eta)^{p-4} \tag{3.11}$$

and

$$\Lambda = \frac{27}{2}\left(\frac{p}{3-p}\right)\left(\frac{D_T}{l_{lem}^3}\right)\frac{(l_{lem}/\eta)^{3-p}-1}{1-(\eta/l_{lem})^p} \tag{3.12}$$

The reader is referred to Kerstein [63] for details of the above formulation. The exact value of the exponent p might be modified in the presence of droplets. In the isotropic turbulence studies (Chapter V) it is found that the results are not sensitive to the value of p and it suggests that for low subgrid Reynolds numbers, using 5/3 scaling law is sufficient to model subgrid scales accurately.

3.2.2 The two-phase model

For two-phase flows, the LEM reaction-diffusion equations have been modified to include two new features: (a) the vaporization of the droplets tracked by the Lagrangian method, and (b) the vaporization of droplets below the cut-off so that the final stages of droplet vaporization and mixing is included. However, some changes are required since droplet vaporization will change the subgrid mass of the gas (primarily the fuel). Thus, in addition to the scalar reaction-diffusion equations, the two-phase mass conservation equations must be solved in the subgrid.

The droplets below the cut-off have been included by assuming that the droplets (below the cut-off) act as a psuedo-fluid and therefore, the overall effect of the droplets

within each LES cell can be modeled in an Eulerian formulation using a void fraction (volume of the liquid phase to the overall volume of the cell). This approach is valid only when the droplets carried in the subgrid sum to only a small fraction of the total volume (or void fraction is small) and the size of the droplets carried in the subgrid are reasonably small such that drag effects are negligible. However, this is an acceptable assumption here since all droplets larger than the cut-off are still tracked using the Lagrangian approach. The present Eulerian two-phase approach is also preferred in terms of accuracy, when compared to the Lagrangian approach, since, as the droplets become very small they begin to behave more like a continuum fluid.

Mass conservation in both the phases in the LEM is given by: $\rho_g \varphi + \rho_l (1 - \varphi) = \rho_{avg}$, where subscript g represents gas phase, l the liquid phase and φ is the volume fraction of the gas phase (1 - void fraction of the liquid (λ)). The void fraction λ or φ evolve during the subgrid evolution. Although, the liquid density is a constant, the gas density ρ_g changes and needs to be determined. The mass conservation of each phase is imposed in the subgrid scales and are obtained from the following equations:

$$\frac{\partial \rho_g \varphi}{\partial t} = S_L + S_2 \tag{3.13}$$

and

$$\frac{\partial(1-\varphi)\rho_l}{\partial t} = S_1 - S_2 \tag{3.14}$$

Here, the source term S_1 is the contribution of the supergrid droplets (i.e., the LES-resolved Lagrangian droplets) to the subgrid liquid phase when the droplet size falls below the cut-off. These terms are given in Eq. 2.5, except that the volume change is equal to the entire volume of the droplets below the cut-off or equivalently correspond to the volume averaged mass of all the droplets below the cut-off size at that time instant. S_L is due to vaporization of the droplets tracked in the supergrid and is same $\dot{\rho}_s$ as given in Eq. 2.5. S_2 represents vaporization of liquid in the subgrid and is computed by carrying Eq. 2.10 in the subgrid. In order to determine the droplet temperature, Eqs. 2.11 and 2.13 are solved in the subgrid.

The gas phase species equation for any scalar mass fraction ψ in the subgrid can be written as

$$\frac{\partial \rho_g \varphi \psi}{\partial t} = \frac{\partial}{\partial s}\left[D\frac{\partial(\rho_g \varphi \psi)}{\partial s}\right] + \dot{\omega}_\psi + S_\psi + S_L \tag{3.15}$$

Here, "s" indicates the 1D domain of LEM. Also, S_ψ is the source term (only in the fuel species equation and is equal to S_2 as the liquid phase consists of a single species in the present case but the approach is general to have multi-species in the liquid phase) for production due to vaporization of the liquid phase from the Lagrangian tracking. In the above equations each of the mass fractions are functions of the LEM 1D domain within each LES cell. For any species k, the supergrid mass density ($\bar{\rho}\tilde{Y}_k(x,t)$) will be equal to the average of $(\rho_g(s,t)\varphi(s,t)\psi(s,t))$ over the subgrid LEM cells. Note that the $\sum_k \rho_g(s,t)\varphi(s,t)\psi(s,t)$ is equal to $\rho_g(s,t)\varphi(s,t)$ and average of $\rho_g(s,t)\varphi(s,t)$ over the subgrid LEM cells is equal to $\bar{\rho}$.

An equation for gas phase temperature is also solved with the above equations since vaporization requires heat absorption and is followed by a drop in temperature. This equation is as follows:

$$C_v \frac{\partial \rho_g \varphi T}{\partial t} = \frac{\partial}{\partial s}\left[\kappa \frac{\partial\left(\rho_g \varphi T\right)}{\partial s}\right] + \dot{E} + \dot{Q}_L + \dot{Q}_{sgs} \tag{3.16}$$

Here, C_p is the specific heat at constant pressure, T is the gas phase temperature in each of the subgrid cells, $\dot{E}$ is the heat release term due to chemical reactions, $\dot{Q}_L$ is the heat source term from the Lagrangian tracking scheme and $\dot{Q}_{sgs}$ is the heat source term due to

the dispersed phase in the subgrid and it is calculated using the relation given in Eq. 2.5, just as it is computed for the supergrid equations for the conventional case.

Note that, in Eq. 3.13, Eq. 3.14 & Eq. 3.15 the convective terms $\frac{\partial \rho_g u_i \varphi}{\partial s}, \frac{\partial (1-\varphi)\rho_l u_i}{\partial s}, \frac{\partial \rho_g \varphi \psi u_i}{\partial s}$ are missing. This is consistent with the earlier implementation of LEM in LES [2], whereby, the convection of the scalar fields is modeled using two distinct and concurrent processes: the small-scale turbulent stirring which accounts for convection in the small scales and the splicing process which accounts for convection of scalars by the LES-resolved large-scale motion. The implementation of the small-scale turbulent stirring process and the large-scale convection process is discussed in Chapter IV.

The subgrid closures for two-phase flows discussed in this chapter are implemented and tested in isotropic turbulence, temporal/spatial mixing layers and are reported in Chapters V, VI and VII. The implementation details are given in Chapter IV.

CHAPTER IV

NUMERICAL IMPLEMENTATION

4.1 Gas-Phase Solver

The two-phase subgrid model as discussed in Chapter III has been implemented into a zero-Mach number code. The zero-Mach number incompressible code used here is developed and implemented for a variety of problems by Chakravarthy and Menon [12] [13]. This code [64] is a finite-difference semi-implicit solver that is second-order accurate in time, and uses a fifth-order upwind biased stencil for the convective terms, a fourth-order central scheme for the viscous terms and a second-order scheme for the solution of the Poisson equation for pressure.The time-integration is conducted using a two-step, semi-implicit, second order accurate, fractional step method. A collocated grid system is used for the finite-difference spatial discretization of the governing equations. In this solver, the fractional step method has been implemented on non-staggered grids for improved accuracy and simplicity on skewed grids. The volumetric dilatation is explicitly obtained from Eq. 2.3. Conservation (divergence) forms can not be used in solving zero-Mach number equations and hence the solver is based on finite differences rather than finite volumes. More details of this scheme are available in Appendix B.

4.2 Dispersed Phase Solver

The Lagrangian tracking of the droplets is carried out using a fourth-order Runge-Kutta scheme and the gas phase velocity at the droplet location is obtained using a fourth-order Lagrangian interpolation scheme.

Equations 2.6, 2.7 and 2.11 are time integrated using a fourth order Runge-Kutta scheme. Here, y(x,t) denotes the velocities and temperatures of the droplets and the time step h is chosen such that it is minimum of the droplet relaxation time, droplet life time, droplet translation time, eddy interaction time and the time step of the LES solver. This is similar to the procedure followed by Oefelein and Yang [23]. Runge-Kutta algorithm computes the solution of the initial value problem $y = f(t,y)$, $y(t_0) = y_0$ at equidistant points $t_1 = t_0 + h$, $t_2 = t_1 + 2h$,.....,$t_N = t_0 + Nh$, where f is such that this problem has a unique solution on the interval $[t_0, t_N]$. The new solution at a new time step is given by

$$y_{n+1} = y_n + \frac{1}{6}(k_1 + 2k_2 + 2k_3 + k_4)$$

where y_{n+1} is the approximation to the solution $y(t_{n+1})$ at $t_{n+1} = t_0 + (n+1)h$ where $n = 0,1,...., N-1$.

k_1, k_2, k_3, k_4 are defined as follows

$$
\begin{aligned}
k_1 &= hf(t_n, y_n) \\
k_2 &= hf\left(t_n + \frac{1}{2}h, y_n + \frac{1}{2}k_1\right) \\
k_3 &= hf\left(t_n + \frac{1}{2}h, y_n + \frac{1}{2}k_2\right) \\
k_4 &= hf(t_n + h, y_n + k_3) \\
t_{n+1} &= t_n + h
\end{aligned}
\tag{4.1}
$$

Thus, the solution of the Lagrangian equations for the droplets are time-stepped till the LES time-step is attained. This is the standard leap-frog scheme for solving two-phase flows using Eulerian solvers for gas-phase and Lagrangian solvers for the droplets. The coupling between the two phases is very weak if there are huge disparities between the time-steps of both the solvers. These disparities can lead to inaccuracies. This imposes additional restrictions (in the present case the time-step was reduced till numerical convergence was assured) on the gas-phase time-stepping in addition to the usual CFL conditions.

4.2.1 Interpolation schemes

In the simplest form the gas-phase properties at the location of the droplet/particle are obtained by averaging the properties at the eight corners of the gas-phase cell

surrounding the droplet. This type of interpolation can be inaccurate and hence, higher order interpolation is needed to calculate the velocities and is implemented in the incompressible solver. In this thesis, a fourth-order, three-dimensional Lagrangian interpolation scheme has been used. Fluid velocities on the 4x4x4 grid lattice surrounding the particle have been used to evaluate the gas-phase velocities at the location of the particle. The interpolated gas velocity at the particle location is given as follows:

$$u_{l,I} = \sum_{i=0}^{3}\sum_{j=0}^{3}\sum_{k=0}^{3} u_l(x, y, z, t)L_i(x)L_j(y)L_k(z) \tag{4.2}$$

where x, y and z are the surrounding grid points. The Lagrangian basis function to determine the above is obtained by constructing a polynomial through the surrounding nodes where the function values are available:

$$L_i(x) = \prod_{\substack{k=0 \\ k \neq i}}^{3} \frac{(x - x_k)}{(x_i - x_k)} \tag{4.3}$$

and similarly for $L_j(y), L_k(z)$. In each direction, the interpolated velocities are polynomials of degree three and thus the error approximates to $O(h^4)$.

In addition to the above interpolation, appropriate extrapolation has to be used to

project the source terms due to the dispersed phase onto the grid location for implementing the two-way coupling between the two-phases. Two methods of source term extrapolation onto the surrounding grid were investigated. In the first case, all the weights were assumed to be the same and thus the source term is equally distributed to the surrounding nodes. In the second case, the weights were calculated based on the droplet distance to the nodes and thus the nodes closer to the droplet position have more contribution of the source term when compared to the farther nodes. Both cases gave statistically similar results and therefore, the equal-weights method is used in all the simulations reported in this thesis.

Particles in a decaying vortex

Using the exact solution of a decaying vortex, the dispersion of the droplets is first investigated. Five different sized particles are injected in the core of the vortex in the x-direction with a specified velocity. The subsequent trajectories of these particles are tracked. Figure 4.1a shows the velocity vector field and Fig. 4.1b shows the trajectories of the injected droplets. It can be seen that the smaller particles follow the vortex streamlines closely as the particles equilibrate with the local fluid motion quickly because of their lower inertia. The larger particles retain their initial inertia for a longer time and thus have very little influence due to the fluid motion. The particles of intermediate size have in-between behavior. This qualitatively confirms the validity of the Lagrangian particle tracking model in the LES code.

4.3 Subgrid Implementation

Since the filtered species $\tilde{Y}_\alpha(\vec{x}, t)$ and the mixture density $\bar{\rho}(\vec{x}, t)$ are calculated directly by ensemble averaging the subgrid $Y_\alpha(s, t)$ and $\rho(s, t)$ fields, there is no need to solve the equivalent LES filtered mixture mass and species conservation equations (i.e., Eq. 2.1 & Eq. 2.4). As mentioned in Chapter III, both $Y_\alpha(s, t)$ and $\rho(s, t)$ subgrid fields are influenced by small-scale and large-scale convection (due to the velocity field u_i and the subgrid turbulent fluctuation estimated from k^{sgs}). The small-scale convection is achieved by the mapping events while the latter is implemented by a Lagrangian transport model, as discussed below.

Turbulent convection or stirring is modeled as stochastic rearrangements events that interrupt the deterministic diffusion, vaporization and reaction mechanism (Eqs. 3.13, 3.14 & 3.15). Each rearrangement event is interpreted as the action of a single eddy on the scalar field and is numerically implemented as a mapping process called the triplet map [65]. This mapping first creates three copies of the chosen segment and then increases the spatial gradients of the copies by compressing each segment by a factor of three and reversing the middle segment. The original segment is then replaced by this mapping. Mathematically, the triplet map transforms the scalar $c(x, t_o)$ to $\hat{c}(x, t_o)$

according to:

$$\hat{c}(x, t_o) = \begin{cases} c(3x - 2x_0, t_0) & x_0 \le x \le x_0 + l/3, \\ c(-3x + 4x_0 + 2l, t_0) & x_0 + l/3 \le x \le x_0 + 2l/3, \\ c(3x - 2x_0 - 2l, t_0) & x_0 + 2l/3 \le x \le x_0 + l/3, \\ c(3x - 2x_0, t_0) & \text{otherwise} \end{cases} \tag{4.4}$$

where l is the size of the mapping event, x_0 is the location of the mapping event and t_0 is the time of the event. An illustration of the mapping event is shown in Fig. 4.2. The mapping event has several attributes similar to turbulent convection [16]. First, it is known that the flame surface normal aligns with the most compressive strain-rate direction, which is mimicked by the compressive nature of the triplet mapping. Second, mapping increases the number of crossings of a single scalar value, which may be interpreted as an increase in surface area caused by flame wrinkling. Finally, turbulent scaling laws are built into the model in order to get the correct rate of strain [63].

The three quantities required to describe the mapping event are: the segment (eddy) size to be mapped (or stirred), the location of the event, and the rate (or frequency) of the event. These are calculated as described in Chapter III.

The convection of the scalar fields by the LES field across LES cell faces is modeled by two different methods and the details of the choice are described below while enumerating both the schemes. The first method used is the “splicing” algorithm [2] [3] [4] and the second method is based on convection as in finite volume methods as

described below. In the first method, given the initial subgrid scalar fields and void fraction, droplet vaporization, reaction-diffusion, turbulent stirring, and large scale convection processes are implemented as discrete events within each LES cell. The epochs of these processes are determined by their respective time scales.

The splicing algorithm transports subgrid fluid elements from one LES cell to another based on the local velocity field. The local velocity consists of the resolved velocity u_i plus a fluctuating component estimated from the subgrid kinetic energy. The splicing events are implemented discretely on the convective time scale. Each splicing event involves (1) the determination of volume transfer between adjacent LES grid cells, (2) the identification of the subgrid elements to be transferred, and (3) the actual transport of the identified fluid elements. The number of cells spliced across an LES x-face (i, j, k) is the flux across the cell surface multiplied by the number of LEM cells and is given by,

$$N_{splice} = \left(\frac{\Delta t(\tilde{u}_i + u'_{sgs,\,i}) S_{x,\,i} N_{LEM}}{\Delta V_{LES}} \right) \tag{4.5}$$

where $\tilde{u}_i + u'_{sgs,\,i}$ is at the x-face of the cell constructed around point (i, j, k) using the centers of the finite difference grid, $S_{x,\,i}$ is the area vector of the face, N_{LEM} is the number of LEM cells and ΔV_{LES} is the volume of the LES cell. The resulting splicing algorithm is illustrated in Fig. 4.3. Here, schematically the transfer of subgrid elements

from LES cells “left” and “below” to the “self” cell is shown. The representative shape of the resulting scalar is also shown.

An important property of the splicing algorithm is that the species convection is treated as in Lagrangian schemes as it is advected across LES cells based on velocities. Thus, convection is independent of the magnitude or gradient of the species which are transported and depends only on the velocity field. This property allows this algorithm to avoid false diffusion associated with numerical approximation of convective terms in differential equations. By avoiding both numerical and gradient diffusion, the splicing algorithm allows an accurate picture of the small scale effects of molecular diffusion to be captured, including counter-gradient and differential diffusion effects [11].

Some of the disadvantages of the splicing algorithm in this implementation are:

- Number of cells obtained by using Eq. 4.5, in general, is not an integer value. Thus, partial cell transport can occur and must be accounted for. Here, the partial cells are accumulated until an integer value is reached and then the whole cell is transported. In flows, where there is no mean convection velocities and very low Reynolds numbers (implying very less number of LEM cells) errors due to partial cell transport can accumulate. This is the case with isotropic turbulence where there is no mean convection and subgrid Reynolds numbers are low. Hence, the modified splicing algorithm described below is used in this case.
- In grids where the volume of LES cells is not a constant, expansion and compression of LEM cells has to be carried out making the algorithm more complicated.

This is the case in the spatial mixing layer simulation and thus the alternate splicing algorithm suggested below is used.

- As seen in Fig. 4.3, the splicing algorithm can create artificial gradients at the interface of subgrid elements of different cells. This gradients can introduce errors if the stirring processes are not frequent enough. This creation of artificial gradients did not play any role in the results obtained in the temporal mixing layer simulations detailed in Chapter VI.

In order to simplify the convection algorithm and eliminate any *ad hoc* implementation, in the second method, the following procedure has been adopted for the isotropic turbulence cases (where there is no mean convection direction) and also for the spatial mixing layers (where there is stretching in both x and y directions). The scalars are convected across the cells in a finite-volume sense based on the convective fluxes (as calculated in Eq. 4.5) across the cell surfaces. For example if the flux coming in from 'left' cell is 0.3, flux coming in from 'below' cell is 0.2 and flux leaving 'self' cell is 0.5, retain 0.5 fraction of the scalar field of the current cell and add 0.3 fraction and 0.2 fraction of the scalar fields from 'left' and 'below' cells, respectively, to get the new scalar field in the 'self' cell. This convection retains the essential properties like mean, variance and all higher order moments of the scalar and is accurate if the CFL is one and is illustrated in Fig. 4.3. This can be easily seen in Fig. 4.4 where the circle convects in the x direction retaining its initial shape. The flattening of the edges is due to the initialization of circle on a cartesian grid of coarse resolution. It is interesting to note that all the geometric properties of the scalar are accurately retained through the convection

process. In cases where the CFL is less than one or when the scalar field is propagated at an arbitrary direction, any cell through which a scalar gradient is advected retains that information for considerable time even though it might be small. This will cause the history effect and can lead to spurious diffusion.

If the convection problem is looked at mathematically, there are inherent limitations as one is trying to map a field that is inherently three dimensional onto one dimension and doing the inverse map to get the 3D information. This process can only be approximate and modifications have to be made case by case to counter some of the inaccuracies. This approach is still expected to be more accurate than other approaches as the rich subgrid field is constructed by resolving all scales of interest apart from the fact that DNS of realistic high-Re flows can not be performed to resolve all scales of interest.

The coupled two-phase LES/LEM solver is illustrated using the block diagram in Fig. 4.5. As shown in the block diagram, the solver can be broken into three main components. The first one involves the solution of the filtered equations in the gas-phase solver (Eqs. 2.2 & 2.3) along with the subgrid kinetic energy equation (Eq. 3.1) to close the momentum equation. The second one involves the solution of the particles/droplets at the supergrid using the Lagrangian tracking scheme (Eqs. 2.6-2.14). The third one involves the solution of liquid/gas phase in the subgrid on the LEM line within each LES cell (Eqs. 3.13-3.16).

To summarize, in this approach, the resolved scale mass, momentum, and energy transport are simulated on a conventional grid using a conventional LES method. However, no scalar transport is simulated on the LES grid. Rather, within each LES cell,

a subgrid one-dimensional (1D) domain is defined and within this 1D domain, turbulent small-scale mixing, molecular transport, chemical kinetics and vaporization are explicitly modeled. The local 1D domain can be visualized as a stochastic instantaneous slice of the local 3D flame brush and the resolution in this domain is chosen to resolve all relevant length scales. As a result, the chemical reaction-diffusion equations along with vaporization can be solved without any assumptions (i.e., as a direct simulation).

Figure 4.6 illustrates how the subgrid void fraction of the droplets, the reactants and products vary as the droplet traverses through the flame and reduces in size. As the droplets vaporize, they contribute to the gas-phase fuel. The droplets below the cut-off also contribute to the subgrid void fraction. Reaction-diffusion mechanisms take place concurrent to vaporization and the fuel reacts with oxidizer to form product. Far away from the flame, the subgrid essentially contains product and sometimes with unreacted fuel and possibly unvaporized liquid.

4.3.1 Stand alone implementation of the new LEM model

Since there is no data to validate the subgrid vaporization model discussed here the current predictions were first compared with results obtained earlier by Mc. Murtry *et al*. [66] who employed the LEM in a stand-alone mode to study decay of a non-reactive scalar field. Here, using very similar initialization, the decay of a scalar was investigated in the presence of droplet vaporization. A range of initial values of the void fraction (0.0001, 0.001 and 0.005) was used for these simulations. These are typical of void fractions occurring in physical combustors. The mass of the injected fuel is typically of

the order of the inflow gas. Since the density of the liquid fuel is three orders of magnitude larger than the gas, the void fractions used here cover the range experienced in the dilute phase regime of most combustors. As shown in Fig. 4.7, as the droplet evaporates and the void fraction tends to zero (or $\varphi \rightarrow 1$), the scalar variance approaches the value predicted by [49] in the absence of droplets. This asymptotic behavior is expected as the scalar variance in the absence of the liquid phase should be same as that of a pure gas phase.

In Fig. 4.8a, the product mass fraction evolution in time, which is the time between two LES time steps in coupled LEM/LES implementation, is shown for a range of initial values of void fraction under otherwise identical conditions. Product formation increases in time and with increase in the initial void fraction of fuel. However, since the vaporization process is endothermic and non-linear (initially very high but levels off in time as temperature fall), the product increase is also non-linear. The product formation and vaporization have a direct correspondence. Figure 4.8b shows that the product mass fraction increases with initial liquid and gas temperature. An increase of 100 K in the temperature increases the initial vaporization rate considerably and this results in much larger amount of product formed. At present, it is assumed that both gas and liquid are at the same temperature or in other words, there is infinite conductivity in the subgrid. However, this assumption can be relaxed.

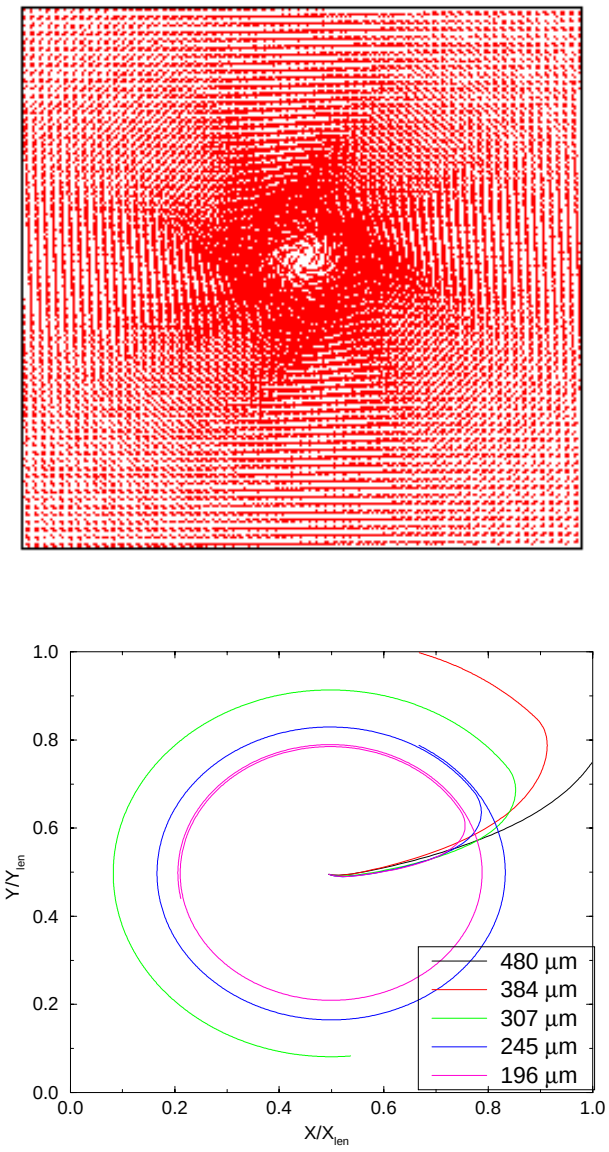

Figure 4.1 (a) The velocity vector field around the core of a decaying vortex. (b) Trajectories of the particles injected into decaying vortex.

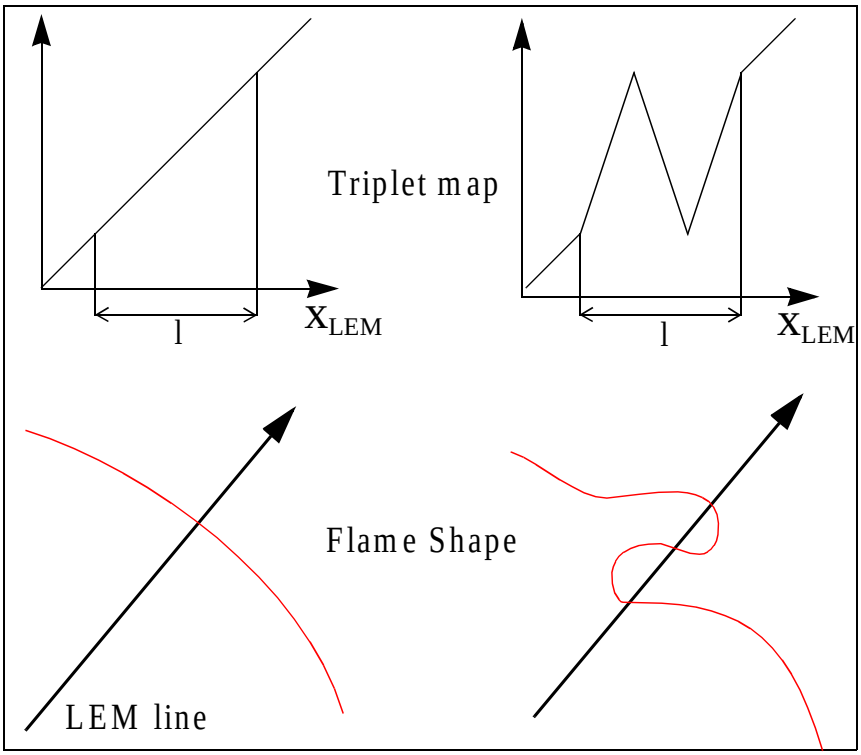

Figure 4.2 Schematic diagram of an LEM triplet mapping event.

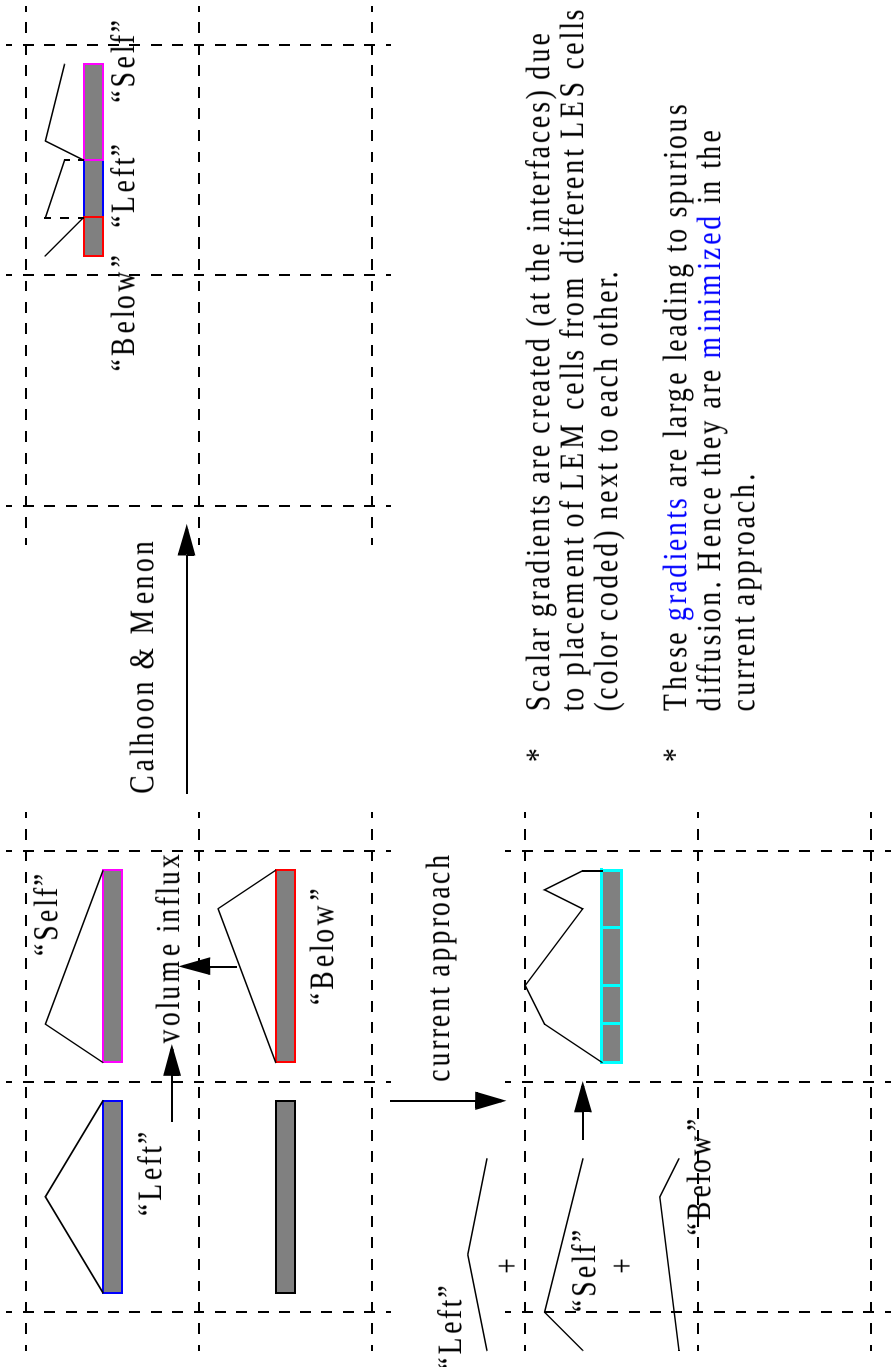

Figure 4.3 Schematic of the LEM splicing algorithm.

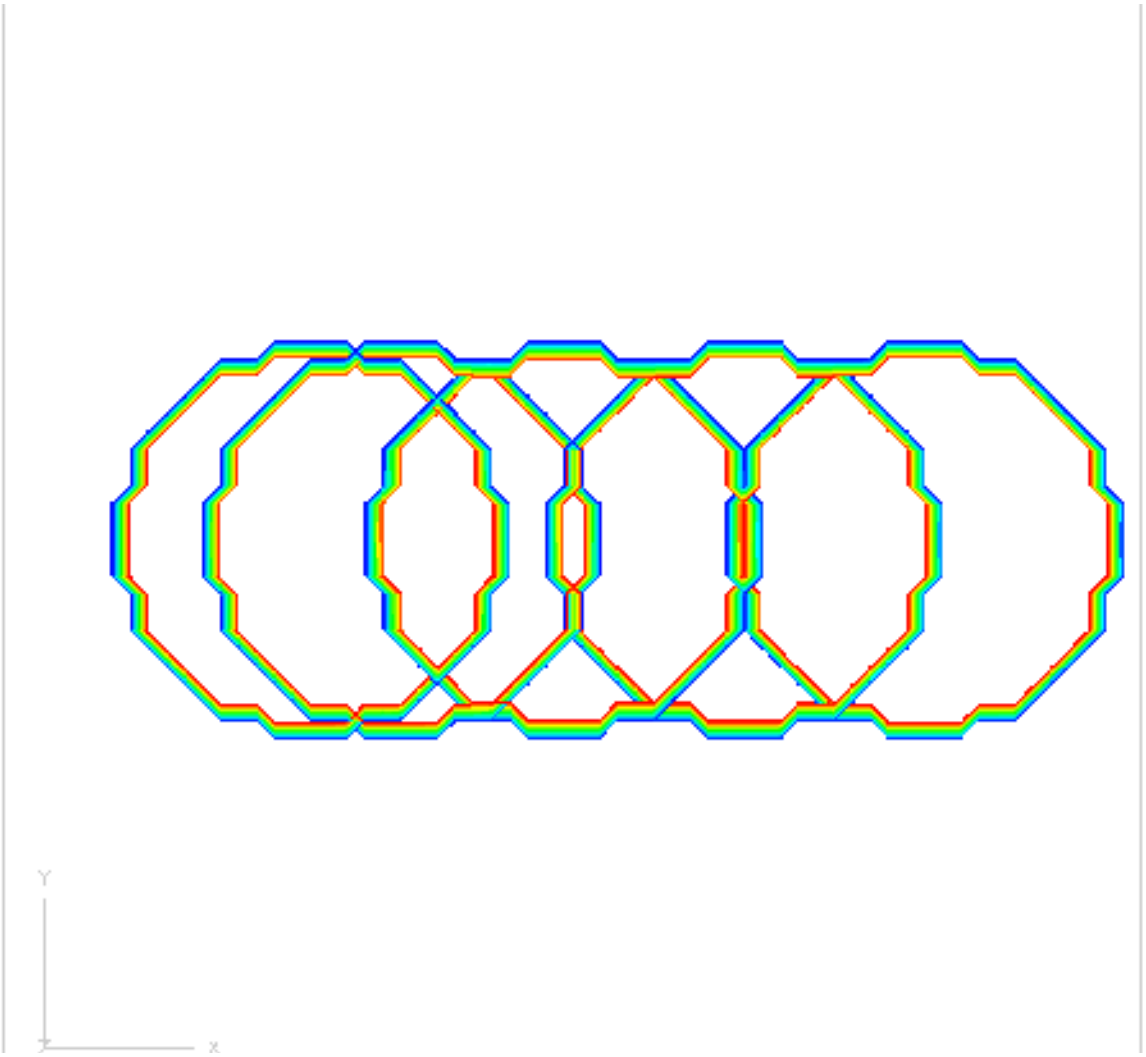

Figure 4.4 Translation of a circle in x-direction using the flux-based convection algorithm.

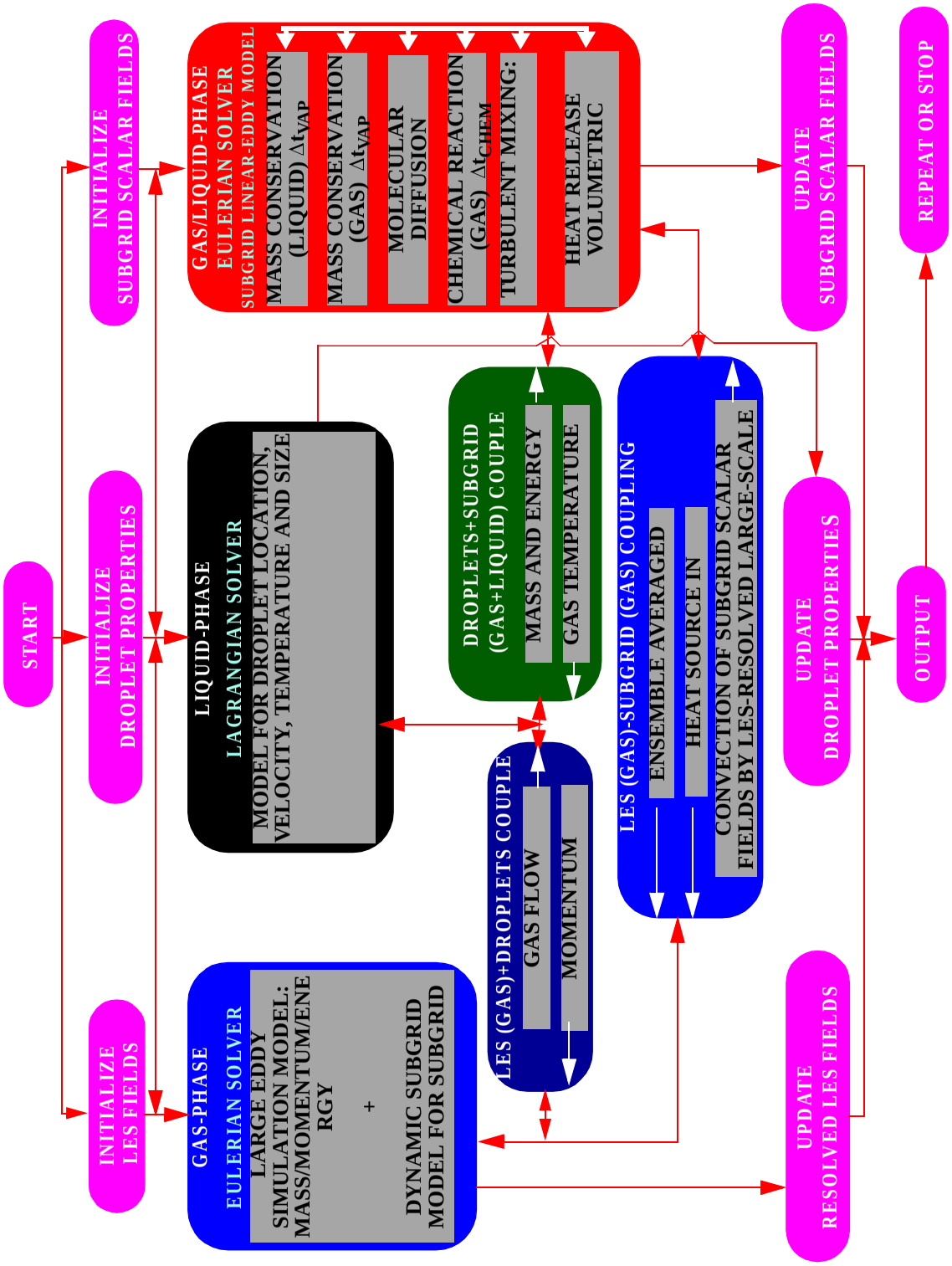

Figure 4.5 Block diagram of the two-phase LES solver

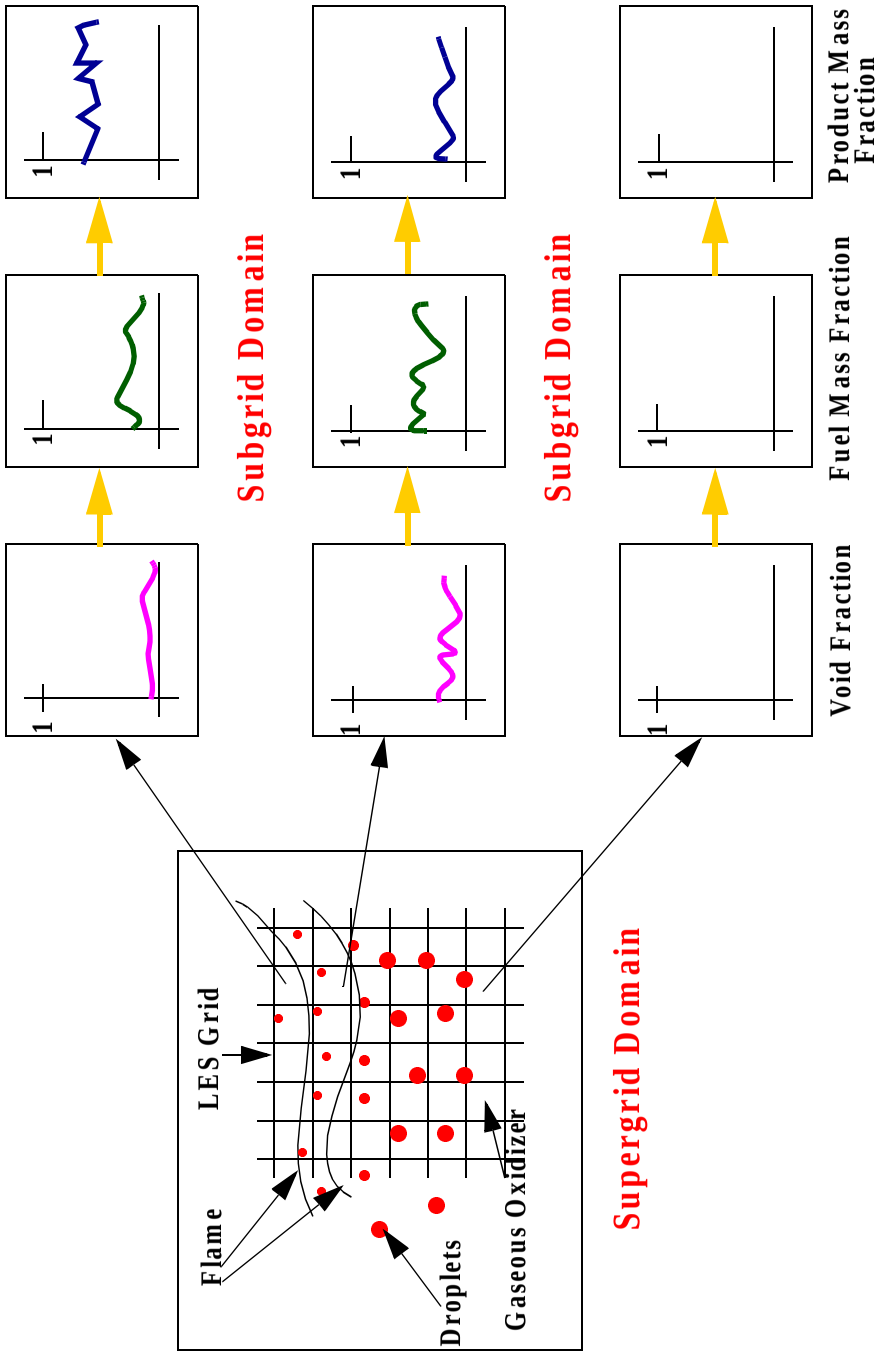

Figure 4.6 Subgrid implementation for two-phase flows.

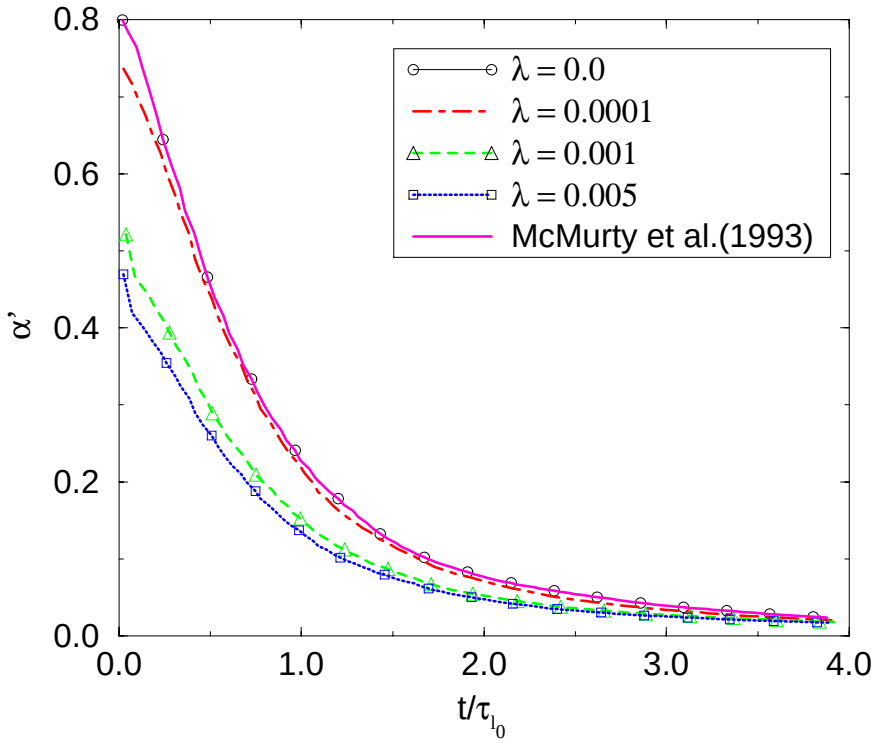

Figure 4.7 Time evolution of a passive scalar rms for different initial void fraction for $Re_{sgs} = u'\Delta/\nu = 90$ and T= 400K.

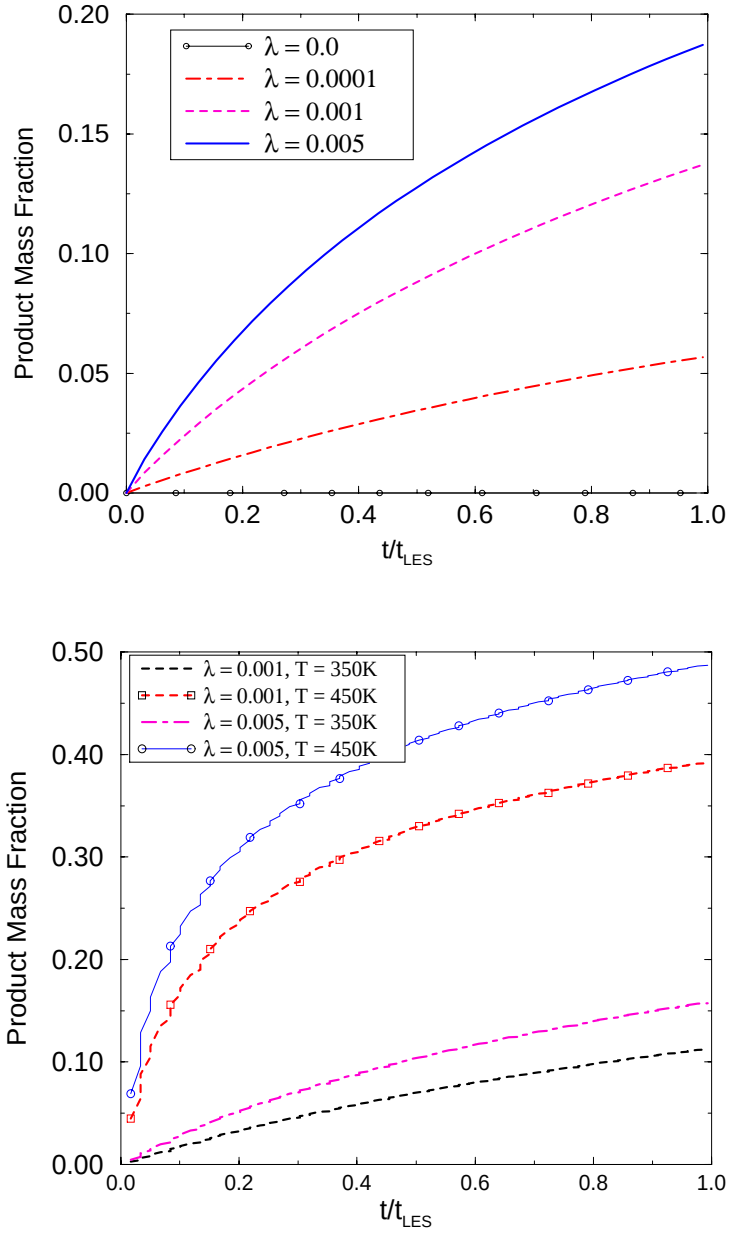

Figure 4.8 Time evolution of product mass fraction at $Re_{sgs} = u'\Delta/\nu = 90$ (a) variation of void fraction for T= 350 K and (b) Variation in temperatures and void fractions.

CHAPTER V

DNS AND LES OF TWO-PHASE ISOTROPIC TURBULENCE

In chapter I, the basic objectives of this thesis were introduced. They included studying and developing models for coupling dispersed phase and the continuum phase at all scales of interest. Experiments are very limited in their ability to provide information at all the relevant scales. In this respect, DNS has been a valuable tool to obtain detail understanding of interactions between the two phases (e.g. Boivin *et al.* [36]). In this chapter, both decaying and stationary turbulence are simulated using both DNS and LES. Here, the specific objective is to use DNS as a validation tool for two-phase LES modeling.

5.1 Decaying Isotropic Turbulence

Some of the early work as part of this thesis was based on the following assumptions:

a) The effect of droplets is ignored in the subgrid k-equation.

b) Scaling laws arrived at for subgrid scalar calculations are based on the 5/3rd law.

In order to address the above issues, both DNS and LES of isotropic turbulence is carried out under similar conditions to that of Elgobashi and Truesdell [40]. DNS is carried out using a 128^3 grid for an initial Taylor's Reynolds number ($Re_\lambda = u'\lambda/\nu$, where λ is the Taylor's length scale) of 50 and 32^3 particles. LES is carried out for the same conditions but using a resolution of 64^3. For the uncoupled case, particle Lagrangian velocity autocorrelations in all the three directions for LES and DNS are plotted in Fig. 5.1a. The autocorrelation coefficient is computed using the following relation:

$$R_{Lp,\,i} = \frac{\langle v_i(t_o)v_i(t_o+\tau)\rangle}{[\langle v_i^2(t_o)\rangle]^{1/2}[\langle v_i^2(t_o+\tau)\rangle]^{1/2}} \tag{5.1}$$

LES and DNS results show very good agreement with each other, as well as the results of Elgobashi and Truesdell [40]. The same kind of results are obtained for particle mean-square displacements (square of displacements from initial locations averaged over all the particles) and are shown in Fig. 5.1b. Here, there are some differences in the displacements in all the three directions and might be due to the fact that the initial conditions are not perfectly isotropic. Unlike stationary isotropic turbulence, where on the average an isotropic field is obtained, here the results are sensitive to the initial conditions.

One of the objectives of this thesis is to extend the earlier LES studies [23] [24] to incorporate turbulence modification due to the presence of droplets. For the uncoupled

case, droplet dispersion by turbulence is well captured by the Stochastic Separated Flow model (SSF). The effects of droplet coupling on turbulent kinetic energy can be deduced from the kinetic energy spectra plotted for momentum coupled and uncoupled case in Fig. 5.2a. As noted in all the other studies (e.g. Squires and Eaton [38]) with momentum coupling, there is increase in energy at high wave numbers and corresponding decrease in energy for low wave numbers. This is due to the fact that the droplets drain the energy from the energetic mean flow and later interact closely with scales comparable to its size. The same is evident in the dissipation spectra (Fig. 5.2b). Similar trends are captured by both LES and DNS and are in accord with the earlier DNS studies of decaying isotropic turbulence [38] [40]. The negligible differences between the coupled and uncoupled cases are due to the low mass loading of the particles and relatively lower Reynolds number. The lack of stationarity coupled with the fact that the Reynolds number is low makes decaying isotropic turbulence an unsuitable test bed for model development and validation. For the reasons stated above, stationary isotropic turbulence was simulated at higher Reynolds number as described in following section.

5.2 Stationary Isotropic Turbulence

The simulations were started from a stationary state of 64^3 pseudo-spectral simulation of isotropic turbulence (Yeung and Pope, [67]). The simulations were forced using an integrated stochastic forcing scheme with parameters given in Table 5.1. These are the same conditions used by Yeung and Pope [67]. The integrated stochastic forcing

is an improvement by Yeung and Pope [67] over the stochastic forcing scheme introduced by Eswaran and Pope [68]. Most commonly used forcing schemes, often referred as "frozen-amplitude" method, freezes the anisotropy in the large-scales. This anisotropy stipulates averaging over several computations to get time-averaged quantities with reasonably small statistical errors. Other techniques such as rate-of-strain-modeling method and Euler-forcing also have similar drawbacks [68]. The stochastic forcing is refined for better differentiable properties by Yeung and Pope [67]. The basic forcing scheme is used to maintain sufficient generation of the turbulence energy to balance the energy loss due to viscous dissipation. For each non-zero wavenumber 'k' lying within the spherical shell of radius K_F, an artificial random acceleration term $a_F(k,t)$ is added to the momentum equation in the Fourier space. In the integrated stochastic forcing approach, $a_F(k,t)$ is specified as a complex vector-valued 'integrated' Uhlenbeck-Ornstein (IUO) process. The forcing accelerations are calculated in the spectral space. These accelerations modify the velocities in the spectral space which are later transformed to physical space for computations. The forcing for the LES cases is also carried out at the 128^3 resolution and filtered down to 64^3 to preserve similarity and to remove uncertainty associated with variations in the forcing characteristics such as the forcing radius. The simulations were advanced in time for several flow-through times till a statistically stationary state evolved. Statistics were collected over 15 eddy-turn over times (based on the velocity and longitudinal integral length scale) and all the flow characteristics corresponding to this state are given in Table 5.1. Droplets were then added to this field and the two-phase simulations evolved in time for another 3-4 eddy-turn over times

before statistics were collected for 3-4 eddy-turn over times. Boivin *et. al* [36] used 6 eddy-turn over times to average the statistics. In this study it has been found that 3-4 eddy-turn over times was sufficient to reach stationarity. The differences in the requirements, might be due to slight differences in the forcing scheme used and possible differences in the numerical algorithms and resolution.

In the following section, the discussion focuses on the validation of the gas-phase and two-phase finite-difference code in the light of earlier work [36] [67]. The effect of vaporization is then addressed.

5.2.1 DNS of single-phase isotropic turbulence

Before simulating the two-phase flows, the base-line gas-phase code has to be validated for applicability to isotropic turbulence. Isotropic turbulence in a domain with dimension $2\pi^3$ and $Re_\lambda \sim 62$ is simulated using a 128^3 grid. Normalized energy spectra and dissipation spectra are compared to the experiments (Re_λ=65) of Comte-Bellot & Corrsin [69] and the DNS (Re_λ=63) using 128^3 grid of Yeung and Pope [67]. Good agreement with experiments and earlier simulations at high wave numbers is evident from Fig. 5.3. In addition the present simulation also predicts the dissipation peak and its location very well. Yeung and Pope [67] use $k_{max}\eta$ to characterize the resolution of the simulations (k_{max} is the maximum wave number and η is the Kolmogorov length scale). In pseudo-spectral codes this has to be > 1.5 for adequate resolution. The resolution requirements for a finite-difference code are more severe. The current simulations are

carried out with $k_{max}\eta \sim 2.3$ and it seems that the resolution is sufficient to resolve the small scales. To verify this, another higher-order measure of small-scale behavior, the dissipation skewness (S_ε) and is defined (Kerr [70]) as:

$$S_\varepsilon = \frac{4}{35}\left(\frac{15\nu}{\langle\varepsilon\rangle}\right)^{\frac{3}{2}} \int_0^{k_{max}} \nu k^4 E(k) dk \tag{5.2}$$

is computed. Here, E(k) is the energy spectrum function at the scalar wave number $k \equiv (\underline{k} \cdot \underline{k})^{1/2}$, k_{max} is the highest wave number, ν is the kinematic viscosity and $<\varepsilon>$ is the volume-averaged dissipation obtained by integration of dissipation spectrum D(k), defined by $2\nu k^2 E(k)$. From Table. 5.1 it can be seen that the value of this function is 0.53, very close to asymptotic value of 0.5 for high-Re. This value also compares very well to the values as reported in Eswaran and Pope [68] and Yeung and Pope [67].

Other parameters are also computed, for example the two-point velocity correlation tensor (with separation vector r)

$$R_{ij}(r) = \langle u_i(x) u_j(x + r) \rangle \tag{5.3}$$

and the integral length scales (with no sum over Greek indices):

$$L_{\alpha\alpha,\beta} = \frac{1}{\langle u_\alpha^2 \rangle} \int_0^{L_0/2} R_{\alpha\alpha}(re_\beta)dr \tag{5.4}$$

are computed. Here, e_β is the unit vector in the β-direction. The integration limit is taken to be $1/2L_0$ because the domain is spatially periodic over the domain length, L_0.

In order to apply periodic boundary conditions, Eswaran and Pope [68] have ensured that the integral length-scale (defined to be the same as the longitudinal integral length-scale) did not exceed 0.3 times L_0. This is very much true in the present simulations. The, longitudinal (L_1) and transverse (L_2) integral length scales are computed using the procedure described in Yeung and Pope [67], i. e. when $\alpha = \beta$ and $\alpha \neq \beta$ in Eq. 5.4, respectively. Here, the ratio of L1 to L2 is 2.3, which is very close to the theoretical value of 2.0 for isotropic turbulence and is in very reasonable agreement with the values predicted (1.87-2.50) by Yeung and Pope [67].

The above study gives confidence that the baseline finite-difference scheme has all the features to accurately capture the small-scale dynamics of isotropic turbulence at moderate Re. Given that background, DNS of two-phase isotropic box and LES are discussed in the following sub-sections.

5.2.2 DNS of momentum coupled two-phase isotropic turbulence

In order to study the two-way coupling between the gas-phase and liquid-phase, the momentum source terms appearing in Eq. 2.2 are included. The grid used for gas-phase computations and other parameters are same as in Section 5.2.1. These simulations were carried out with 32^3 droplet groups, with actual number of particles dictated by the mass-loading (ϕ), density of the particle (ρ_p) and droplet diameter (d_p). The statistical error (which varies as $1/(\sqrt{N})$ from central limit theorem [40]), is less than 1% for the current number of droplets. The statistics were computed as described in Section 5.2.1.

Figure 5.4a shows the effect of droplets on the normalized energy spectrum. In accord with earlier studies (e.g. Squires and Eaton [38]) there is an increase in energy in high wave numbers compared to that of low wave numbers. This is due to the transfer of energy from the large scales by the particles and subsequent transfer to the small scales. Here, the variation with mass loading agrees very well with previous studies [36] [38] and as the mass loading increases, the effect of momentum coupling is more pronounced. Figure 5.4b shows the corresponding dissipation spectrum. Similar to the energy spectrum, there is more dissipation at the small-scales (high wave numbers) compared to the large-scales (low wave numbers). In pure gas phase flows the energy cascades from the large scales to the small scales through the triadic interactions. In two-phase flows this transfer is augmented by the alternate transfer mechanism through droplet interactions with the gas phase, causing additional energy at the small scales which is dissipated as the viscous forces dominate at the small scales.

The increased dissipation of energy is evident in Fig. 5.5a, where the equilibrium

values of the kinetic energy ($1/2q^2$) and mean dissipation ($<\varepsilon>$) are plotted for various mass loadings. These values are normalized by respective quantities for the uncoupled case. It is very evident that kinetic energy of the system decreases because of the dissipation by the droplets. The equilibrium values are thus lower than the corresponding uncoupled case and decrease with increased mass loading. These results are in good agreement with those of Boivin *et al.* [36] and Squires and Eaton [38].

The dissipation skewness which represents the small scale processes, is plotted for various mass loadings in Fig. 5.5b. Here, this higher-order, small-scale parameter increases with increasing mass-loading. This reflects the increased high wave number dissipation and increased activity at the small-scales.

Figure 5.6 plots the transfer energy spectra for various mass loadings. Transfer energy spectrum is calculated using the procedure detailed by Van Atta and Chen [71] using FFT's of triple order velocity correlations. As observed in earlier studies [36] [41] there is a decrease in transfer of energy from large scales to small scales as the mass loading increases. The plot indicates that there is very negligible transfer of energy from low wave numbers to high wave numbers for a mass loading of 2.0. Boivin *et al.* [36] suggested that there is a possibility of 'backscatter' of energy from the small scales to large scales as the small scales are more energetic in the presence of droplets. From the trends noticed in the transfer energy spectrum, beyond this mass loading of 2, there might be backscatter of energy from the small scales to the large scales. These simulations were not carried out in the present study as the particle mass loading increases, particle-particle collisions become important and they are not accounted for in the current formulation.

One of the parameters which characterizes the particle response, is the particle Stokes Number (St). It is defined as $St = \tau_p/\tau_e$ for the present simulations. Here, τ_p is the particle response time given by $\rho_p d_p^2 / 18\mu$ and τ_e is the eddy turn over time calculated using integral length scale and u'. For lower mass loading case (ϕ=0.1), Fig. 5.7a shows the energy spectrum for two-different St values. It is seen that particle response time has negligible effect on the fluid properties. This is also true in the dissipation spectrum plotted in Fig. 5.7b. These results are in very close agreement with those of Boivin *et al.* [36]. In the present case, the particle sizes are still small comparable to Kolmogorov length scales and thus expected to play similar roles in the energy transfer mechanism in the low mass loading cases. Thus, there is very little difference in the kinetic energy and dissipation spectrums.

Isotropic turbulence has energetic eddies traversing at random directions to ensure isotropy in a stationary sense. The droplets interact with these vortex structures and experience forces due to the drag interaction. Droplets with St ~ 1, where the particle response time is of the order of the characteristic eddy time, the interaction between the droplets and fluid is maximum. Centrifugal forces acting on these droplets under these circumstances are strongest, thus leading to accumulation of droplets in the regions of low vorticity. This feature has been observed in isotropic turbulence (e.g. Squires and Eaton [38]) and in forced shear layers (e.g. Lazaro and Lasheras [44]; Martin and Meiburg [45]). Some of the present studies on shear layers has been reported in Chapters VI and VII. The same phenomena has been observed here in Fig. 5.8b, where the droplet

distribution is plotted. This leads to preferential concentration of the particles and the particles thus have a very localized effect instead of a global uniform effect. These effects might cause instantaneous preferential concentration but as the basic flow field itself is statistically isotropic, the evolved two-phase flow is also statistically isotropic. The corresponding vorticity is plotted in Fig. 5.8a. Comparing the two figures one can note the direct correspondence between the flow structures and the droplet concentrations.

In this section, momentum coupling between gas phase and particles has been examined. It has been found that the particles transfer the energy from the large scales to the small scales augmenting the energy cascade in single-phase turbulence. The energy transfer spectrum suggests that as the particle mass loading increases, there is less transfer of energy from the large scales to small scales.

5.2.3 DNS of isotropic turbulence with vaporizing droplets

Starting from an equilibrium solution of the isotropic turbulence with suspended droplets, simulation is carried out with droplet vaporization. The equations governing the droplet heat and mass transfer (Eqs. 2.9 & 2.11) are solved for. This leads to additional source terms in the continuity and species equations, as described in Chapter II and Chapter III. The flow and droplet properties are the same as described in previous section. Since this is a time evolving process and there is continual addition of mass, exchange of momentum and energy (kinetic and thermal), no stationary state can be reached. Furthermore, in a periodic domain, high rates of mass addition and heat transfer are numerically impermissible. Therefore, the present study is limited to a relatively low

vaporization rate.

Fig. 5.9a shows the time variation of normalized kinetic energy spectrum from the time the droplet vaporization is turned on. At the first instant shown there is a rapid accumulation of energy in the small scales. The corresponding increase in dissipation can also be seen in Fig. 5.9b, where the dissipation spectrum is plotted. This state is followed by intermediate states tending to the baseline case of isotropic turbulence with momentum-coupled droplets. This suggests that droplets vaporize at a faster rate, when the temperature of the droplets is higher and there is constant heat transfer from the gas-phase. With time, the gas-phase loses energy and has more concentration of the fuel in the gas-phase. These two factors reduce the heat and mass transfer rates and this is very similar to what is observed by Miller and Bellan [37] in mixing layers. This equilibration might not occur in flows with inflow/outflow conditions and where there is high mass and heat transfer between the phases.

Figure 5.10 shows the vorticity contours and product mass-fraction contours for two different instants. Here, the droplets vaporize and react with the surrounding oxidizer at infinite rate to form the product. The product mass fraction distribution is an outcome of complex droplet-flow, scalar-flow and droplet-scalar interactions. As mentioned in the previous section, droplets of St number of order 1 preferentially concentrate in regions of low vorticity. This is due to the centrifugal forces acting on the droplets. The preferential concentration inturn modifies the vorticity (which is a representation of energy at various scales) since the droplets transfer the energy from the large scales to the small scales. The droplets are also responsible for local mass and heat transfer. These processes lead to

instantaneous non-uniformity of the flow and thus overall preferential concentration of flow variables at any given time. Figure 5.10 reflects this preferential concentration of the droplets in the form of flow variables like vorticity and product mass fraction.

In summary, in this section the effects of vaporizing droplets on the kinetic energy and dissipation energy spectrum are studied. It is found that when the heat and mass transfer rates are considerable, there is sharp increase in the energy of the small scales. It is also found that the product formed through infinite reaction rates between the gaseous fuel and the oxidizer exhibit preferential concentration. The DNS of isotropic turbulence for the various cases has provided valuable information to proceed to the next step of validating LES. The LES of isotropic turbulence are carried out for a wide range of cases and are compared with the DNS results in the next section.

5.3 LES of Isotropic Turbulence

LES of isotropic turbulence for all the cases discussed before are carried out using a dynamic subgrid kinetic energy equation for momentum closures.

Figure 5.11 compares the kinetic energy spectra predicted by the coupled and un-coupled DNS and LES. E(k) is scaled by the average kinetic energy ($1/2q^2$). For uncoupled case (ϕ=0), LES captures the DNS spectra very well at all the resolved wave numbers. For the momentum coupled case (ϕ=0.5), DNS shows an increase of kinetic energy at the high wave numbers. The right trend and magnitude is captured by the LES.

In figure 5.12a, the resolved turbulent kinetic energy normalized by the initial

kinetic energy is plotted for LES. By comparing it to Fig. 5.5a, one can see that the variation of dissipation of energy with increasing mass loading agrees qualitatively. The magnitudes are slightly lower and can be due to the fact that the unresolved energy (k_{sgs}) is not included in the calculation of the kinetic energy. Similar to Fig. 5.5b, Fig. 5.12b illustrates the variation of dissipation skewness with mass loading. Since, dissipation skewness is primarily a small-scale feature, it is not surprising that the magnitude is under predicted since the small-scale energy is not included in the computation of dissipation skewness.

Figure 5.13 shows the transfer energy spectra for various mass loadings for the LES. As observed in the DNS, there is decrease in transfer of energy from large scales to small scales as the mass loading increases. This plot indicates that the LES is qualitatively predicting all the features captured by the DNS.

The vaporization cases have been studied with and without the subgrid model (LEM) for the species closure. Since the vaporization is very low, droplets do not fall below the cut-off diameter. All the droplets are tracked using the Lagrangian tracking scheme and thus the terms S1 and S2 in Eq. 3.14 are zero. As a consequence, the void fraction in the subgrid implementation is zero. However, in the new methodology' all the scalar information is still carried in the subgrid. Furthermore, for the cases reported here the subgrid turbulence is low and so both conventional and LEM based LES approaches are expected to give similar results. Figure 5.14 confirms that no appreciable difference can be seen between the energy spectra predicted by these two LES approaches. As in the momentum coupled case discussed earlier, resolved scale kinetic energy agrees very well

with the DNS. Here, both the LES methods show very good agreement and this indicates that all the scales are accounted for in both procedures.

To evaluate the impact of turbulence modification due to particles, the exponent 'p' appearing in Eqs. 3.11 & 3.12 for computation of length distribution and event frequency has been varied. By changing 'p' from 4/3 (corresponding to -5/3 inertial scaling law) to 1 (corresponding to -2 inertial scaling law) hardly changed the results. This value was chosen arbitrarily to perform the sensitivity analysis and also to reflect the fact that mass addition and presence of particles has made the turbulence spectra at high wave numbers less steeper. This result indicates that the present case is insensitive to slight changes in the spectral characteristics of inertial range in the presence of droplets. In general, this would not be true for high Reynolds number flows where there are larger number of scales spanning the inertial range.

Figure 5.15 shows the normalized product mass fraction spectra for the two different LES methods contrasted with the DNS. As seen in the kinetic energy spectrum, both the LES methods agree reasonably well. The spectrum is under predicted at intermediate to high wave numbers while agrees very well for the low wavenumbers.

Finally, to characterize the particle energy in both DNS and LES, Lagrangian autocorrelation coefficient (Eq. 5.1) of the particle velocities is calculated. Here, the vaporization case is shown where t_0 is the start time for evaporation to begin. Figure 5.16 shows the autocorrelation coefficient for the DNS and LES for St=0.4 and ϕ=0.5. From the figure it is observed that the two LES methods agree well with each other but show lower correlation between the particle velocities in the initial stages reaching the DNS

values at later times.

In summary, DNS using the zero-Mach number incompressible code agrees well with most of the features observed in experiments (for single-phase) and past calculations (for single-phase and two-phases). LES in the current implementation has the capability to model the physics as predicted by DNS both qualitatively and quantitatively to a reasonable extent. The scope of the work is limited to low vaporization and low-Re due to numerical and computational requirements. Within that scope the main feature of the subgrid mixing and vaporization model (LEM) has not been extensively studied. Based on these isotropic turbulence simulations, more extensive studies of high-Re two-phase mixing layers are reported in Chapters VI and VII. Further high-Re studies have to be performed, to prove that LES is a viable tool for high-Re simulations.

Table 5.1: Flow and Computational Parameters

Parameter	Description or Formula	Value
ν	*Kinematic Viscosity*	*0.0125*
L	*Integral Length Scale (= L_1)*	*1.226*
$1/2q^2$	*Turbulent Kinetic energy* $= 3/2u'^2$	*2.995*
η	*Kolmogorov Length Scale* $(\nu^3/\langle\varepsilon\rangle)^{1/4}$	*0.0035*
λ	*Taylor's Length Scale* $= \langle\varepsilon\rangle/15\nu u'^2$	*0.55*
L_0	*Domain Length*	2π
$Kmax*\eta$	*Grid Resolution Parameter*	*2.3*
Re_λ	$u'\lambda/\nu$	*62*
Re_L	$u'L/\nu$	*133*
S_ε	*Dissipation Skewness*	*0.53*
S	*Skewness of Velocity Derivatives* $S = \left[-\frac{1}{3}\sum_{i=1}^{3}\langle(\partial u_i/\partial x_i)^3\rangle\right]/\left[\frac{1}{3}\sum_{i=1}^{3}\langle(\partial u_i/\partial x_i)^2\rangle\right]^{\frac{3}{2}}$	*0.46*
N	*Number of Droplet Groups*	32^3
DNS Resolution	-	128^3
LES Resolution	-	64^3
K_F/K_0	*Forcing Wavenumber Radius*	$2\sqrt{2}$
T_F	*Forcing integral timescale*	*0.6369*
ε^*	*Forcing amplitude rate parameter*	*0.01306*
T_M^*	*Ratio of forcing microscale to T_F*	*0.4*

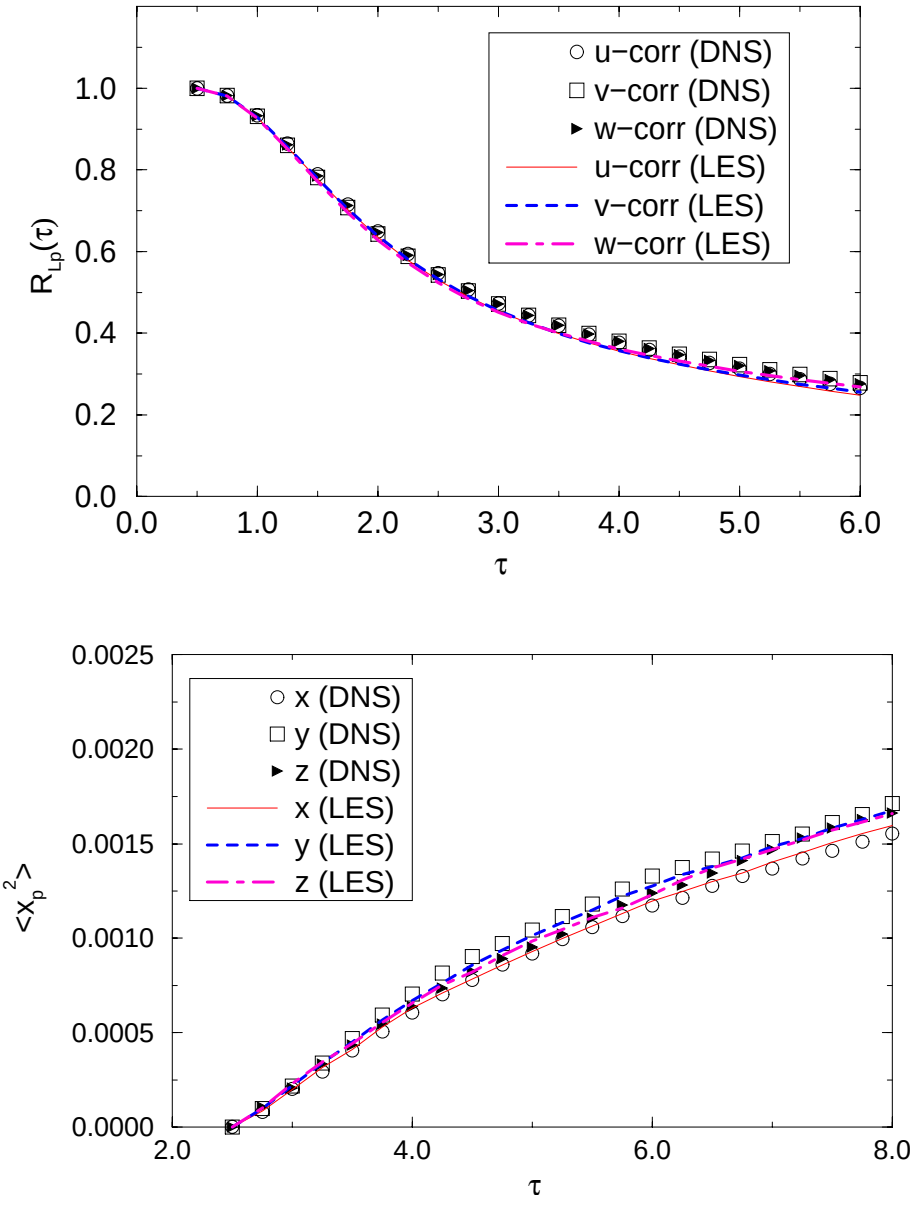

Figure 5.1 Comparison of particle properties in LES and DNS (a) Variation of Lagrangian velocity particle correlations and (b) Variation of mean-square displacements.

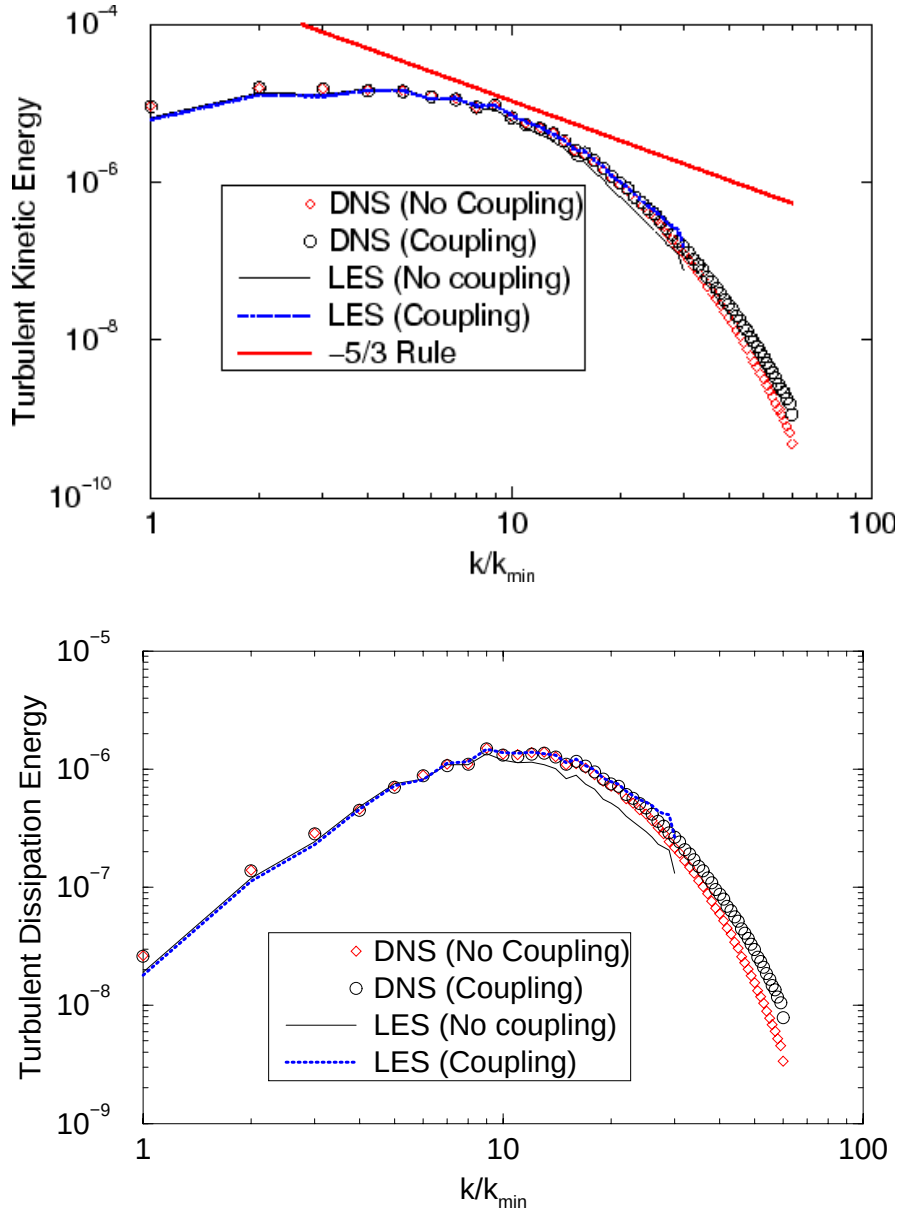

Figure 5.2 Comparison of spectra for LES and DNS with and without coupling. (a) Turbulent kinetic energy spectra and (b) Dissipation spectra.

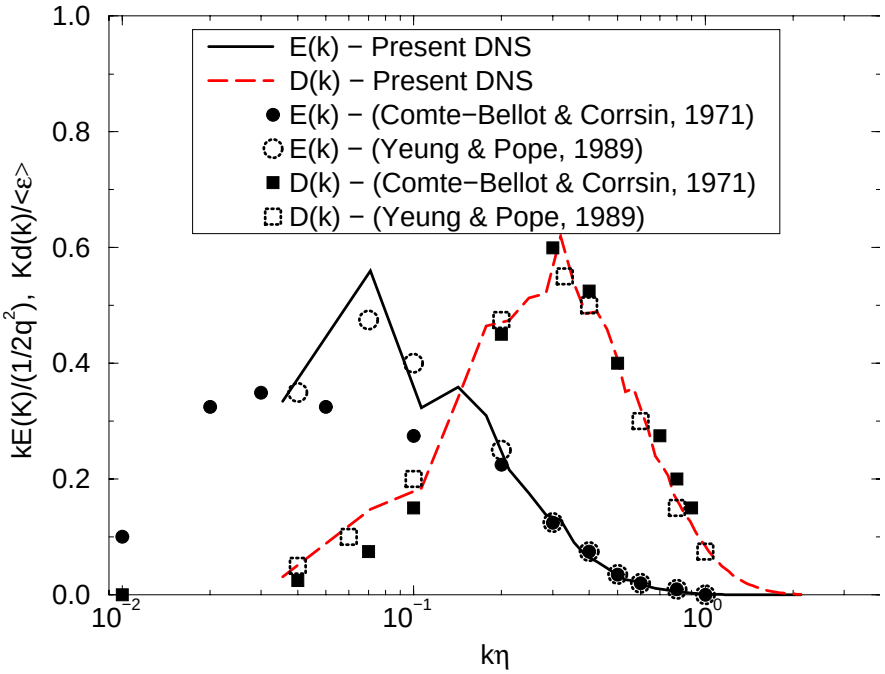

Figure 5.3 Normalized kinetic energy and dissipation spectra compared with experiments and computations of Yeung and Pope [67].

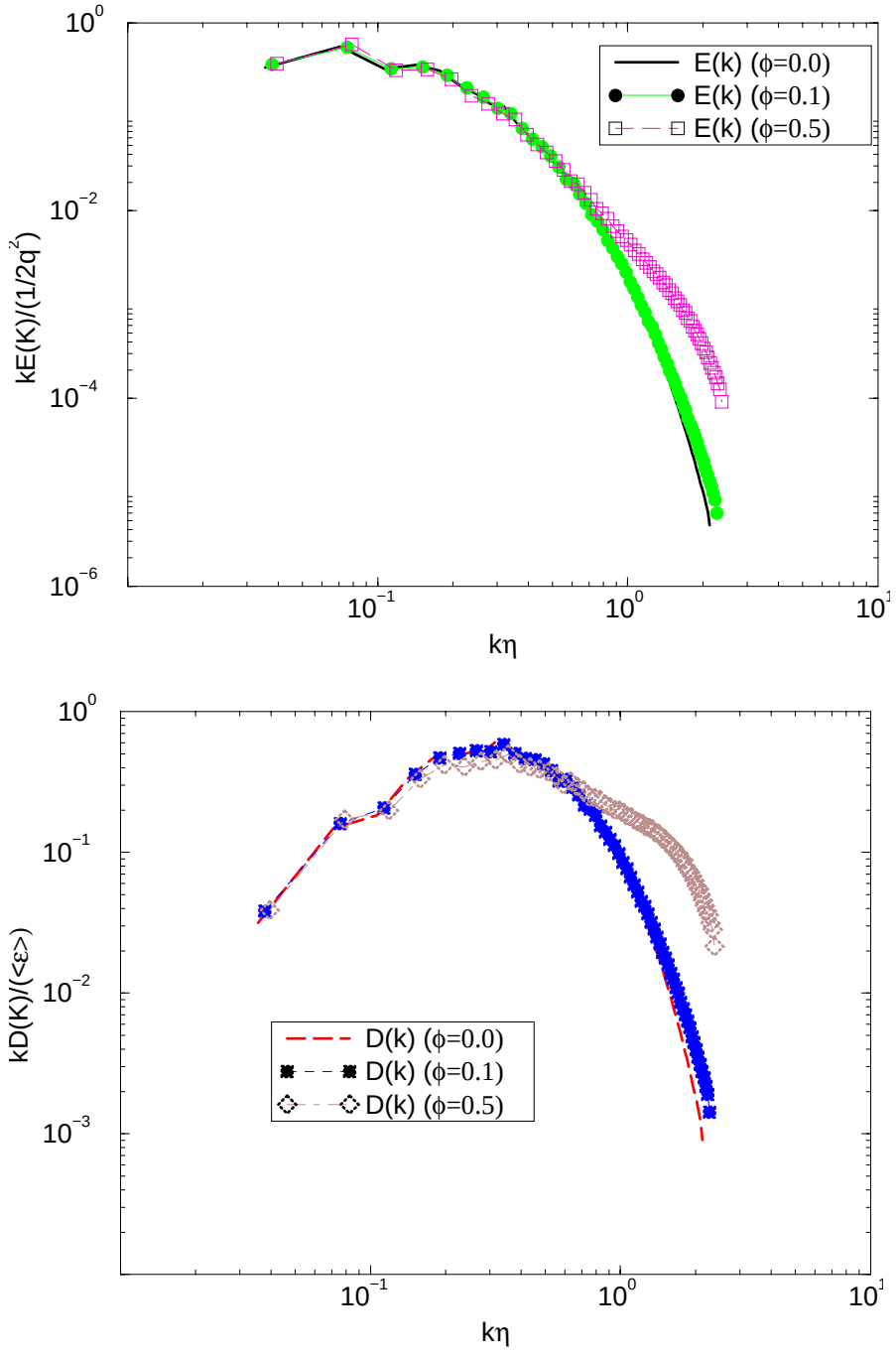

Figure 5.4 Effect of two-way momentum coupling with mass-loading of the droplets (a) Kinetic energy spectrum and (b) Dissipation spectrum.

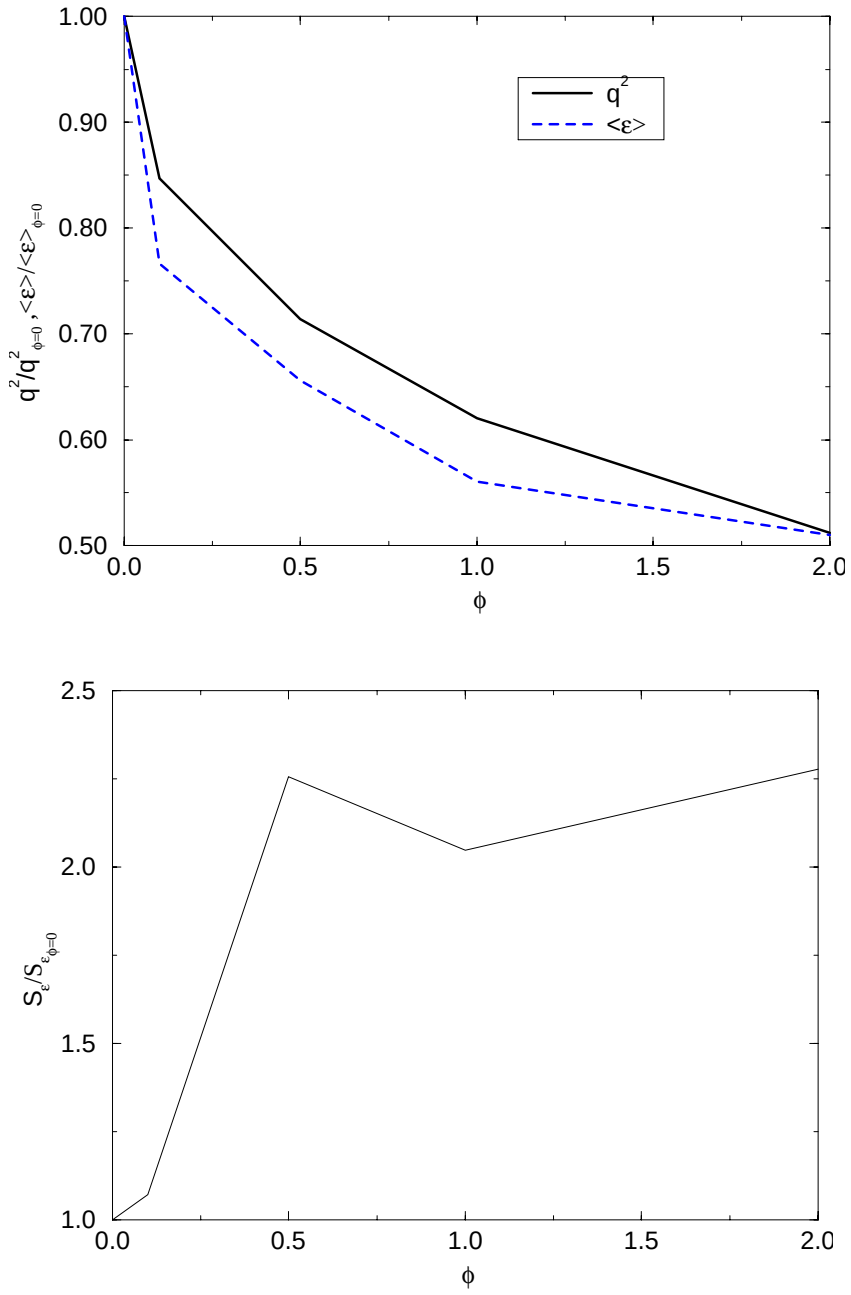

Figure 5.5 Variation of gas-phase properties with mass loading (a) Total kinetic energy and dissipation rate and (b) Dissipation skewness.

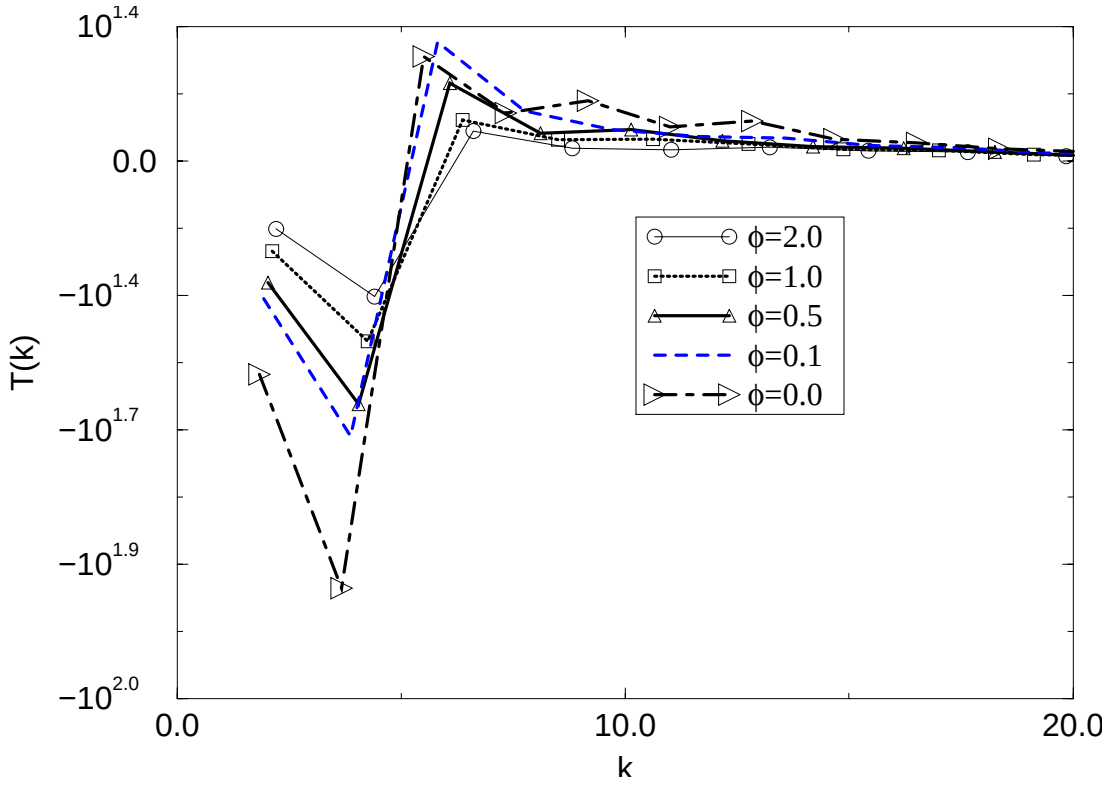

Figure 5.6 Effect of mass loading on the evolution of the transfer energy spectra.

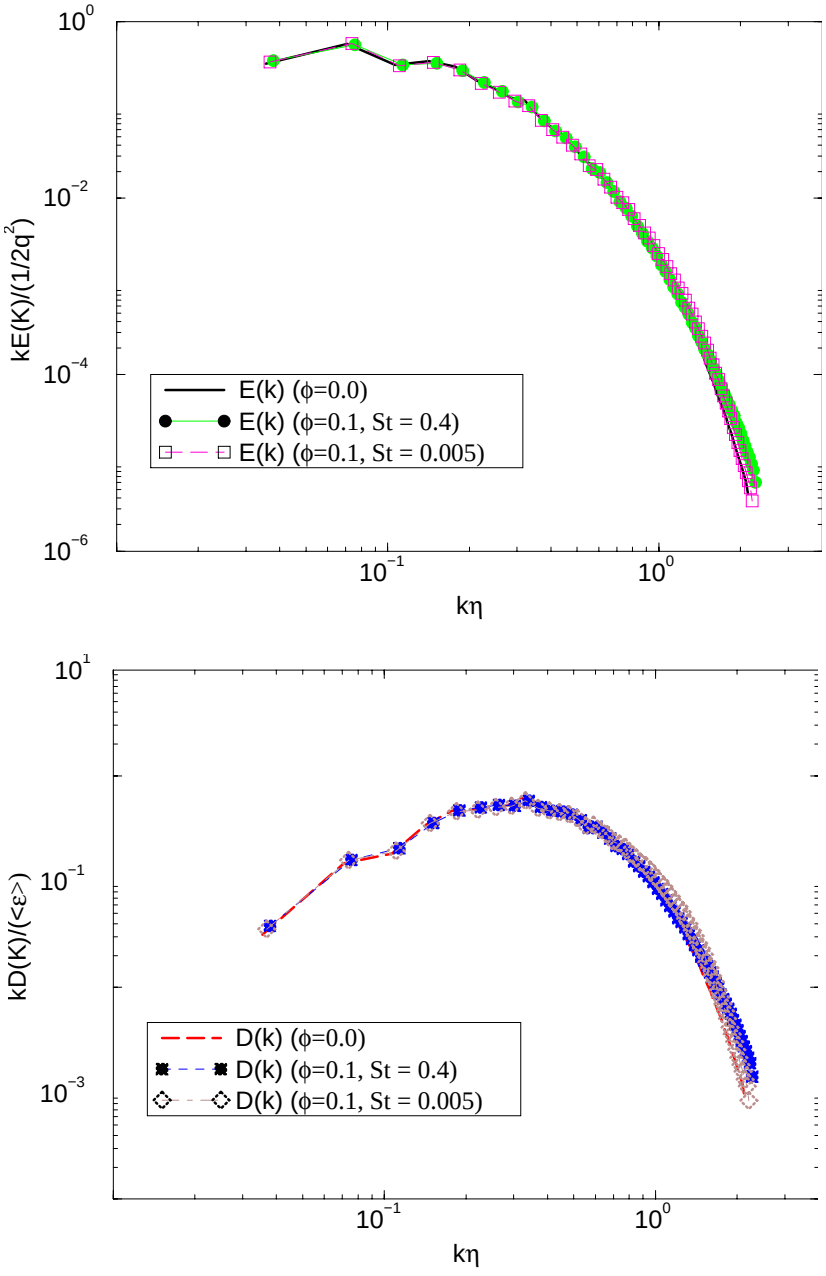

Figure 5.7 Effect of two-way momentum coupling with Stokes number of the droplets (a) Kinetic energy spectrum and (b) Dissipation spectrum.

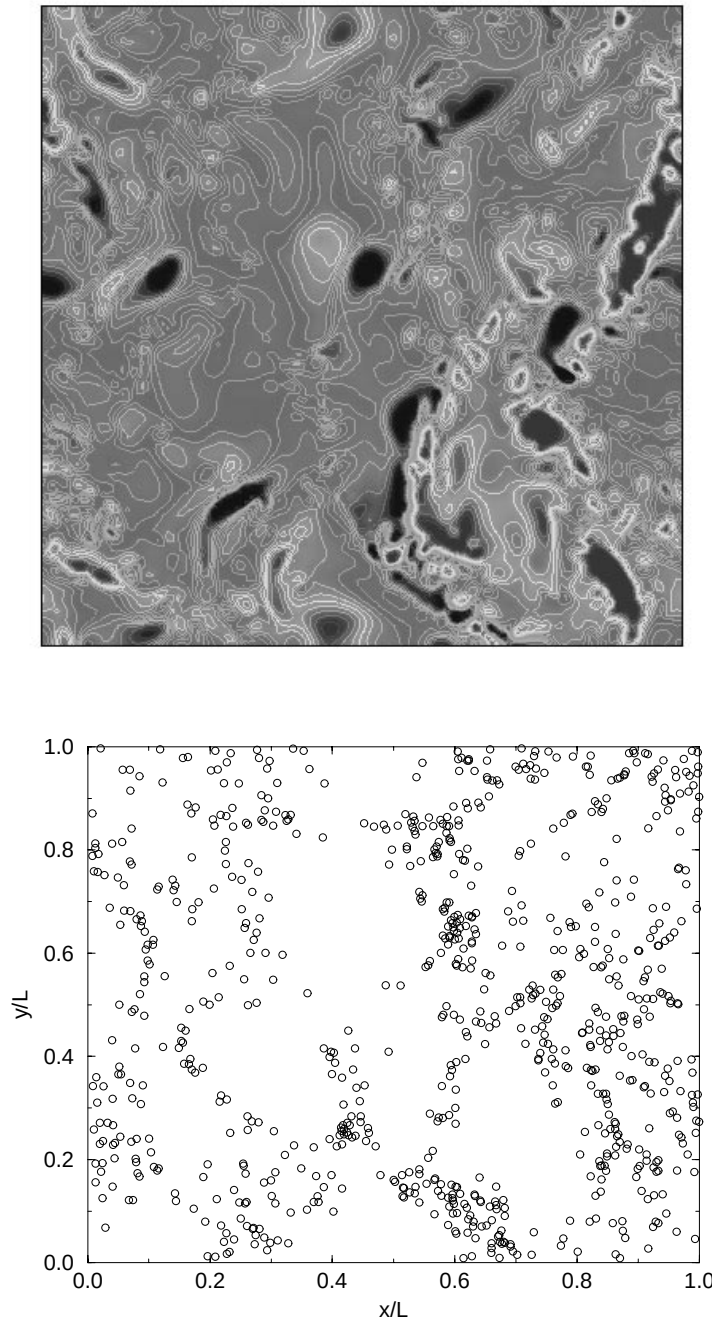

Figure 5.8 Preferential concentration of droplets in low-vorticity region (St = 0.4) (a) Spanwise vorticity and (b) Spatial distribution of droplets in the spanwise direction.

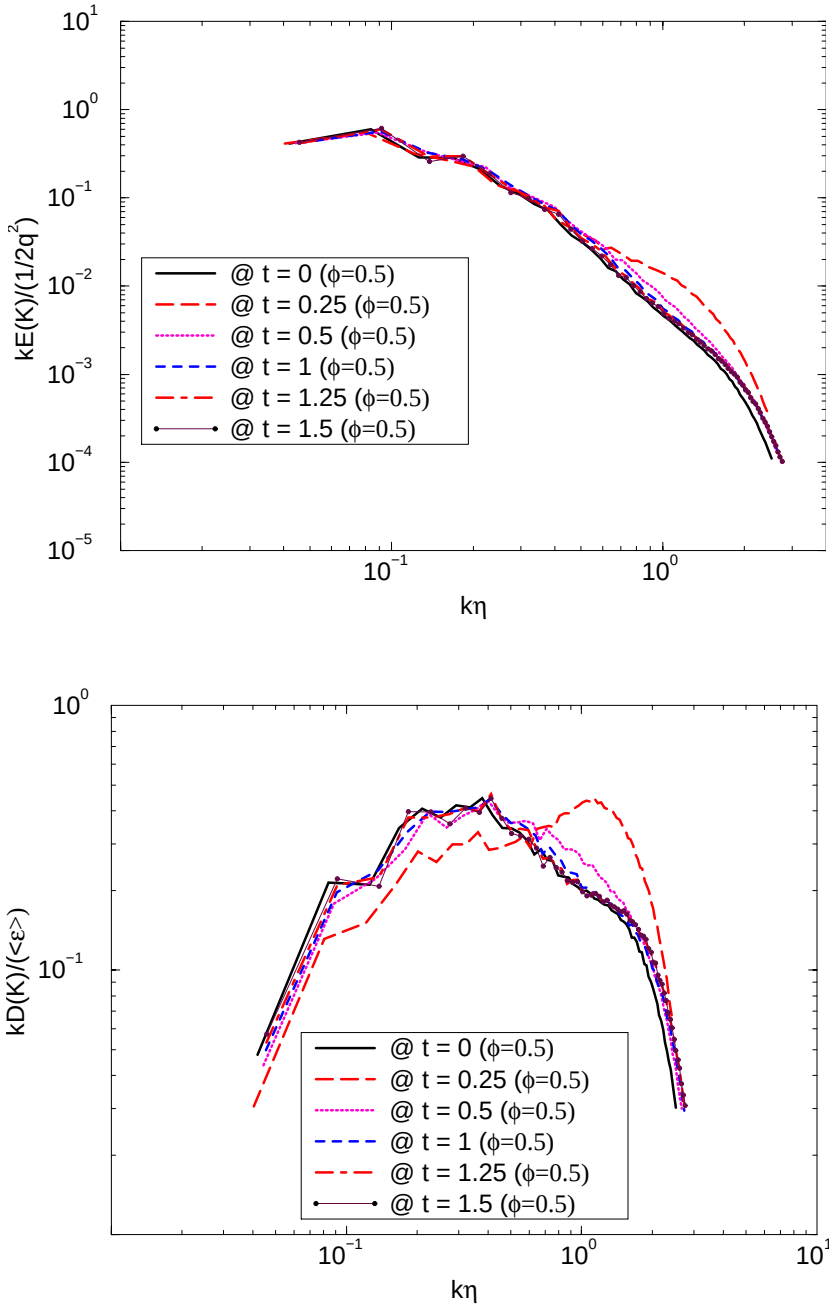

Figure 5.9 Time variation of effect of two-way coupling with vaporizing droplets (a) Kinetic energy spectrum and (b) Dissipation spectrum.

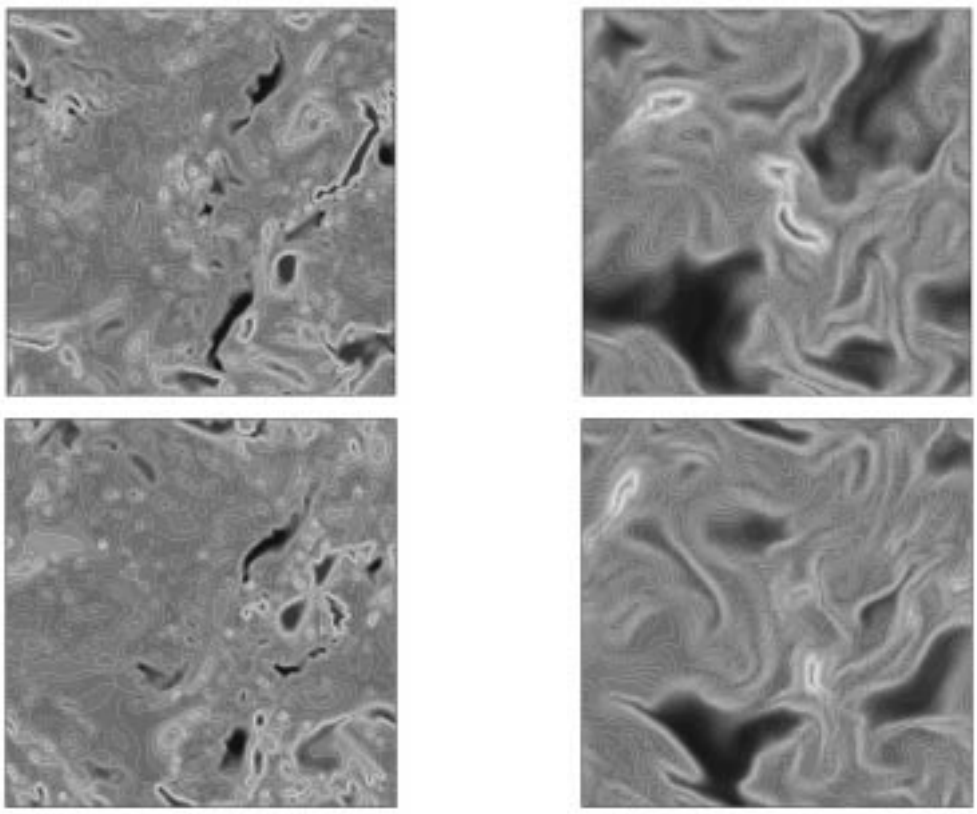

Figure 5.10 Snapshots of span-wise vorticity (left) and product-mass fraction distribution (right) at two different time instants for St=0.4 and ϕ=0.5.

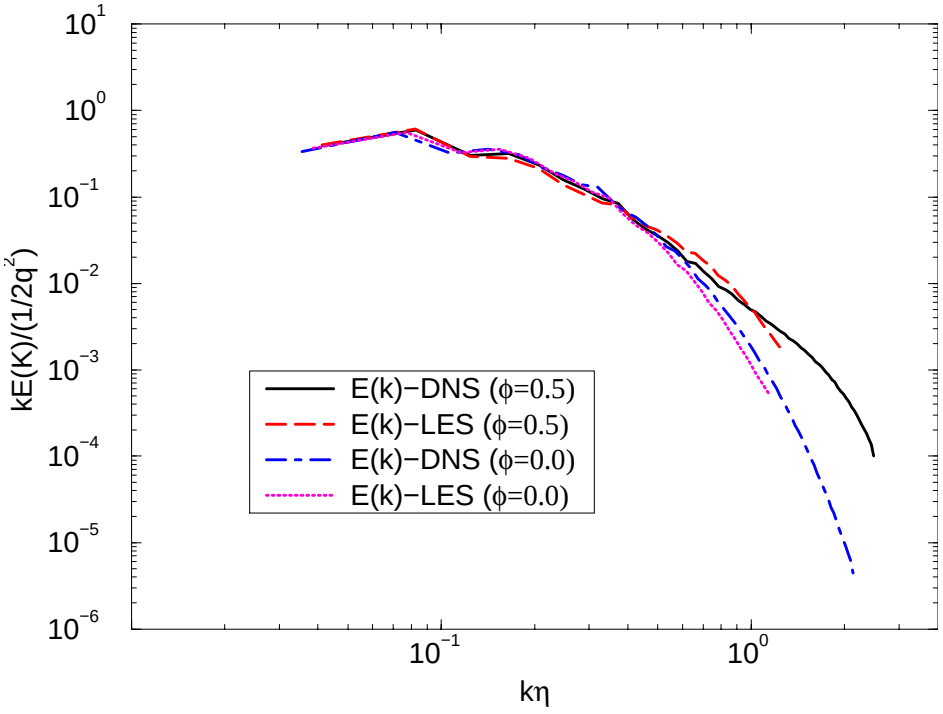

Figure 5.11 Comparison of kinetic energy spectrum of LES with DNS for two-way momentum coupling for St=0.4.

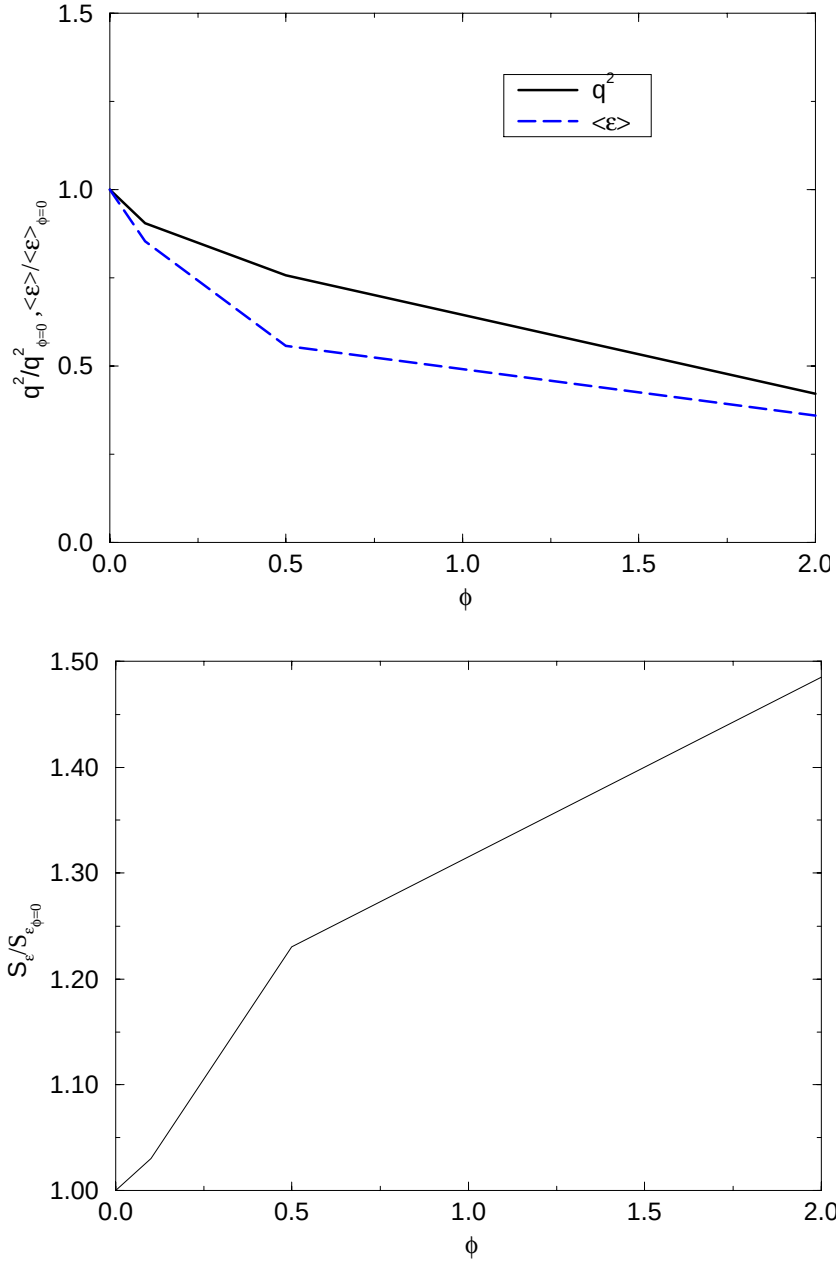

Figure 5.12 Variation of gas-phase properties with mass loading as predicted by LES (a) Resolved total kinetic energy and dissipation rate and (b) Dissipation skewness computed using resolved scale field.

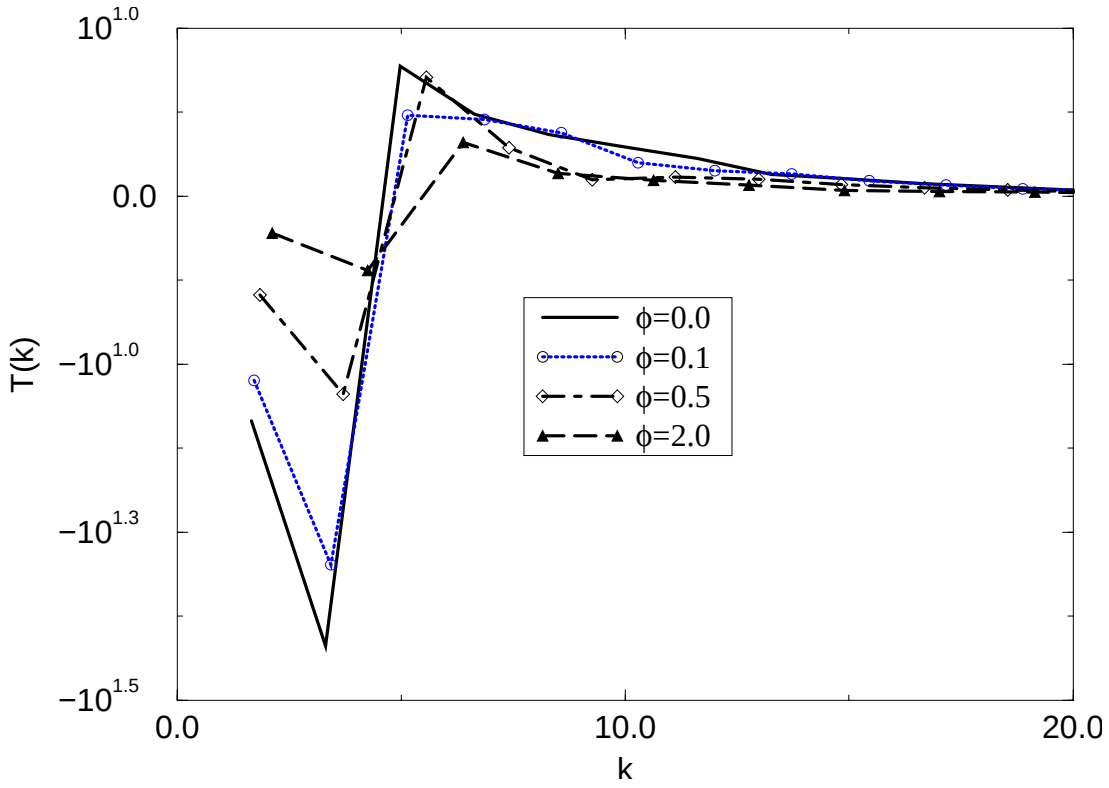

Figure 5.13 Effect of mass loading on the evolution of the transfer energy spectra.

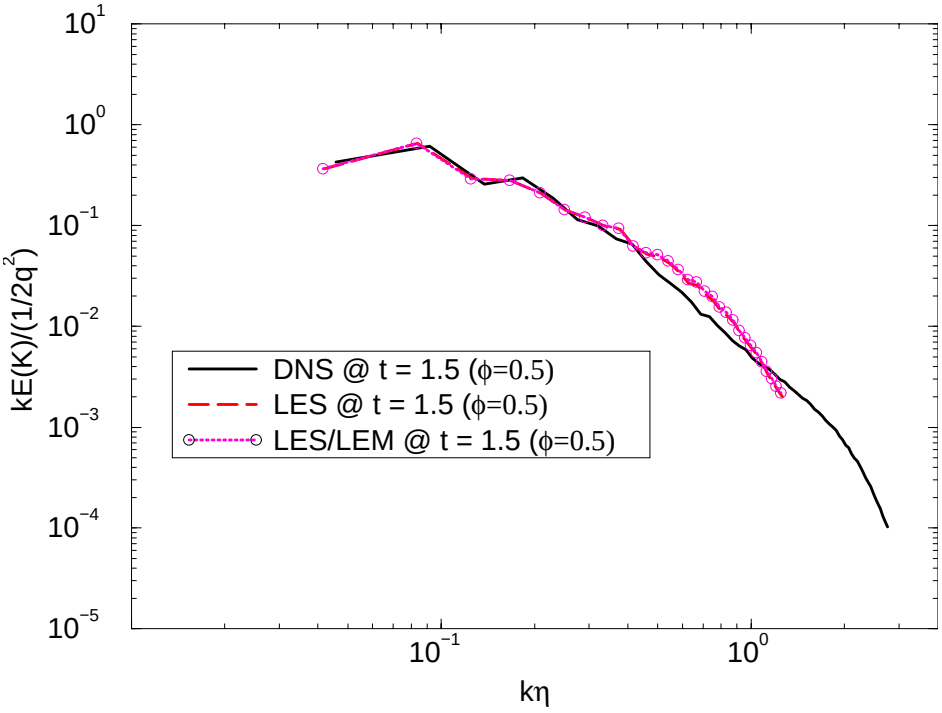

Figure 5.14 Comparison of kinetic energy spectrum of LES with DNS for two-way coupling for vaporizing droplets of St=0.4

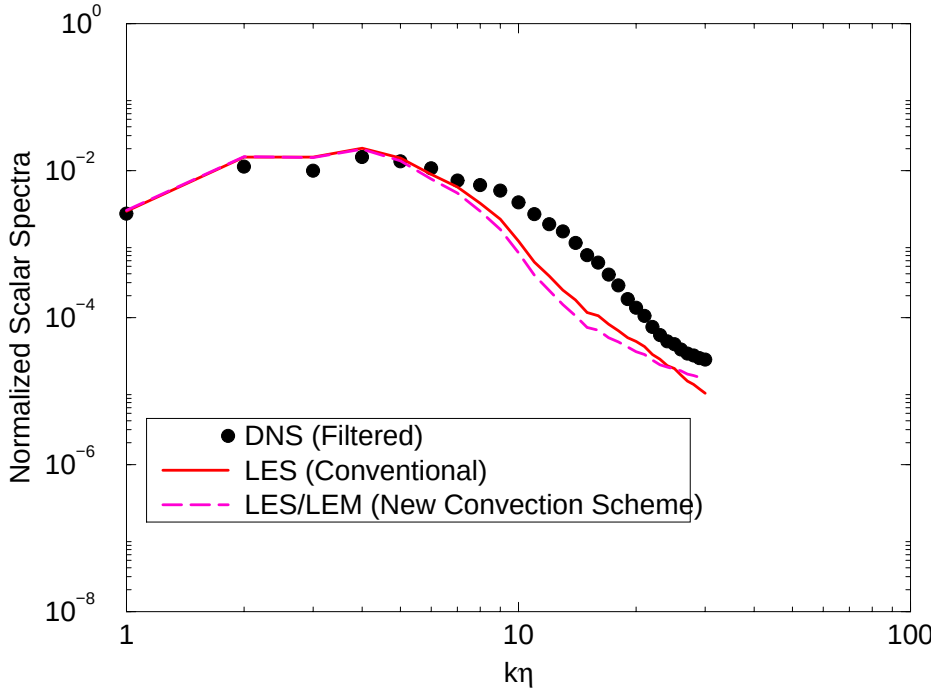

Figure 5.15 Normalized product mass fraction spectra of LES is compared with DNS for two-way coupling for vaporizing droplets of St=0.4.

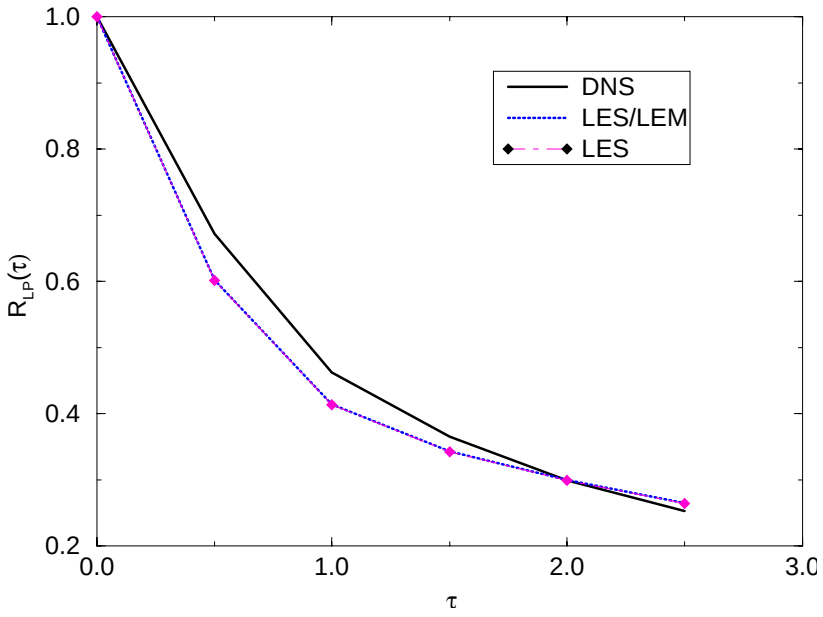

Figure 5.16 Time evolution of particle velocity autocorrelations for St=0.4 and ϕ=0.5 with vaporizing droplets.

CHAPTER VI

TEMPORAL MIXING LAYERS

In this chapter, particle dispersion in presence of strong coherent vortices is studied using temporal mixing layers. The effect of both vaporizing and momentum coupling due to droplets on the large scale structures is explored at length as this gives further understanding into the physics of two-phase flows. The sensitivity of the conventional LES is evaluated against current approach for different droplet cut-offs.

6.1 Non-vaporizing Particle Dispersion in Mixing Layers

The Lagrangian approach of particle tracking is qualitatively/semi-quantitatively validated through the use of temporal mixing layers before simulating reacting flows. Although quantitative comparison with earlier studies is difficult due to differences in the set up and/or initial conditions, qualitative comparison can be carried out. For this purpose, simulations of the mixing layers studied by Lazaro and Lasheras [43] [44] and simulated by Martin and Meiburg [45] using a 2D vortex method, are carried out here. Here, a 3D approach was employed and a temporal mixing layer was simulated. The mixing layer is initialized by a tangent hyperbolic mean velocity along with the most

unstable 2D (of dimensional wavelength 2π) mode and random 3D turbulence (similar to that described in [72]). Simulations for relatively low Reynolds number ($\delta_\omega \Delta u/\nu$, based on vorticity thickness and velocity difference) of approximately 200 are carried out using a grid resolution of 64x64x64. The particles were injected in every cell of the upper stream with velocities equal to the local cell values. The total number of particles tracked is 110,000. This case is very similar (except for the high resolution both in grid and number of particles, the differences in the initial forcing and use of a simplified particle drag in the earlier case [45] using Stokes law) to the direct simulation of [45]. Using the 0.9-0.1 level thickness (δ_L) (defined as the distance between the cross-stream locations where the particle concentrations are 90% and 10% of the reference value, respectively [44]), particle dispersion was computed for a range of Stokes numbers. Here, Stokes number is defined as:

$$St = (\rho_p d_p^2 / 18\mu)\Delta U / \delta_\omega \tag{6.1}$$

where δ_ω is the vorticity thickness and ΔU is the velocity difference between the upper and lower stream.

Figure 6.1 shows the dispersion of particles (in terms of the dispersion thickness) with time for a range of Stokes numbers. It can be seen that the dispersion of particles of order St=1 exceeds that of droplets with St<1 (i.e., smaller droplets). The results obtained by Martin and Meiburg [45] are also plotted in filled symbols along with the present

simulations in Fig. 6.1. The same trends are qualitatively captured by the present simulations. Note that the variations between the two results are possibly due to the differences in the initial forcing parameter and the Stokes drag (neglecting the particle Reynolds number correction assumed in [45]). The increased dispersion of particles of St ~ 1, is similar to the phenomena observed earlier in both experimental [44] and numerical [45] studies and was attributed to the increased lateral dispersion of the particles when the aerodynamic response time is of the order of the characteristic flow time. This is due to the centrifugal forces acting on the droplets acting on this range of droplets leading to increased dispersion. The increased particle dispersion leads to the formation of narrow band of particles on the vortex peripheral on the lower side for St=5 as shown in Fig. 6.2a. These results also agree qualitatively with earlier experiments [44] shown in Fig. 6.2b.

6.2 Droplet Vaporization in a Mixing Layer

Droplets were injected into the core of a temporal mixing layer (described in section 6.1) to eliminate any interference from the walls at time t=0 for the study of droplet vaporization. The mixing layer is simulated using a grid resolution of 32x32x32 and 64x64x64. The results with these two grid resolution numbers showed good agreement thus indicating grid independence.

The mixing layer is initialized with the oxidizer in both the upper and lower streams at 350^{o} K. A range of droplets from 10-50 micron radius with an initial

temperature of 300 K was used for all simulations with the droplet cut-off radius set at 5 micron. A total of 2100 droplet groups were tracked. The results using relatively higher number of groups (~10,000) were very similar and thus the lower resolution case was used for all the simulations reported here. In any case, lower resolutions is preferred to demonstrate the capability of LES. For simplicity, the droplet groups were uniformly distributed and the number of droplets in each group was prescribed such that the overall mass loading is 0.5 which corresponds to a volume loading of 0.0005. The mass loading chosen here corresponds to typical mass loadings in the dilute phase regime of liquid fuel based combustors.

Figure 6.3a shows the spanwise vorticity contours in the mixing layer at the roll-up stage for a case in which the particles are passively transported upon insertion (i.e., no vaporization included and hence, there is no coupling between the two phases). It can be seen that the shear layer rolls into coherent structures as seen in pure gas phase flows. However, when droplet vaporization is included (Fig. 6.3b), the associated heat absorption results in major changes in the shear layer. The formation of the coherent spanwise vortices is inhibited due to vaporization and mass addition to gas phase. Although the extent of the mixing layer appears to be large, the peak value of the spanwise vorticity is substantially lower for the vaporizing case. Analysis shows that, in the vaporization case, significant 3D vorticity is generated and this plays a major role in inhibiting the spanwise coherence.

The enhancement of streamwise vorticity can be visualized by comparing Figs. 6.4a and 6.4b which show, respectively, the streamwise vorticity for the non-vaporizing

and vaporizing cases. Here, the same contour interval was used for direct comparison. The 3D nature of the shear layer can be clearly seen in these figures. The comparison also indicates that the droplets generate additional streamwise vorticity in the vicinity of droplets. Further insight can be obtained by looking at various terms in a vorticity transport equation. The generalized vorticity equation in 3-D can be written as:

$$\frac{D\omega}{Dt} = (\omega \bullet \nabla)v - \omega(\nabla \bullet v) + \frac{\nabla\rho \times \nabla p}{\rho^2} + \frac{1}{Re}(\nabla^2\omega) \qquad (6.2)$$

Four different mechanisms [49] can modulate vorticity. The terms on the right hand side of Eq. 6.2 are respectively the vortex stretching, the thermal expansion, the baroclinic torque and the viscous diffusion.

The spanwise component of the baroclinic torque is shown in Fig. 6.5a. This indicates that vaporization produces significant baroclinic torque. This production plays a major role in redistributing the vorticity in the mixing layer. This can be confirmed by calculating the various terms in the 3D vorticity transport equation. For example, the expansion term $\varpi(\nabla \bullet \vec{v})$ in vorticity equation Eq. 6.2 is shown in Fig. 6.5b. Comparison with Fig. 6.5a indicates that baroclinic term dominates in this case. Interestingly, this behavior is quite similar to the case when heat is released [49] except that, in the present case, heat is absorbed and the temperature is decreasing.

The droplet distribution for the above two cases is shown in Figs. 6.6a and 6.6b, respectively. The Stokes number for all the droplets tracked is in the range of 0.0004 to

0.01. As expected, the droplets follow the fluid motion and this behavior qualitatively agrees with the results described in [73]. The droplet distribution between the two cases is slightly different due to the modulation of the vortex structures as a result of vaporization as discussed in the above paragraph. The effect of the decrease in the strength of the vortex structures and the formation of new smaller vortex structures leads to further dispersion of the droplets and a thickening of the braid region.

In the simulations described above, the continuity, species and energy equations are solved in the supergrid in addition to the momentum equations. The droplets are tracked by the Lagrangian tracking scheme. In conventional schemes all the droplets are tracked by the Lagrangian tracking scheme till they reach the cut-off size and below which they are assumed to vaporize instantaneously. In these studies, as the subgrid Re is very low, the subgrid resolution necessary for capturing all the scales was less than 30 cells. Grid independence tests with as many as 100 cells have resulted in similar results. In order to evaluate the convection algorithms, both the splicing algorithms (one based on transfer of cells and the other based on transfer of scalar field properties) are used. Fig. 6.8 plots the variation of product mass fraction across the mixing layer for the two-cases. It has been found that in this case with uniform grid and in the presence of a mean flow direction, both the convection algorithms give near identical results. In all the cases reported below, the former convection algorithm based on cell transfer is used.

Note that if the droplet cut-off size is chosen such that no droplet falls below the cutoff, then the void fraction is zero. In this case, the present LES and the conventional LES approaches should agree reasonably well. The only difference between the two

approaches is that the new approach simulates the scalar fields in the subgrid and therefore, the phase change of the Lagrangian droplets will appear as a source term (S_L) in the subgrid gas density and the subgrid fuel species equations (Eq. 3.13 & Eq. 3.14). In contrast, the conventional LES will solve the species conservation equations along with the other LES equations and phase change source term will be used in Eq. 2.4.

The spanwise and streamwise vorticity for the conventional and subgrid approach are shown in Figs. 6.7a and 6.7b, respectively, and correspond to Figs. 6.3b and 6.4b for the conventional case. The effect of vaporization on shear layer is qualitatively similar in nature but the magnitude is much higher for the subgrid approach. This can be due to the fact that in LEM approach phase change occurs in the subgrid and small scales not directly accounted for in the conventional simulations are resolved within the subgrid.

Calculations using infinite rate kinetics, i.e., when the vaporized fuel mixes with the oxidizer and instantaneously reacts, were carried out for the case when all drops are larger than the cut-off size. The product mass fraction, which is the ratio of the product density to the overall gas density, predicted by the conventional and the new LES approaches is compared in Fig. 6.9a. It can be seen that there is very good agreement between the two methods. This is expected considering the fact that the subgrid Reynolds numbers are very low and the mean quantities are compared here. The predicted temperature of the gas phase (Fig. 6.9b) also shows good agreement. Within the scope of the conditions used in this study, these results confirm the validity of the new LES approach.

The conventional LES assumes that as droplets fall below the cut-off size they

instantaneously vaporize and mix. This can result in significant error especially if the cut-off size is large. As a result, to maintain good accuracy, conventional LES requires a very small cut-off size. This, in turn, increases the computational cost considerably. Since the new subgrid approach is supposed to take care of the vaporization process even in the subgrid, it should be able to deal with an increased cut-off size without adversely affecting the accuracy. This is demonstrated below by simulating identical problems but with different cut-off sizes of 10 and 20 microns.

The subgrid void fraction models, Eqs. 3.9 & 3.13, have no explicit droplet size information other than in the source terms. The source term S_2 represents the vaporization of the liquid in the subgrid and is generally a function of the droplet size. The expression for S_2 is same as in Eq. 2.9. It was determined that as the droplet cut-off size is increased, the subgrid vaporization model for S_2 needs to represent the droplet distribution from the cut-off to the smallest possible size. This requirement is qualitatively similar to the need to characterize (and pick) the eddy size that causes the turbulent mixing process in the subgrid as described in section 3.2.1. To account for this droplet size distribution, the S_2 term (Eq. 2.9) picks a representative droplet size from a distribution within the subgrid. In general, the droplet size should be picked at random from the distribution similar to the manner the eddy size is picked for turbulent stirring. However, at present, the droplet sizes are picked using representative drop sizes. The simple formula which is used to randomly pick the droplet size is based on the fact that the droplet life time drastically reduces as the droplets become smaller and smaller. If the

droplet cut-off diameter is d_c, minimum droplet size is d_{min} and the range of droplet groups is d_{range}, then droplet size picked is (d_c+d_{range}/2.0) with probability 0.667 and (d_c-d_{range}/2.0-d_{min}) with probability 0.333. This is just a representative distribution to mimic the actual exponential decay observed in the experiments. It is found here that the results are not very sensitive to slight variations in the chosen distribution as long the decay nature is preserved. The number of bins have to be increased if we go for higher cut-off size to represent the characteristics of the droplets more precisely. For example three bins have been used for cut-off radius of 30 microns. This distribution can be an input from the experimental data against which the comparisons are made or for the type of liquid fuel being used.

The new approach shows significant advantage over the conventional approach even using the assumptions stated earlier. For example, the product mass fraction obtained by the two LES methods are compared in Figs. 6.10a and 6.10b, respectively, for the various cut-off sizes. The results predicted by the conventional LES are in gross error for cut-off radius of 10 and 20 microns. This error is due to the fact that there is unphysical addition of mass and energy into the gas-phase instantaneously. This leads to unrealistic flow and reactions. In contrast, the present methodology agrees very well over the cut-off range and predicts nearly identical results for a range of cut-off sizes upto 30 microns cut-off size. The observed differences in the spread are due to slightly higher vaporization rates in the peripherals of the mixing layer. This may be related to the fact that there is some error introduced as even the droplets below the cut-off have drag, which can not be handled in the subgrid domain as the momentum equation is not solved.

The same results have been obtained for the temporal mixing layers under different set of conditions (lower forcing of the fundamental mode and higher initial random turbulence). The product mass fraction for this case is plotted in Fig. 6.11. This plot clearly demonstrates the insensitivity of cut-off size on the results with the LEM/LES model.

The above results clearly suggest that with the new approach a larger cut-off size can be used without losing any accuracy. This has important implications for the computational effort since the present subgrid approach is much more expensive when compared to the conventional method for the same cut-off size. Thus, increasing the cut-off size should offset the increased cost of the subgrid model. The increased cost associated with tracking small droplets is two-fold. First the number of droplets to be tracked increases and thus the computational expense associated with it. Second, as the droplet size drops the characteristic times of the droplet (relaxation time, life time, etc.,) reduce considerably resulting in decrease in the time-step of integration. In fact, a conventional LES using 15,000 particles and a cut-off size of 2.5 micron is nearly 4-5 times more expensive than the subgrid LES approach which used a 10 micron cut-off. This result provides confidence that the new approach will be both more cost effective and more accurate than the conventional approach. This result also has other implications in large-scale parallel computations of two-phase flows. The variation of the droplet sizes dictates the time-step for integration of the Lagrangian transport equations for the droplets. The droplet relaxation times and the droplet life-times vary as the square of the droplet size. This creates a huge imbalance between the time-steps between the various groups and thus can lead to severe load-imbalance on massively parallel computers. This

can lead to degradation of parallel performance. The present approach reduces this imbalance by using a subgrid process which is efficiently parallelizable.

Finite-rate Damkohler number (Da) effects without heat release were also investigated. It was seen that as the chemical time scale decreases (Da increases), the product mass fraction increases, in agreement with earlier results and physics. Due to finite-rate effects, there is a considerable amount of unreacted fuel in the gaseous form. In addition to the droplet temperature and the surrounding oxidizer concentration, the amount of fuel present in the gaseous form dictates the liquid to gaseous fuel phase change. Thus, the vaporization rate is coupled to the rate of chemical kinetics, heat release and the other processes such as convection.

The new approach is able to capture the Da effects without error when the cut-off size is increased. For example, the product mass fractions for a Da=100 case computed using the conventional approach are shown for various cut-off sizes in Fig. 6.12a and the corresponding results obtained using the new LES approach are shown in Fig. 6.12b. As seen earlier for the infinite-rate kinetics, increasing the cut-off does not adversely affect the predictions by the present LES whereas, the conventional LES results in significant errors. Furthermore, since the present method can deal with differential diffusion quite easily, Schmidt number effects can also be studied.

In summary, temporal mixing layers are simulated with vaporizing and non-vaporizing droplets. The effects of coupling on mixing layers dynamics indicate that baroclinic torque redistributes the energy and the vortex roll-up is considerably inhibited. The new feature of the hybrid Eulerian-Lagrangian model is quite insensitive to droplet

cut-off size unlike the conventional Lagrangian model. This work is extended for spatial shear layers in Chapter VII.

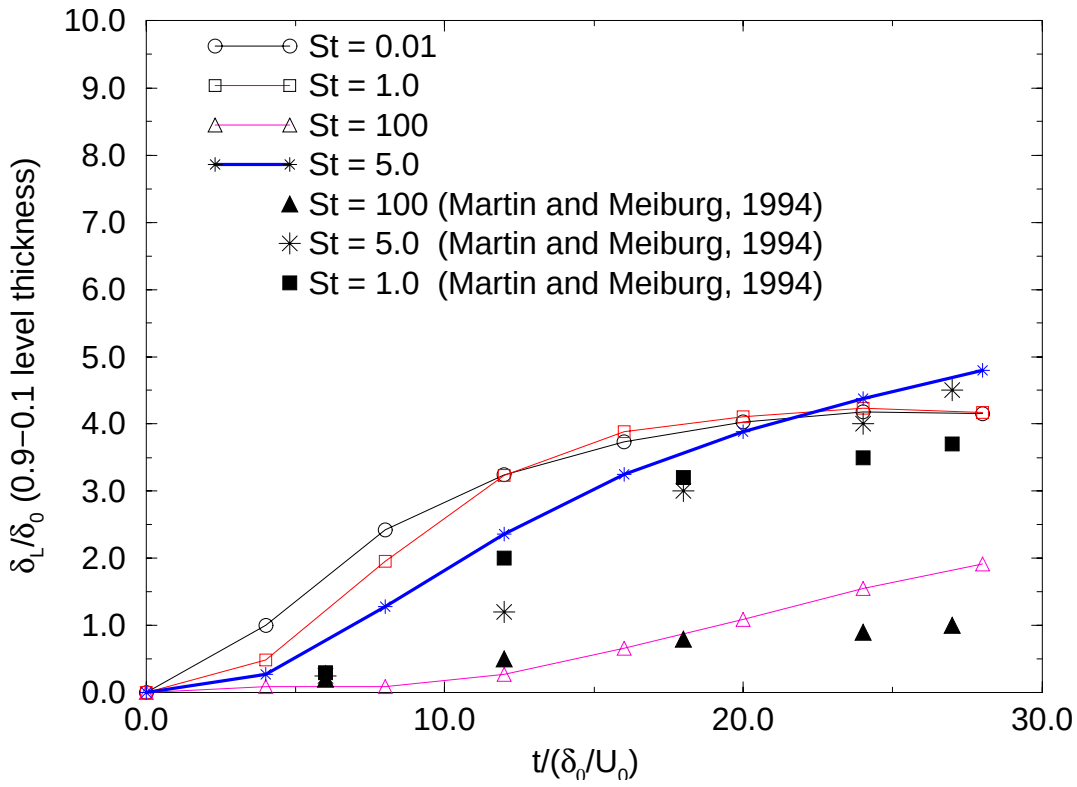

Figure 6.1 Evolution of the 0.9-0.1 particle concentration level thickness for various St.

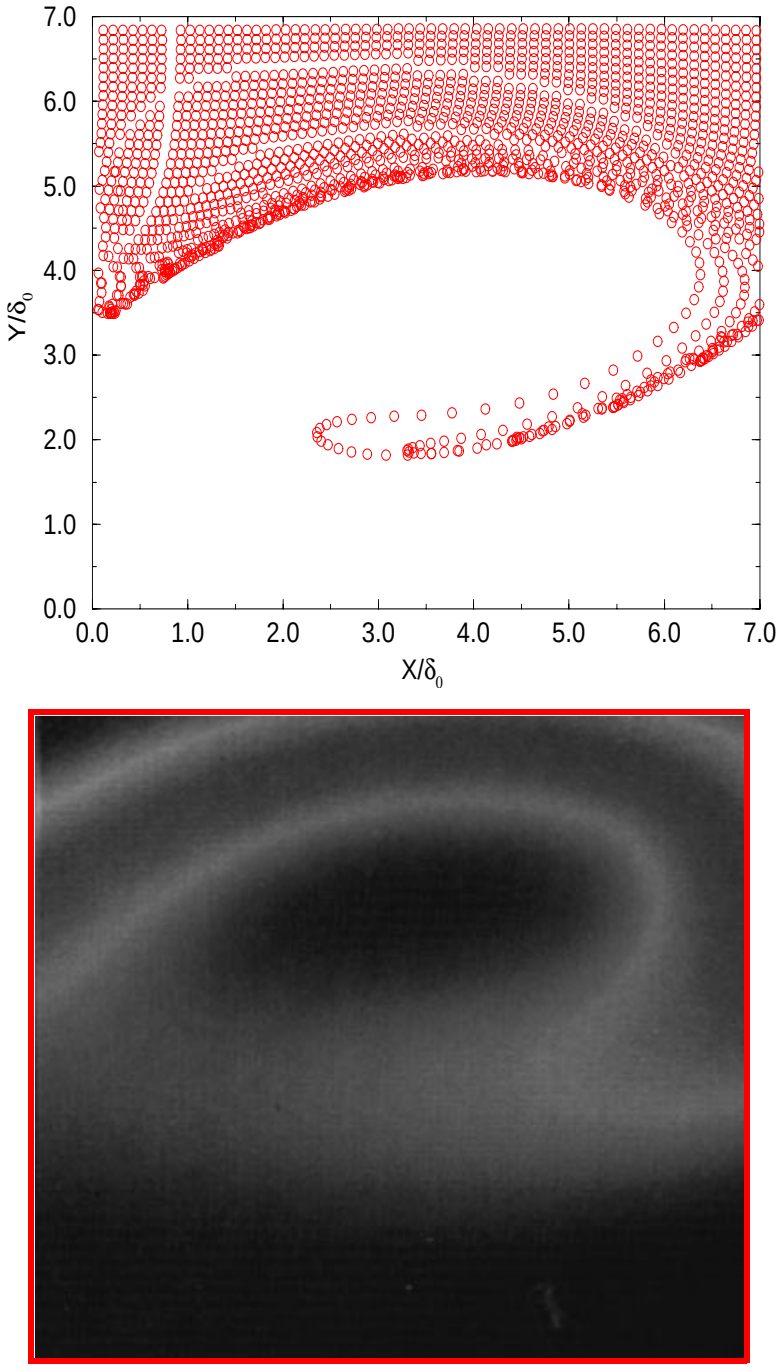

Figure 6.2 Droplet distribution in the X-Y plane (a) Simulation with St. = 5.0 at t=18 and (b) Flash pulse visualization of Lazaro and Lasheras (1992).

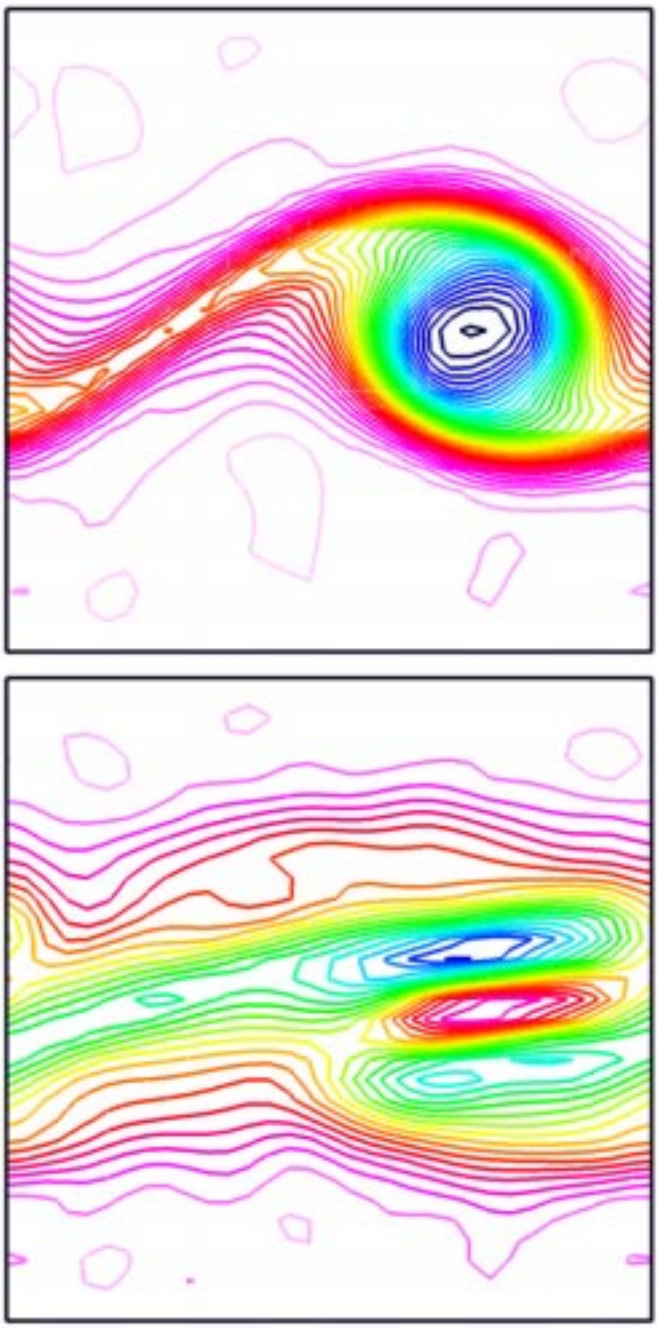

Figure 6.3 Spanwise vorticity in the mixing layer (a) Without liquid-gas coupling from droplets and (b) With liquid-gas coupling. Note: Contour interval level = 0.0374.

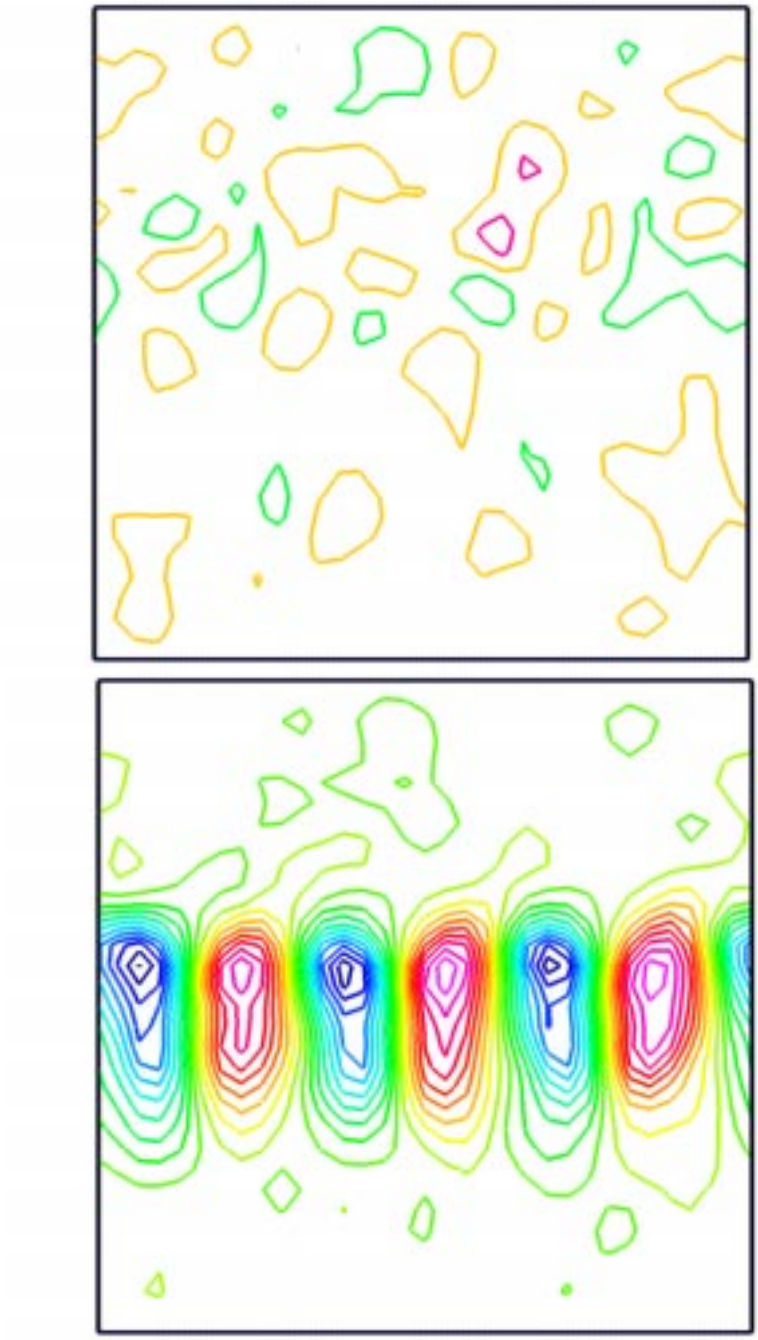

Figure 6.4 Streamwise vorticity in the mixing layer (a) without liquid-gas coupling and (b) with liquid-gas coupling. Note: Contour interval level = 0.03

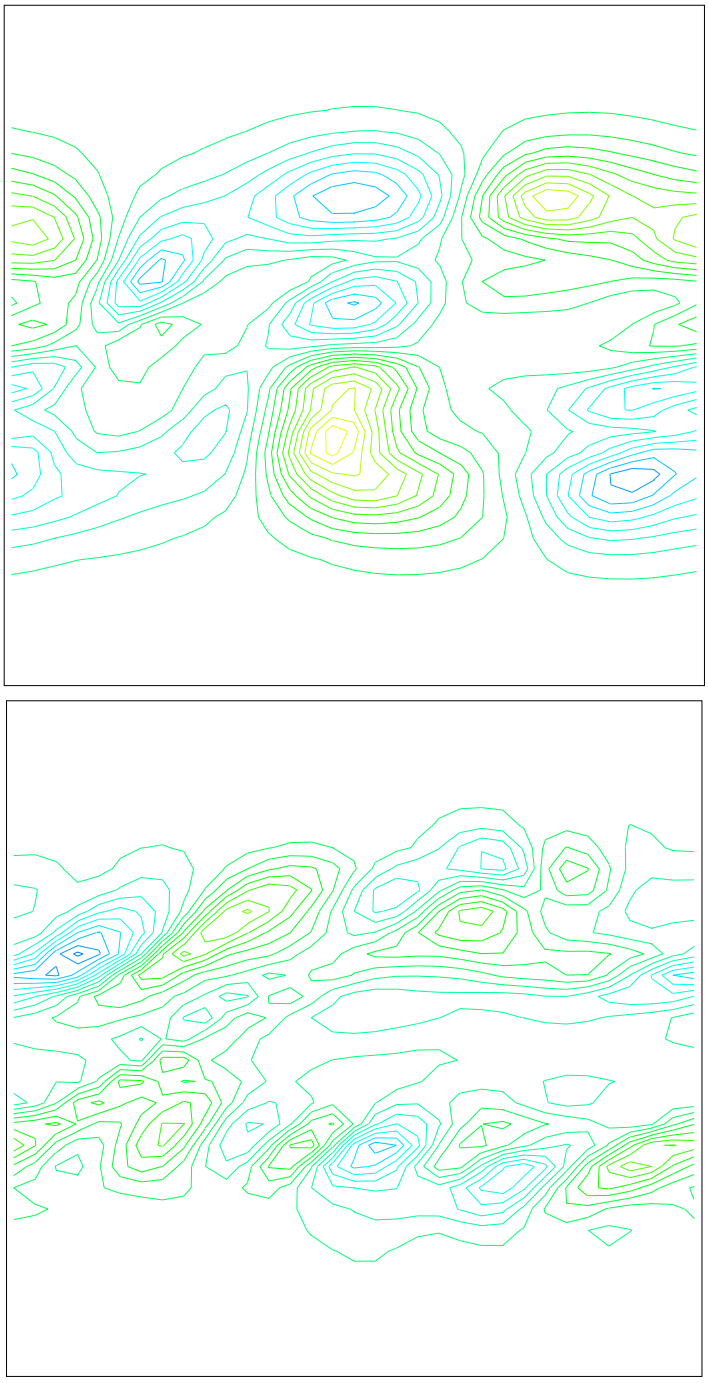

Figure 6.5 Instantaneous value of spanwise component of terms in vorticity equation in mid-span plane (a) Baroclinic Torque (Contour interval level = 0.0018) (b) Expansion term (Contour interval level = 0.0005).

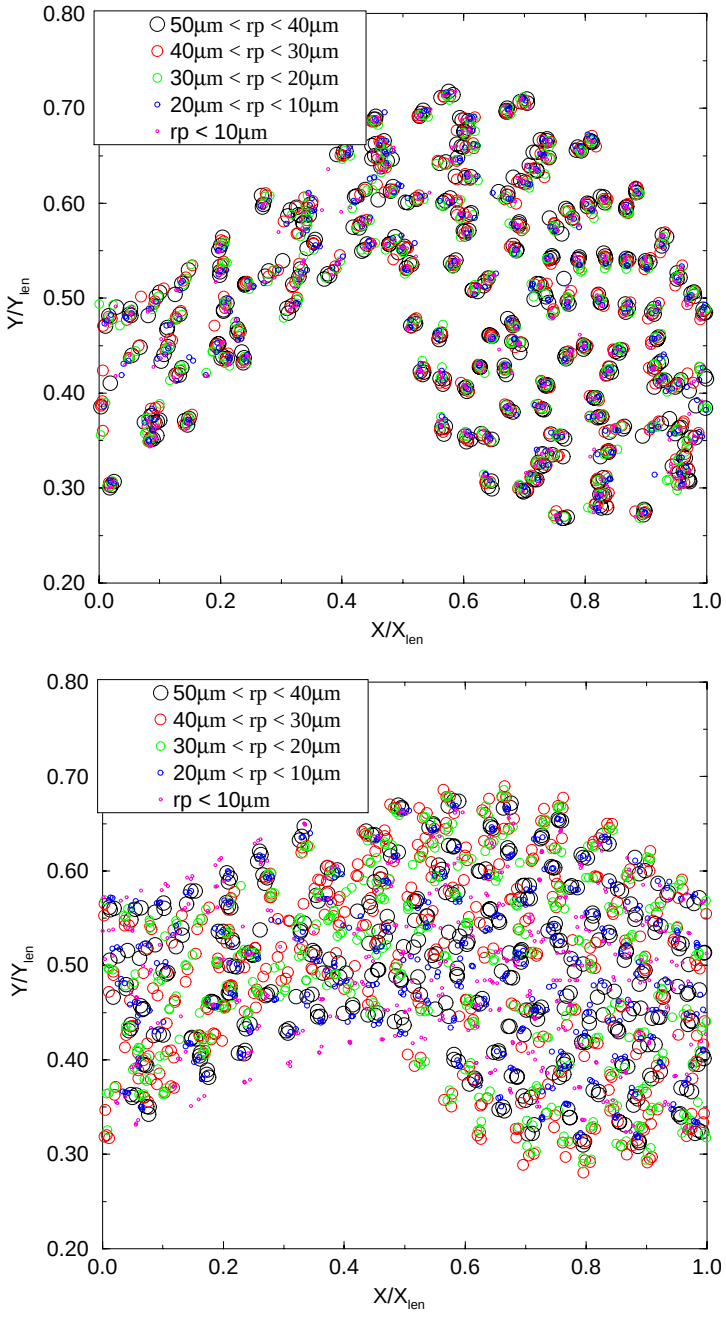

Figure 6.6 Droplet distribution in the X-Y midplane (a) Without coupling and (b) With coupling (LES)

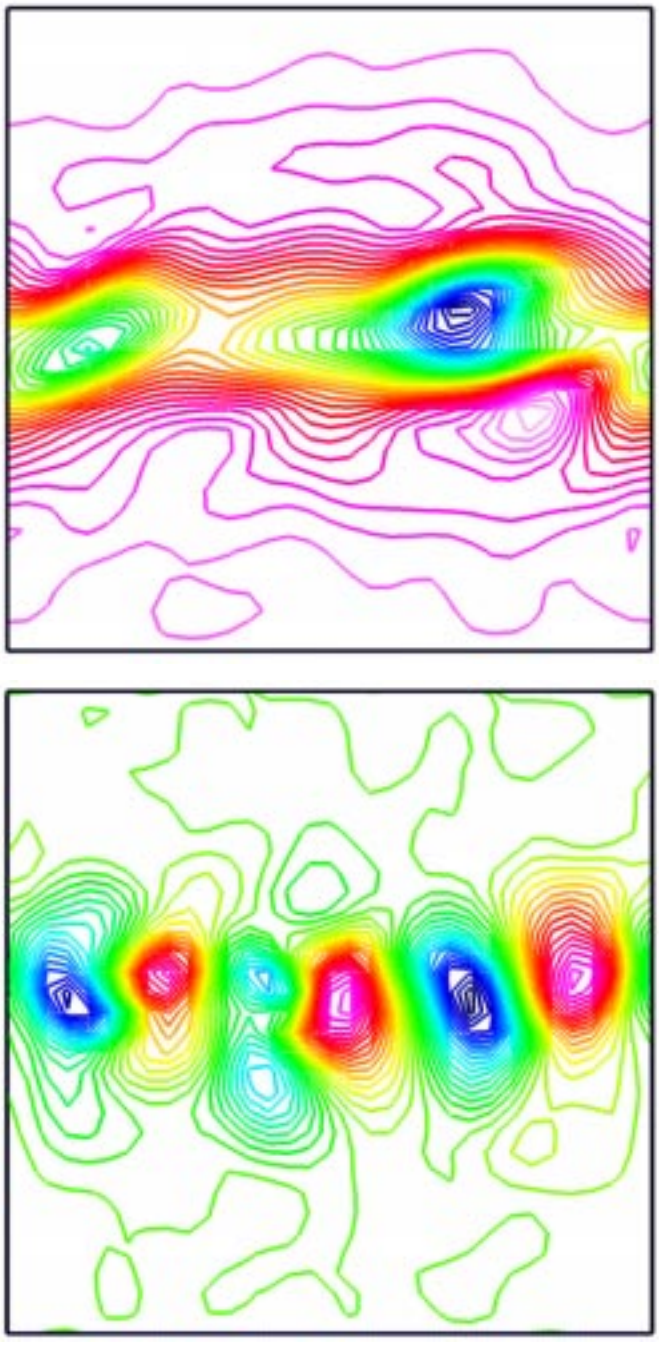

Figure 6.7 Variation across mixing layer using 2-phase LES/LEM methodology (a) Span-wise vorticity (contour interval = 0.0374), (b) Streamwise vorticity (contour interval = 0.03)

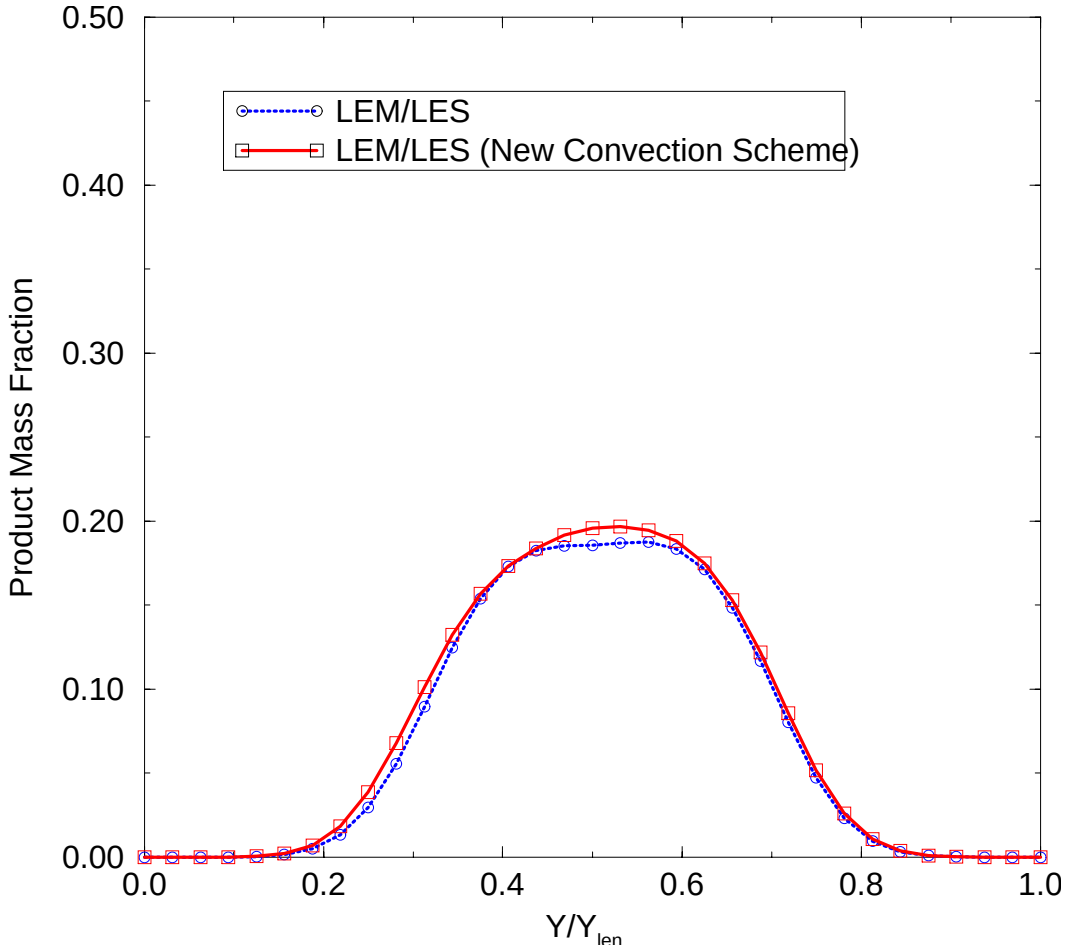

Figure 6.8 Variation of product mass fraction across the mixing layer with new and the old convection algorithms.

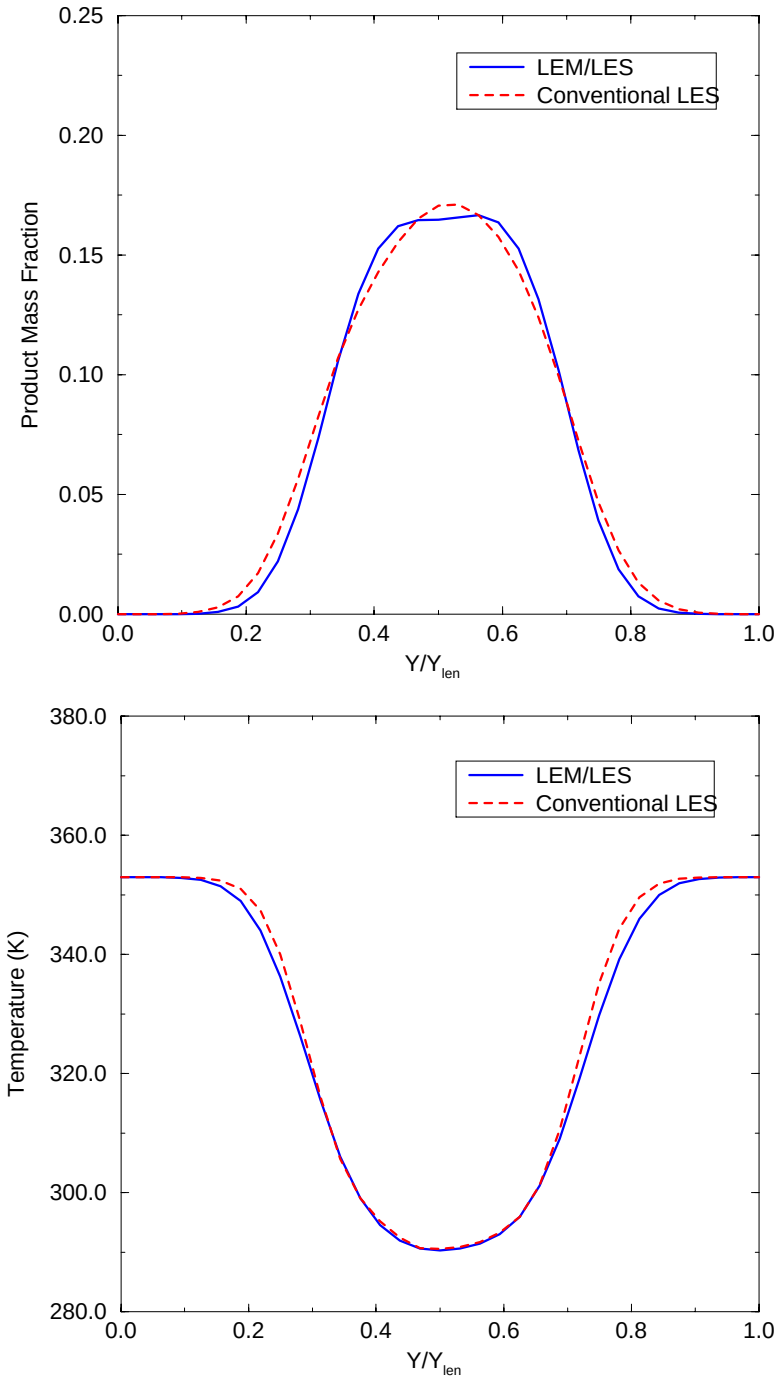

Figure 6.9 Comparison of conventional and current methodology (a) Variation of product mass fraction across the mixing layer and (b) Variation of temperature across the mixing layer.

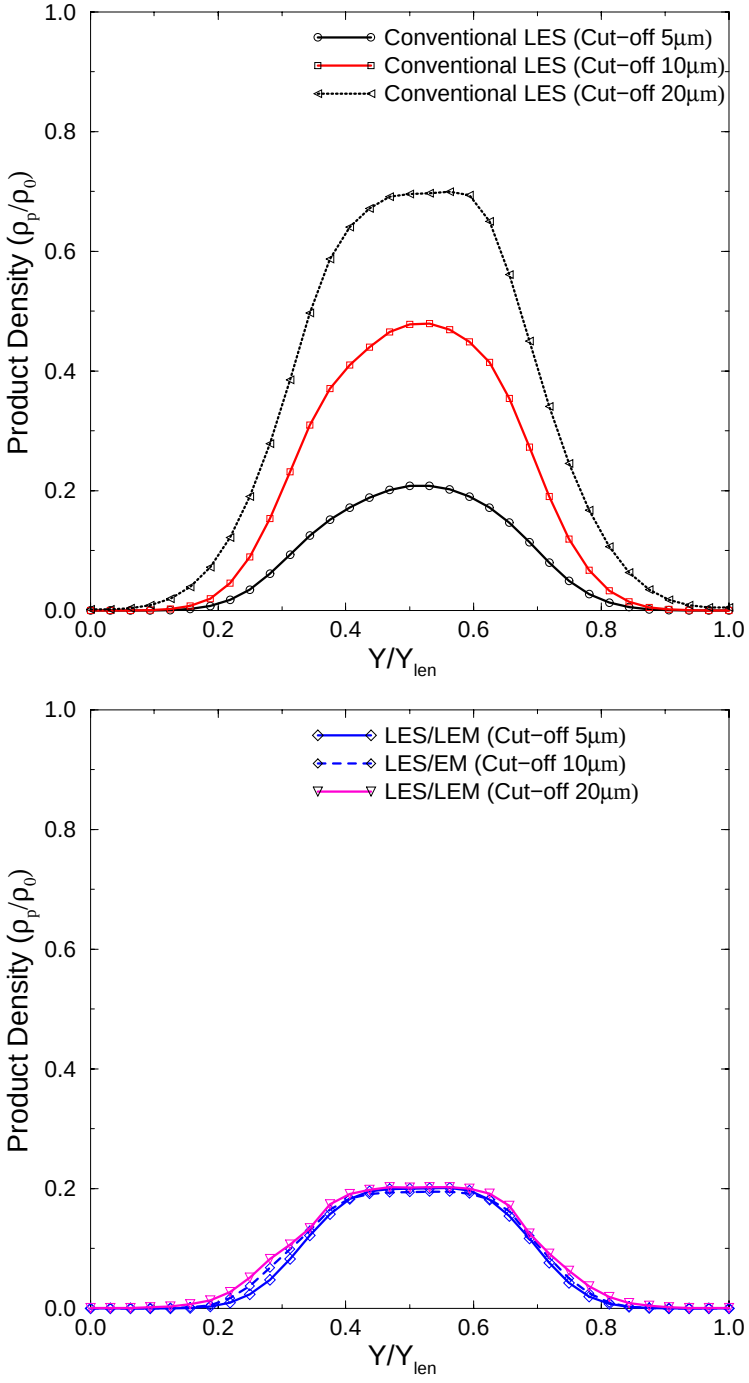

Figure 6.10 Comparison of the two methods in predicting product density (for infinite rate with Damkohler number Da = ∞) across the mixing layer for different cut-offs (a) Conventional LES and (b) LEM/LES.

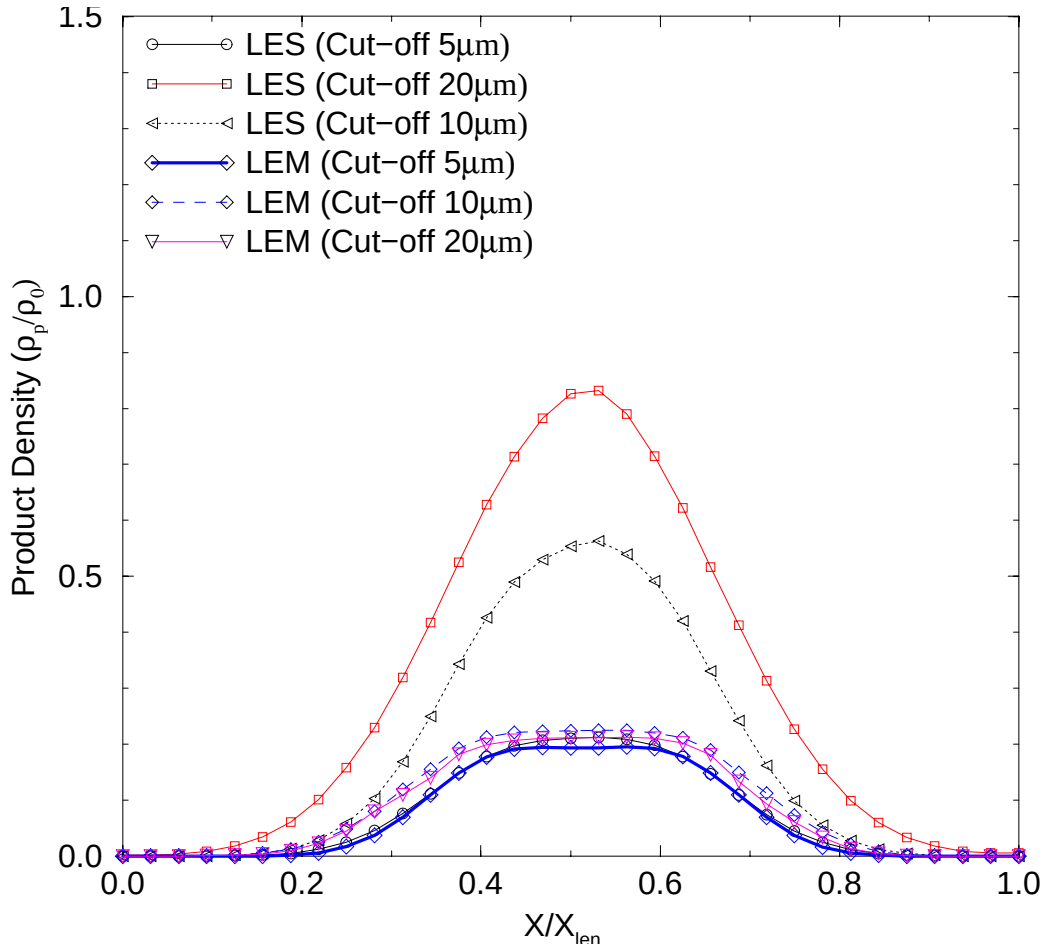

Figure 6.11 Comparison of the LES/LEM and conventional methods in predicting product density (for infinite rate with Damkohler number Da = ∞) across the mixing layer for different cut-offs under higher turbulence and lower forcing.

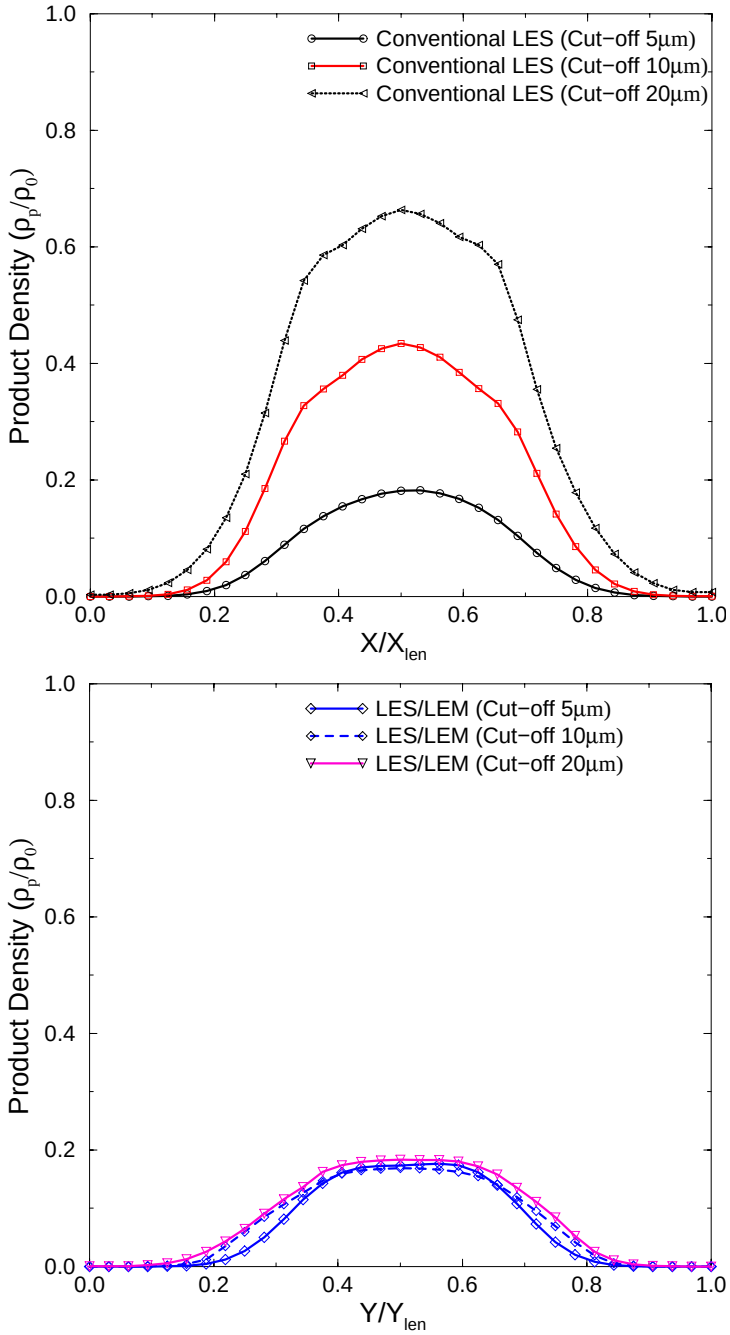

Figure 6.12 Comparison of the two methods in predicting product density (for finite rate with Damkohler number Da = 100) across the mixing layer for different cut-offs (a) Conventional LES and (b) LEM/LES.

CHAPTER VII

SPATIAL SHEAR LAYERS

The mixed Eulerian-Lagrangian approach for two-phase flows as discussed in Chapters 2 & 3 has some significant advantages over the conventional LES approach. However, to fully demonstrate this method, detailed validation against experimental data is important. Unfortunately, controlled experiments where all the required information is available is almost non-existent.

In this chapter, the present LES model has been tested in two experimental spatial shear flow configurations. The first one is a NIST combustor and the second one is a spatial mixing of Hishida *et al.* [46]. This study involves validating the basic LES solver for spatial flows with non-vaporizing and vaporizing droplets. Spatial flows are of interest, since they approximate most of the features of modeling actual combustors.

7.1 NIST Swirling Spray Combustor

In continuation to the validation process, an experimental configuration from National Institute of Standards and Technology (NIST) was chosen to be simulated as it was designed for detailed CFD validation of sprays in highly swirling flows. This

exercise of validating spray simulations against experiments clearly shows that the limitations experienced during experiments cripple one's ability to simulate and validate spray models.

The schematic of the experiment is given in Fig. 7.1. In the experiments, only the secondary air velocities were measured as seeding of the primary air was not possible. With the absence of the fluid velocities in the primary zone, the velocities in the secondary zone were patched in different ways, of which two cases are reported here. The profiles of the axial and radial velocities for these two cases at the inlet are given in Figs. 7.2a and 7.2b. At first, the axial and radial gas-phase velocities were chosen to exactly match the measured droplet velocities at the inlet. The rationale behind the criterion was that the droplets are small enough to be in local equilibrium with the fluid and represent the fluid velocities to reasonable accuracy. Profiles based on such an assumption lead to large recirculation regions at the inflow and do not correspond to anything similar to the downstream evolution of the flow. In an attempt to match the downstream fluid and droplet velocity profiles, the inflow velocities were tweaked from this baseline reference values to arrive at the two cases in Figs. 7.2a and b.

Figs. 7.3a and b show the droplet distributions for the two cases corresponding to the inlet velocities as shown in Figs. 7.2a and b. The distributions clearly indicate that droplet and flow characteristics are extremely sensitive to the assumed profiles of the primary air. Figs. 7.4a, b and c strengthen the same fact, as the downstream velocities and variation of SMD of the droplets are drastically different. It can be concluded that primary air has tremendous influence on the droplet characteristics and since this is a

highly non-linear behavior, determining a proper inflow through reverse engineering is almost impossible. This reiterates the need for detailed experiments with all the required data to be able to successfully validate two-phase codes.

7.2 Spatial Mixing Layers

Extensive study of the temporal mixing layers has been reported in Chapter 6. Temporal mixing layer is a great tool to study and evaluate different physical problems in a simplified manner. The simplicity comes in several different ways. Due to the periodic conditions in the axial direction, the problem of specifying inflow and outflow conditions as well as the appropriate boundary conditions can be avoided. This leads to an ideal situation of having much less resolution in the axial direction. The mathematical problem posed ensures that the centerline of the mixing layer always corresponds to the centerline of the grid, thus ensuring enough resolution at the center of the vortical structures and the mixing layer interface. The simplicity in solving temporal mixing layers comes at an expense and these simulations cannot capture some of the essential features of spatial mixing layers due to the following reasons:

- Spatial mixing layers exhibit asymmetry and mean centerline shifts to the slower stream side.
- Mixing layers are very sensitive to time variation of inflow and outflow conditions. In addition, there is also a strong coupling between the inflow and outflow conditions. To make things worse, previous experiments [74] suggest that there is history effect.

- Spatial and temporal mixing layers correspond to different problems in the presence of heat release and mass addition. Unlike spatial mixing layers, in temporal mixing layers the energy and mass is fed back into the domain through the periodic conditions. This can lead to distortion of the solution.
- Inclusion of effects that control the growth of the mixing layer like splitter plate thickness and boundary layer characteristics into temporal simulations is very difficult.

Considering the above limitations of temporal mixing layers, there is a need to simulate spatial mixing layers in order to have a direct correspondence with experiments. Here, extensive validation of the simulations against the experiments of Hishida *et al.* [46] is carried out. In the available literature, the same problem was numerically simulated using two different approaches. Wang and Squires [56] simulated the problem using LES of temporal mixing layer while Chen and Pereira [75] solved the problem using a time-averaged k-ε formulation. Temporal mixing layers as used in [56] do not mimic the spatial mixing layers for results noted above and result in differences between the experiments and simulations. On the other hand in k-ε formulations, where the equations are obtained by time/ensemble averaging, the prediction of the fluctuating quantities is quite inaccurate since this is essentially an unsteady problem.

The problem in the k-ε simulations is two-fold. First, the model co-efficients have to be tuned to the problem at hand. Second, a complicated stochastic dispersion model has to be used in order to accurately model the particle dispersion characteristics. In the present study, the simulation results have been analyzed and compared with the experiment results and appropriate reference to other mixing layer studies (both

experimental and numerical) are made to draw any similarities or analogies wherever relevant.

Some of the difficulties encountered during the simulations of spatial mixing layers are:

- Sensitivity of the mixing layer characteristics to inflow conditions such as disturbance strength and modes, type of boundary layers on the splitter plates, thickness of the splitter plates etc.
- Several factors (including initial and operating conditions) influence the mixing layer properties as indicated in the experimental results (Bell and Mehta [74] and Oster and Wygnanski [76]). Since these factors can vary from one to another setup, drastically different results were found.
- The above experimental observations translate into numerics such as resolution, grid variation, inflow-outflow conditions, initial conditions, grid stretching, assumed boundary layer shape and thickness, etc.

7.2.1 Spatial mixing layer with particles

In this study, the spatial mixing layer as depicted in Fig. 7.5 was simulated using the zero-mach number incompressible code using a resolution of 197x197x5. Three different particle sizes used in the experiments (Hishida, *et al.*, [46]) were tracked. This problem is essentially 2-dimensional, but the relaxation in the third direction changes the transverse velocities and in turn the axial fluctuations. Since, the spanwise direction is periodic in nature we can assume that it emulates the third direction to some degree. LES also requires the third direction as the turbulence is only correct in the presence of the vortex stretching term. The justification in using 5 points in the spanwise direction is the

fact that the problem is otherwise very expensive to solve. The boundary layer on the 1.17 mm thick splitter plate has to be captured in addition to capturing the entire flow field in the 600 mm long mixing layer. This brings about a wide range of both spatial and temporal scales into the picture, thus restricting the time step. These make the simulations very expensive and takes several days on a 8 processor SGI O2K. The problem is aggravated due to the fact that the current solver is not parallelized for distributed memory architectures and the wall clock times cannot be reduced as the shared memory parallelization does not scale well at higher number of processors. A laminar boundary layer profile was assumed on the splitter plate and the flow is simulated from the end of the splitter plate. Even with this resolution, the splitter plate and the two boundary layers are captured only with 10 grid points. The grid is stretched out slowly in both stream-wise and cross-stream directions. The grid is also skewed (non-cartesian) as the grid has been coarsened at the centerline and appropriately stretched in the cross-stream direction to capture the growing mixing layer more accurately. These impositions further increase the stiffness and thus reduction of the time step.

When the experiments were carried out, the particles were injected at the end of the splitter plate. The present methodology developed works for dilute spray regime only, as particle-particle collisions, etc., have not been incorporated. In addition, sufficient data is not available to specify the particle properties accurately. Therefore, here the particles are injected at a location 100 mm downstream where the evolution of the simulated mixing layer is very close to that of the experiments. The particle velocities were based on the mean and fluctuating quantities, assuming that the fluctuations are Gaussian. The

first three test-cases studied are exactly same as those of the experiments with 42 μm, 72 μm, and 135 μm particle sizes. On an average, around 15,000 to 20,000 particle groups are simulated after the steady-state is reached. In the experiments, it has been observed that the variation of the gas-phase properties in the presence of the particles was less than 3%. The effect of coupling on particle characteristics cannot be evaluated in the experiments, as they cannot have an uncoupled case in reality. To account for the coupling in the experiments, momentum coupling was turned on for the 42 μm case in this study. As expected, it has been found the results with coupling are more closer to the experiments than an uncoupled case.

In Fig. 7.6, the spatial evolution of the momentum thickness is plotted against downstream axial distance. The momentum thickness by definition is:

$$\theta_x = \int_{-\infty}^{+\infty} \frac{u - u_2}{\Delta u} \left\langle 1 - \frac{u - u_2}{\Delta u} \right\rangle dy \tag{7.1}$$

where u_1 is faster stream velocity, u_2 is the slower stream velocity, $u_m = (u_1 + u_2)/2$ is the mean velocity of the mixing layer, Δu is the velocity difference and u is spanwise time-averaged velocity.

The mean velocity was plotted (Fig. 7.7) for four downstream locations and compared to the experiments. Like in the experiments [46], [74], [76] and previous studies [56], there is very good self-similarity in the mean velocities. The fluctuating

quantities $\frac{u_{rms}}{\Delta u}, \frac{v_{rms}}{\Delta u}$ and $\frac{\overline{u'v'}}{\Delta u}$ are plotted in Fig. 7.8 for the first downstream location at 100 mm. There has been reasonably good agreement with the experiments for the first two downstream locations (only the first location is shown here). The increased velocity fluctuations in the tails are due to lower resolution. This is because the rapid changes in the velocities at a coarse grid location amount to increased fluctuations. The downstream development of the mixing layer is lot more stronger than that has been found in the experiments. This is also reflected in the droplet distributions, discussed later in this section. This can be due to a variety of reasons including the following:

- A near 2-D approximation. Earlier studies [77] found that 2-D simulations lead to almost 40% increase in the transverse fluctuating velocities due to the lack of relaxation effect. The periodicity in the spanwise direction has alleviated the relaxation effect to some degree, but the simulation is not entirely 3-D.
- Simulating naturally developing mixing layers (like the one in this experiment) without any dominant modes is extremely difficult as it is not known how to excite the same modes as in the experiments. Due to this difficulty, Wilson and Demuren [77] have used randomly generated fluctuations with a broad spectrum of modes to force the inflow. Schwer *et al.* [78] have done extensive simulations on spatial mixing layers but they have not simulated naturally growing mixing layers citing the difficulties to do the same. This iterates the fact that it is very difficult to validate computational results without precise specification of the inflow conditions.
- Bell and Mehta [74] found that the mixing layer characteristics are highly dependent on the boundary layer characteristics and the wake of the splitter plate. In the present simulations, a laminar boundary layer was chosen based on experimental evidence. The layer used was resolved by few grid points in order to

make the simulation feasible. The coarser resolution could trigger instabilities at different modes which is not the case with the experiments. These modes might be weak to start with, but eventually could lead to additional growth of the shear layer.

- The grid is stretched both in streamwise and cross-stream direction downstream of the splitter plate. This coarsening of the grid and associated numerics could affect the quality of results. In order to address some of these issues, Schwer [79] in his thesis has used extensive sets of complicated grids (in addition to overlap grids) to study the various effects of grid resolutions. Schwer has indicated that the splitter plate has to adequately resolved to capture all the instabilities accurately.

Continuing with the present study, particle properties are plotted in Fig. 7.9 for a particle size of 42 μm. As expected the mean velocities match very well with the experiments. The mean cross-stream velocities tend to differ at the farthest downstream location on the slower stream side. This might be a consequence of the increase in gas-phase transverse fluctuations downstream or the influence of the complex interaction with the slip wall and outflow boundary conditions. The transverse fluctuating velocities and the particle shear stress are captured very well at first two locations. It has been found that the coupled case (solid line) is closer to the experiments (open circles) when compared to uncoupled case (dashed lines). This might be due to the slight dampening of the vortex rollers in the presence of the particles. This may be the same effect observed earlier which is related to mechanism of energy transfer by the particles from the large scales to small scales resulting in the large-scale vortex structures losing energy.

The particle properties corresponding to 72 μm and 135 μm are shown in Figs.

7.10 and 7.11 respectively. The results are very similar to the earlier case. As found in experiments, the particle velocity fluctuations decrease with increasing particle sizes. This is a direct consequence of the inertia of the particles and this is reflected in the mean velocity profiles.

Figure 7.12 shows the droplet distribution for the three different particle sizes. It has been found in the experiments that the Stokes numbers range fall into three categories:

a) 42 μm - Stokes numbers - $0.5 < St < 2.5$

b) 72 μm - Stokes numbers - $2.5 < St < 4.0$

c) 135 μm - Stokes numbers - $St > 4.0$

As observed in the temporal mixing layer simulations, the particles with $St \sim 1$ disperse the most. This can be clearly seen in Fig. 7.12a, where the particles disperse throughout the mixing layer. The initial region downstream of the particle injection is reasonably void of large scale vortical structures. The instabilities become visible further downstream where the fundamental mode dominates resulting in formation of strong vortical structures. Further downstream the growth of the subharmonic mode results in pairing of adjacent vortices. The particles of $St \sim 1$ respond to the centrifugal forces the most manifesting in their concentration in the regions of low vorticity as seen in Fig. 7.12a. For the medium sized particles in Fig. 7.12b where the particle inertia is more dominant, the dispersion of the particles is more contained. In the case of the large droplets (Fig. 7.12c), the particle dispersion is very limited due to relative passiveness caused by the large inertial forces of the particles.

7.2.2 Spatial mixing layers with vaporizing droplets

In this study the spatial mixing layer as depicted in Fig. 7.5 was simulated using the zero-mach number incompressible code using a resolution of 97x97x5. In this case, the 1.17 mm thick splitter plate has been neglected to capture all the features of the mixing layer at this coarser resolution. Five different droplet sizes from 10μm to 50μm were tracked using a Lagrangian Tracking scheme. A laminar boundary layer profile was assumed on the zero-thickness splitter plate and the flow is simulated from the end of the splitter plate. Two different cases are simulated here. One in which all the droplets are carried in the Lagrangian tracking scheme while in the other case all the droplets below cut-off radius of 5 μm are carried in the subgrid with the procedure described in Chapters 3 and 4. In the first case all the scalars are carried in the subgrid and the droplets are tracked in the Lagrangian tracking scheme. Here, the conditions are such that the droplets don't fall below the chosen small cut-off size. In the second case, everything is same except that the cut-off radius was chosen to be 5 μm so that some of the droplets are tracked in the subgrid in the Eulerian fashion.

Figure 7.13 shows the evolution of the mixing layer momentum thickness as defined by Eq. 7.1. This is the equivalent of Fig. 7.6 for the splitter plate of zero-thickness. Here, the growth rate of uncoupled (with passive, non-vaporizing droplets) mixing layer increases at first rapidly than the one with vaporizing droplets. Beyond 70 mm downstream, the growth rate of the coupled mixing layer exceeds that of the uncoupled one. This may be due to transfer of energy from large scales to small scales which results in faster equilibration. It is interesting to note that the growth rate between

the two vaporizing cases is almost identical. This reaffirms that the subgrid treatment of the droplets below the cut-off retains the physics of the problem.

In Figure 7.14, the mean velocity at 200 mm downstream location is plotted for all the three cases. Self-similarity of the mean profiles is achieved in all the cases and is not shown here for clarity. The increased spread of the mixing layer for the vaporizing case can be noted in this figure and is in agreement with Fig. 7.13. The fluctuating quantities are plotted in Fig. 7.15 for all the three cases. Here, similar to earlier figures, there is very good match between the two vaporizing cases. This confirms that the new subgrid treatment of droplets below the cut-off models the mean and fluctuating quantities correctly. As noted in Figs. 7.13 and 7.14, there is increased spread of the mixing layer in the transverse direction. This is reflected in the increased cross-stream fluctuations in Fig. 7.15. The axial fluctuations and the corresponding Reynolds stresses seem to be higher when the droplets are vaporizing. This is related closely to the production of baroclinic torque and reduction of the peak vortex strength in temporal mixing layers discussed in Chapter VI. This is also in agreement with recent studies by Miller and Bellan [37], who have indicated that increasing the droplet mass loading results in a more “natural” turbulence characterized by increased rotational energy (as indicated by instantaneous squared vorticity magnitude averaged over the entire domain) and less influence of the initial forcing parameters.

Calculations using infinite rate kinetics with no heat release, i.e. when the vaporized fuel mixes with the oxidizer and instantaneously reacts, were carried out for the mixing layer with vaporizing droplets. The product mass fraction, which is the ratio

of the product density to the overall gas density, at a location 20 mm downstream of the droplet injection is predicted by the two methods is compared in Fig. 7.16. It can be seen that there is very good agreement between the two methods.

In summary, the current simulations of single and two-phase spatial mixing layers capture most of the salient features. These studies compare very well to the experiments of Hishida *et al.* [46] for mixing layer with and without non-vaporizing particles. The vaporizing case demonstrates the viability of the new subgrid treatment of the droplets below the cut-off as a tool to accurately and efficiently model the two-phase flows. These studies demonstrate the strength of LES of two-phase flows in simulating complex flows with particles and droplets. The simulation methodology as outlined in this thesis can be a great tool to study the two-phase flows with highly non-linear interactions. From the knowledge of the author, this is the first LES simulation of two-phase spatial mixing layer reported in open literature.

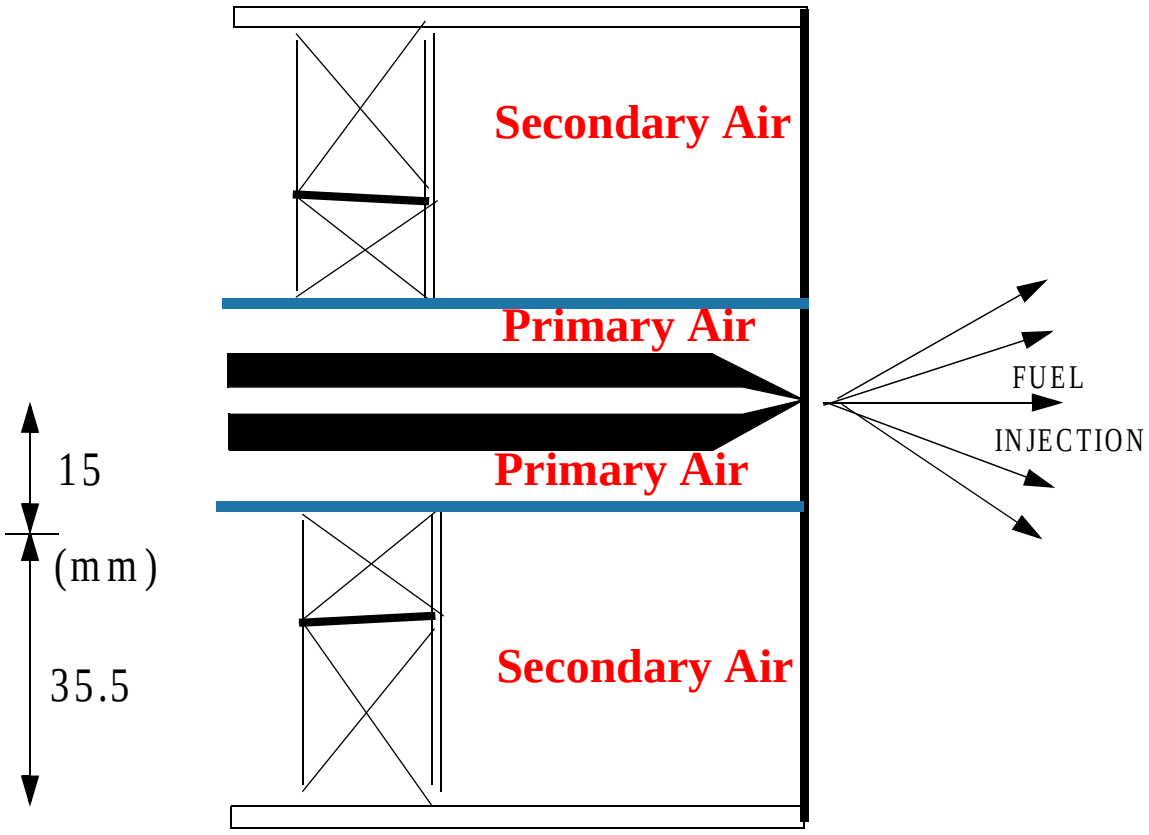

Figure 7.1 Schematic of NIST spray combustor

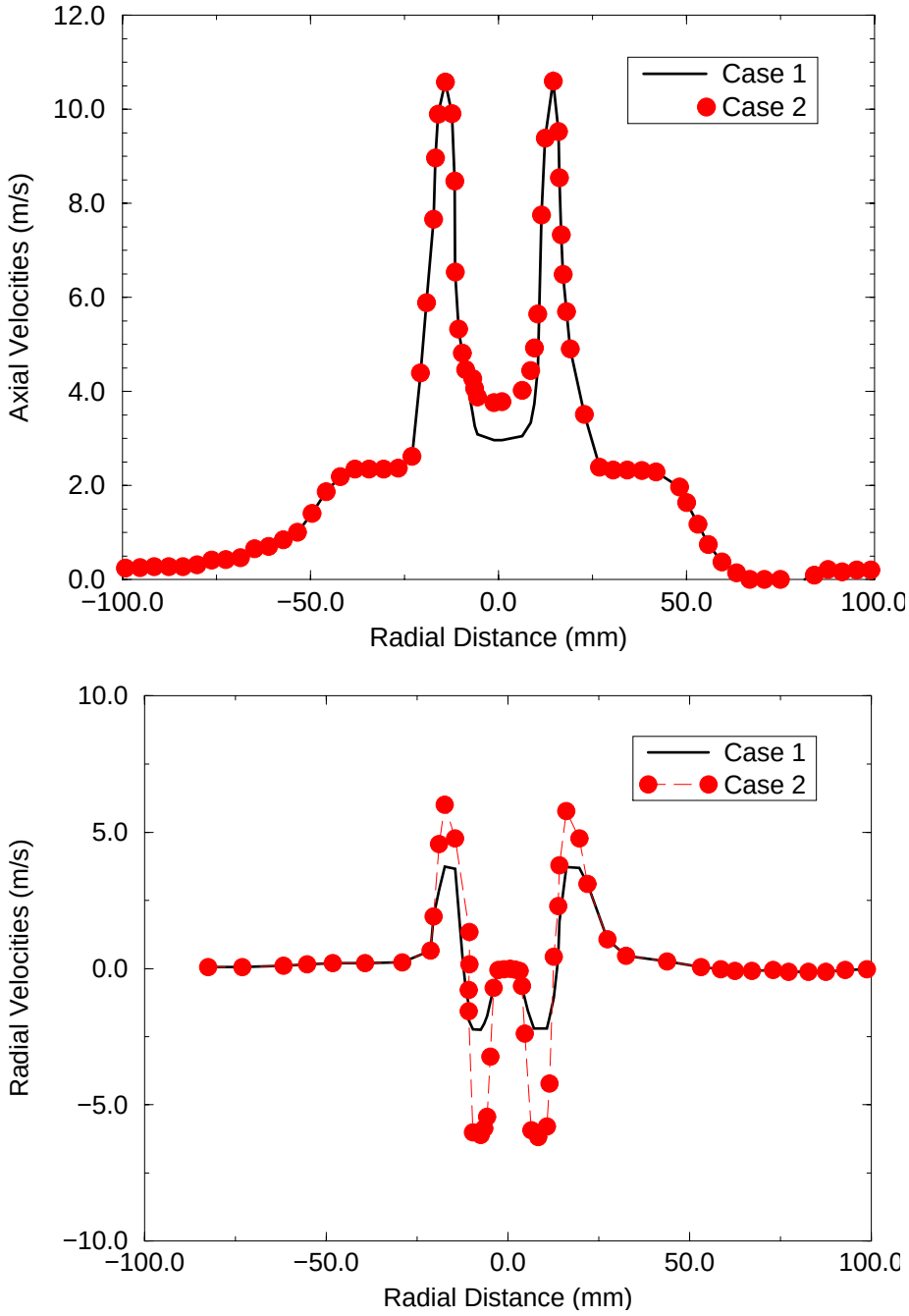

Figure 7.2 Inflow gas-phase profiles for the two cases: a) Axial Velocities and b) Radial Velocities.

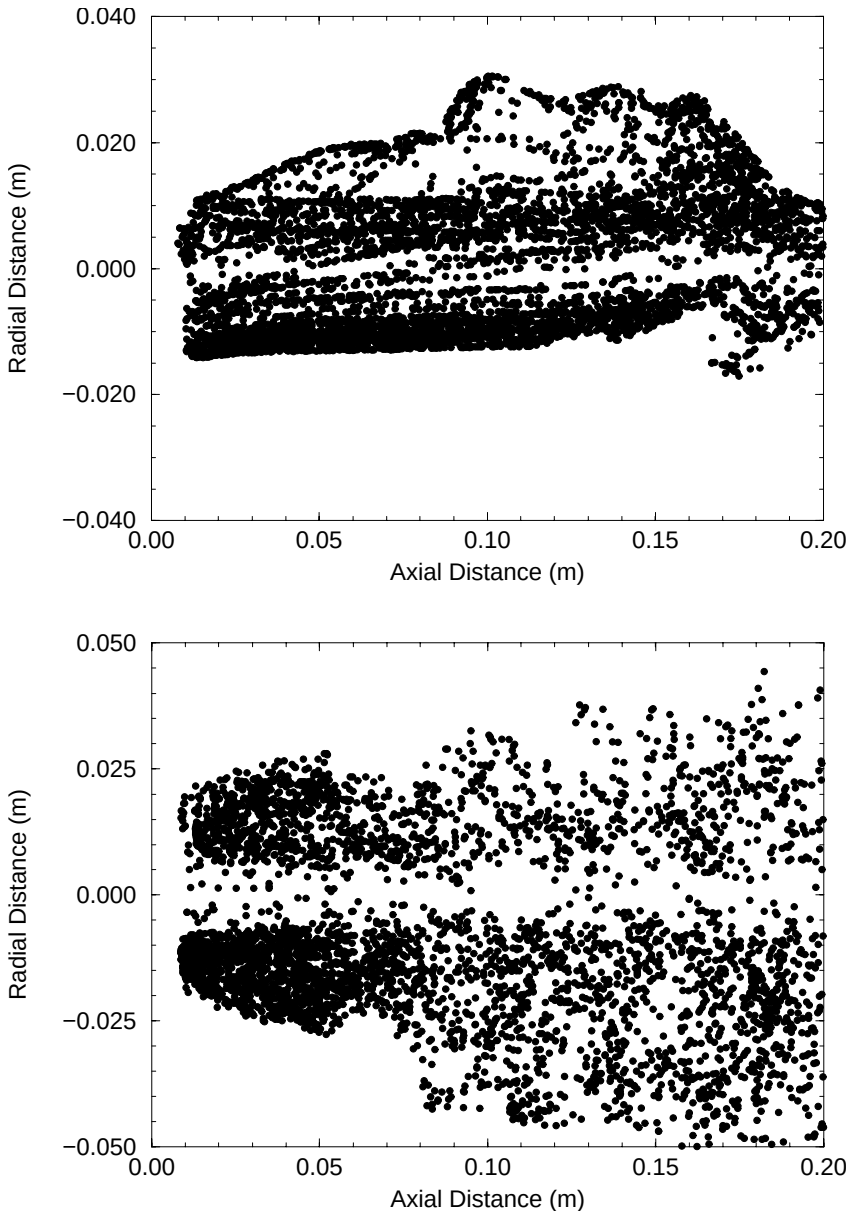

Figure 7.3 Droplet distribution for two different cases in the NIST combustor: a) Case 1 and b) Case 2

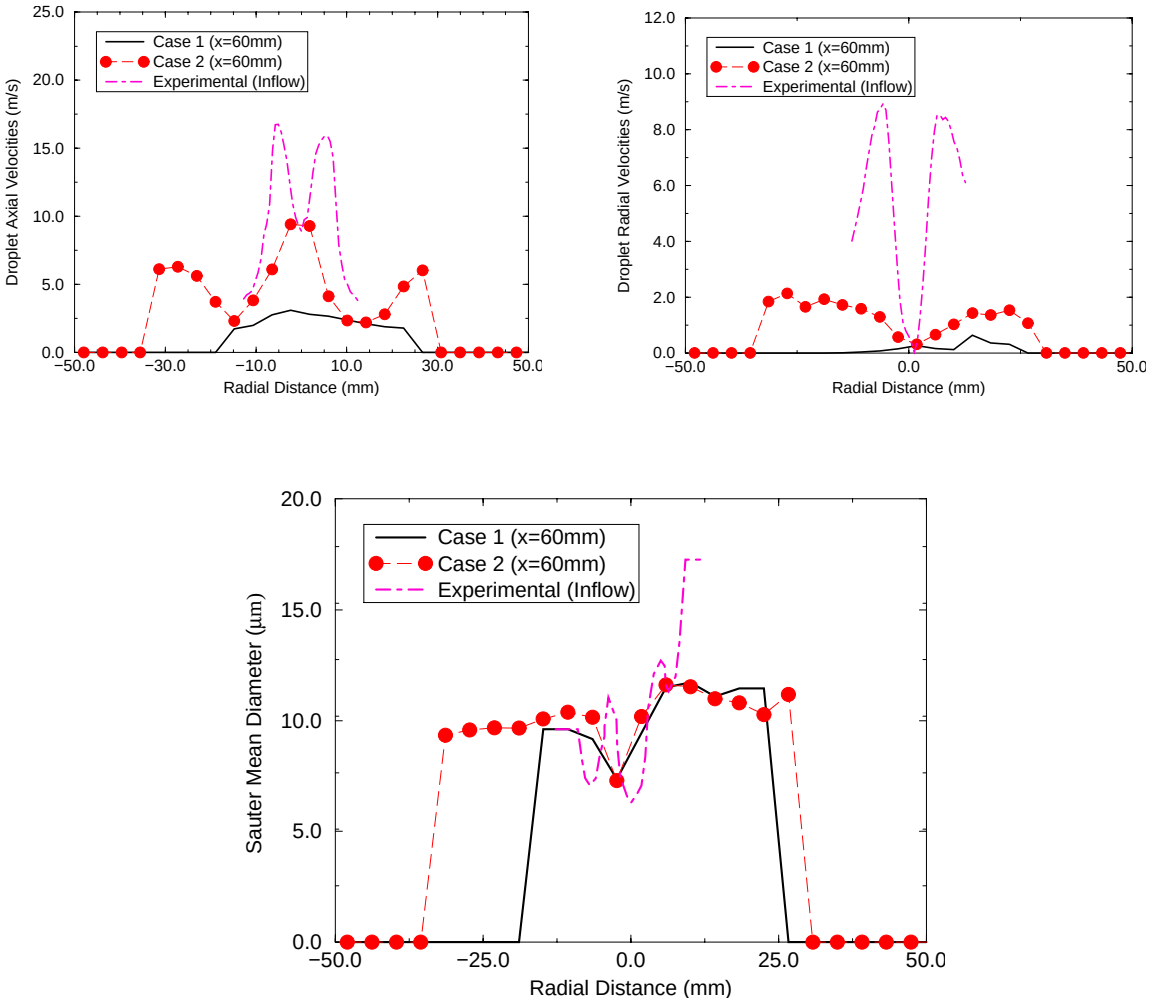

Figure 7.4 Droplet characteristics downstream of the injection for both the cases: a) Radial profile of the droplet axial velocities b) Radial profile of the droplet radial velocities and c) Radial profile of the Sauter mean diameter of the droplets.

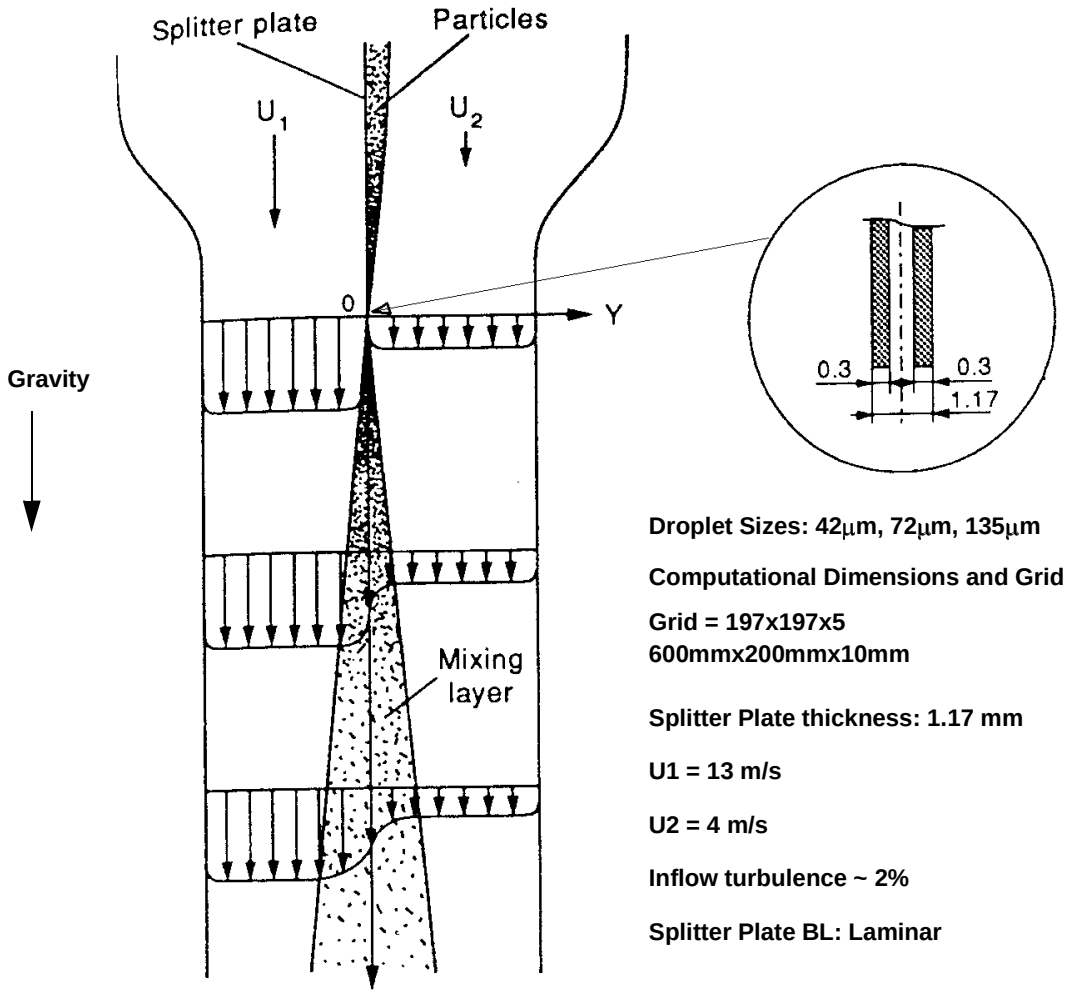

Figure 7.5 Schematic of the Spatial Mixing Layer (from Hishida *et. al.*, [46]) along with the geometric parameters used in the simulations.

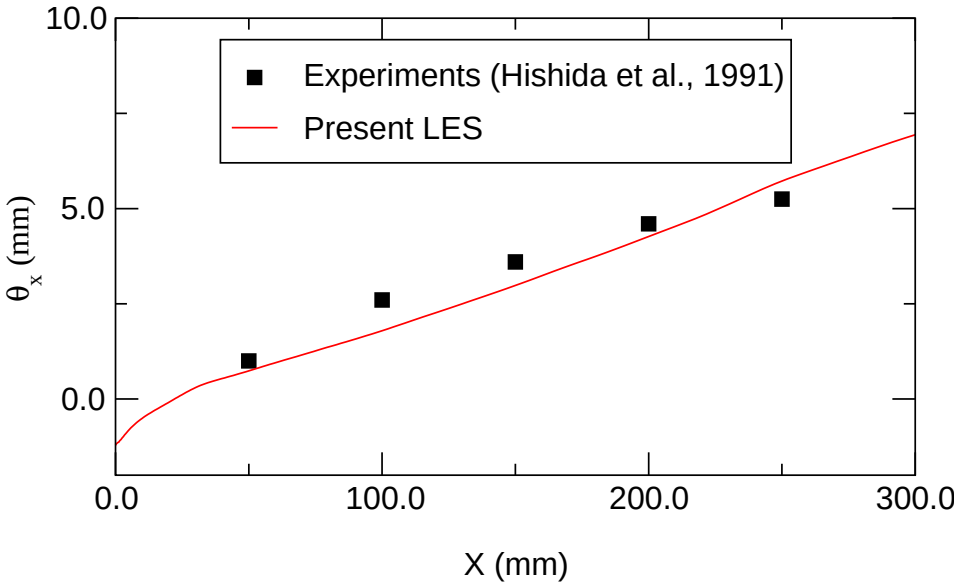

Figure 7.6 Evolution of local momentum thickness with downstream distance.

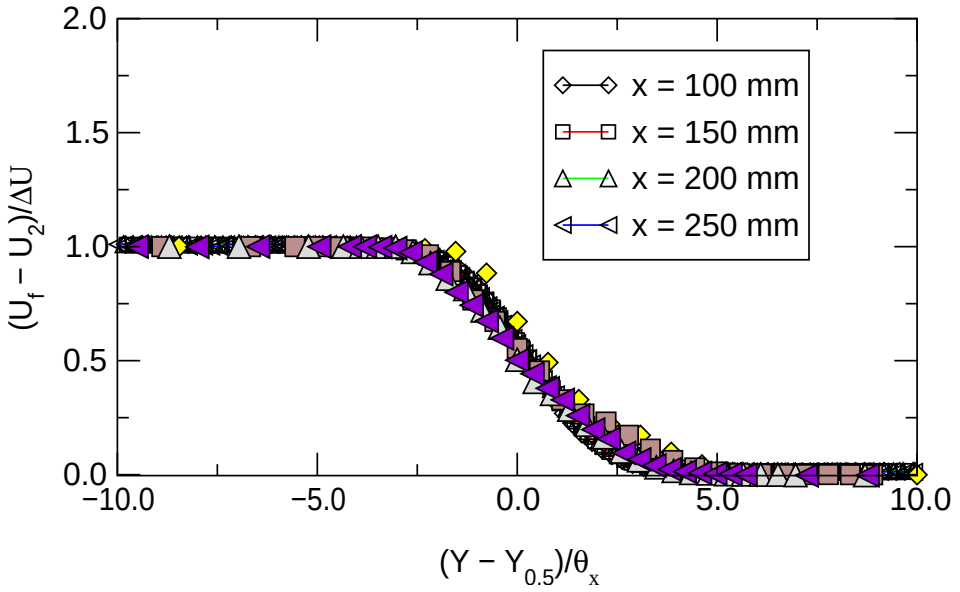

Figure 7.7 Mean axial velocities distribution of the gas-phase flow (lines with empty symbols) compared to the experiments of Hishida *et al.*, [46] (corresponding solid symbols).

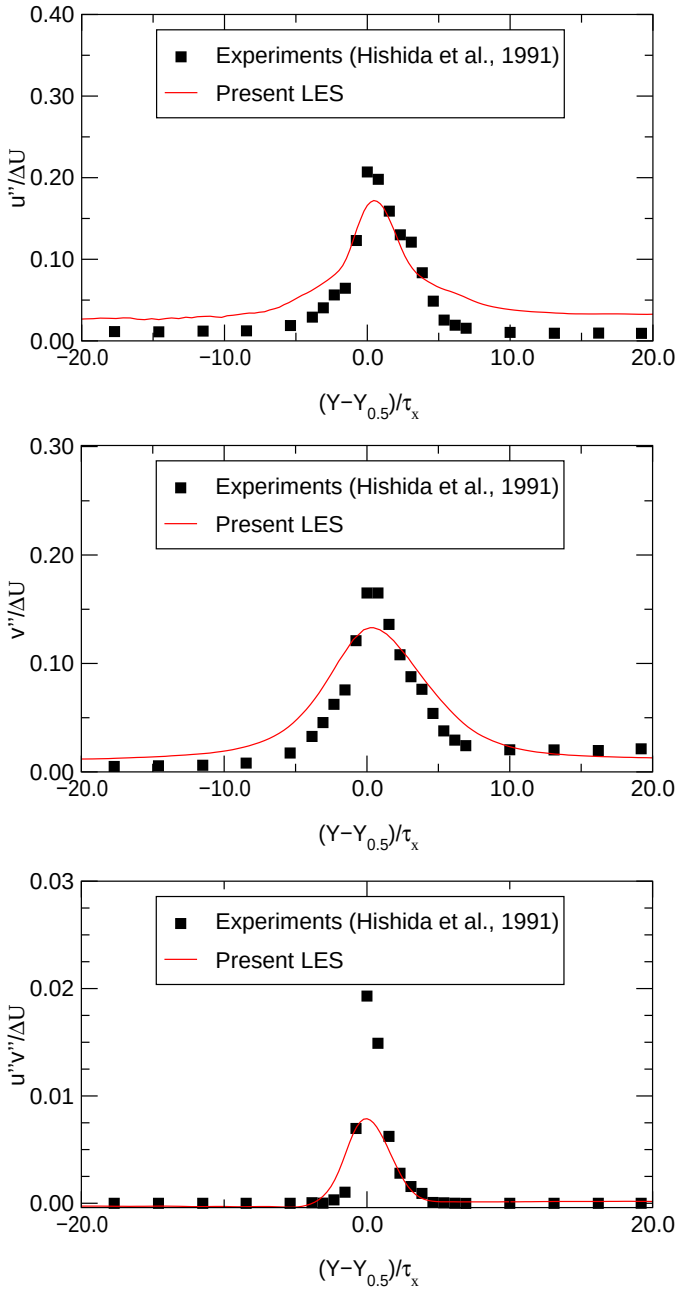

Figure 7.8 Comparisons of the fluctuating quantities with the experiments at 100 mm downstream for the following quantities: a) Normalized streamwise fluctuations, b) Normalized cross-stream fluctuations and c) Reynolds stress.

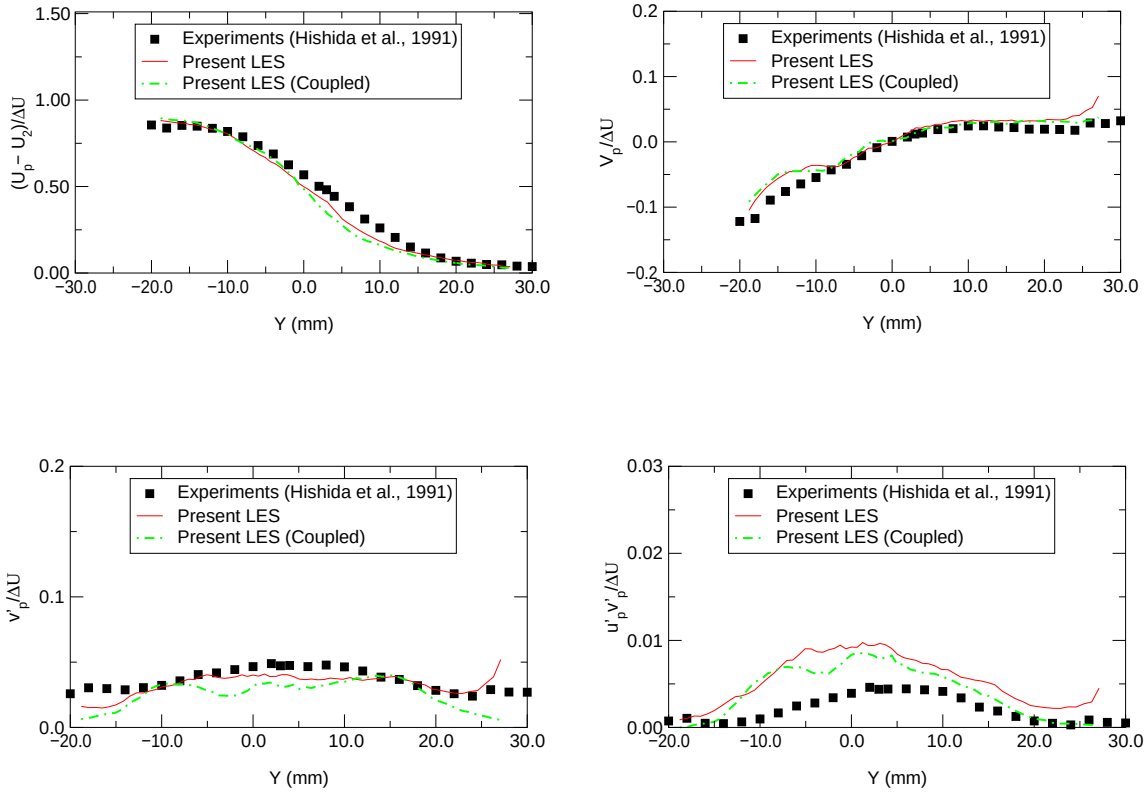

Figure 7.9 Comparisons of the 42 μm particle properties with the experiments at 200 mm downstream for the following: a) Normalized streamwise mean velocities, b) Normalized cross-stream mean velocities, c) Normalized cross-stream fluctuations, and d) Normalized particle shear stress.

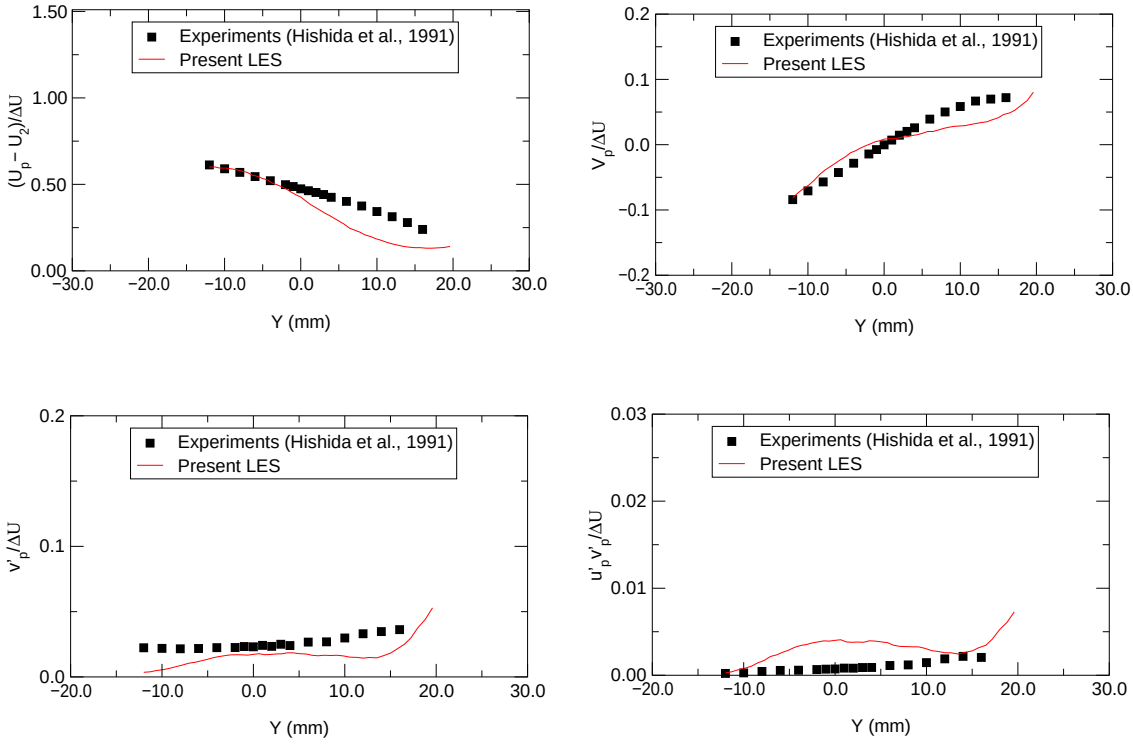

Figure 7.10 Comparisons of the 72 μm particle properties with the experiments at 200 mm downstream for the following: a) Normalized streamwise mean velocities, b) Normalized cross-stream mean velocities, c) Normalized cross-stream fluctuations, and d) Normalized particle shear stress.

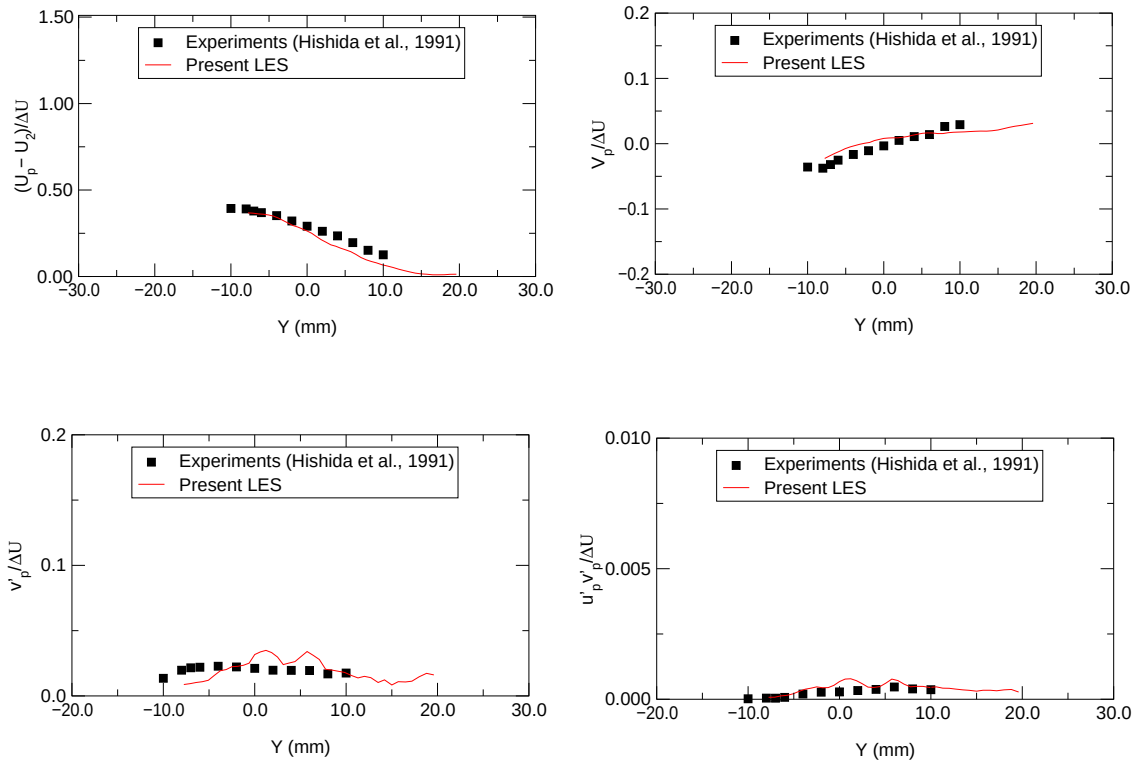

Figure 7.11 Comparisons of the 135 μm particle properties with the experiments at 200 mm downstream for the following: a) Normalized streamwise mean velocities, b) Normalized cross-stream mean velocities, c) Normalized cross-stream fluctuations, and d) Normalized particle shear stress.

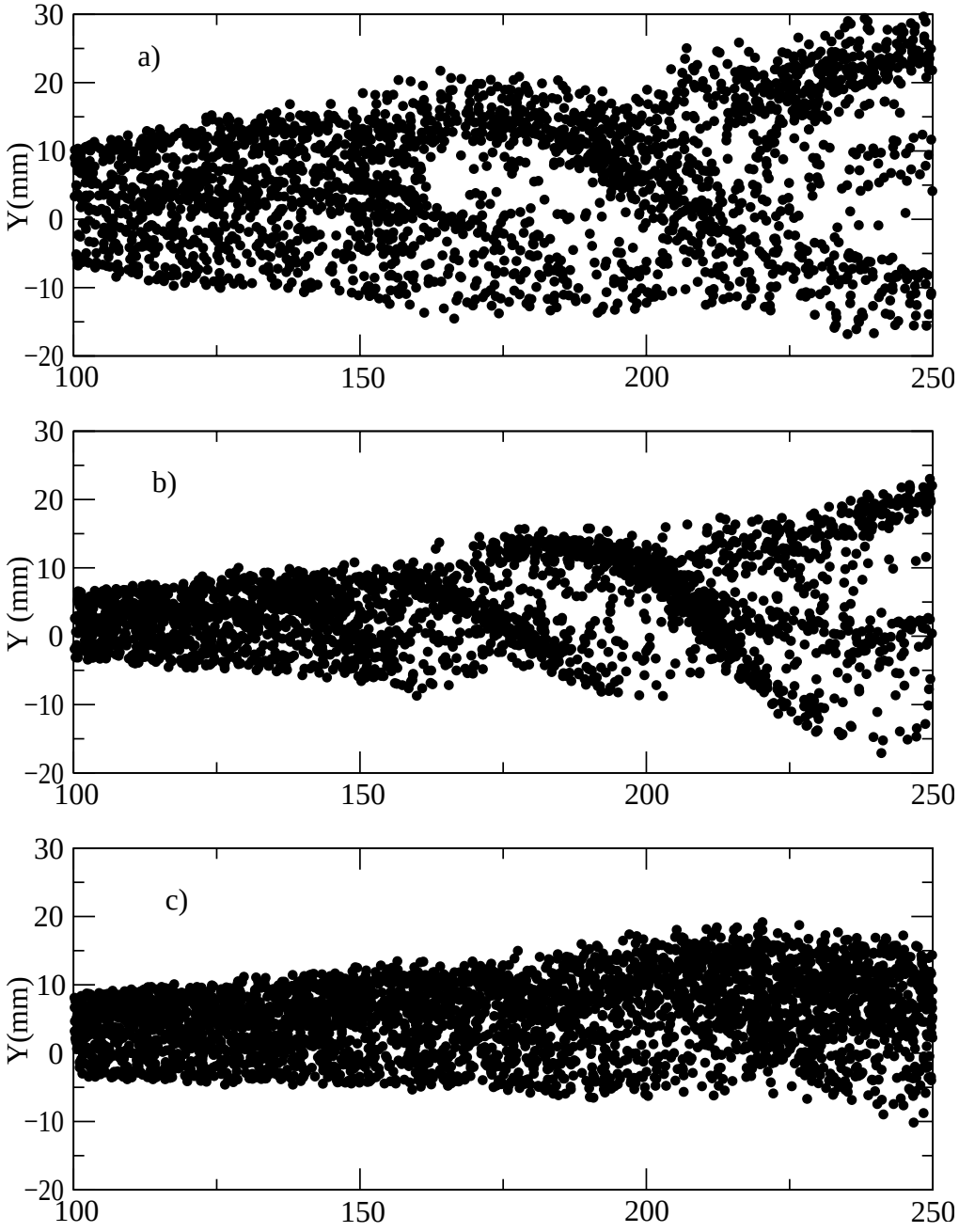

Figure 7.12 Instantaneous droplet distribution for the following particle sizes: a) 42 μm, b) 72 μm and c) 135 μm.

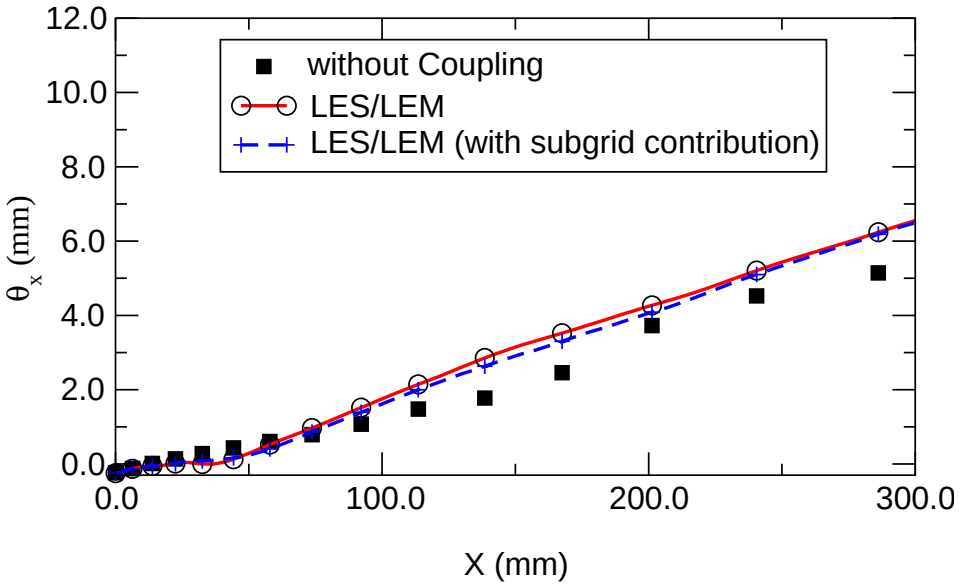

Figure 7.13 Evolution of local momentum thickness with downstream distance with and without vaporization.

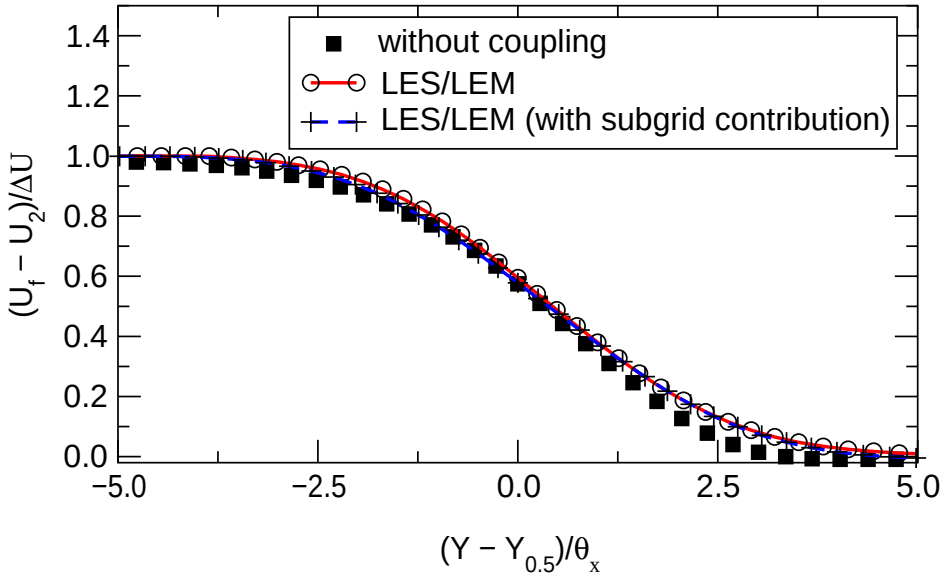

Figure 7.14 Mean axial velocities distribution of the gas-phase flow with and without vaporization.

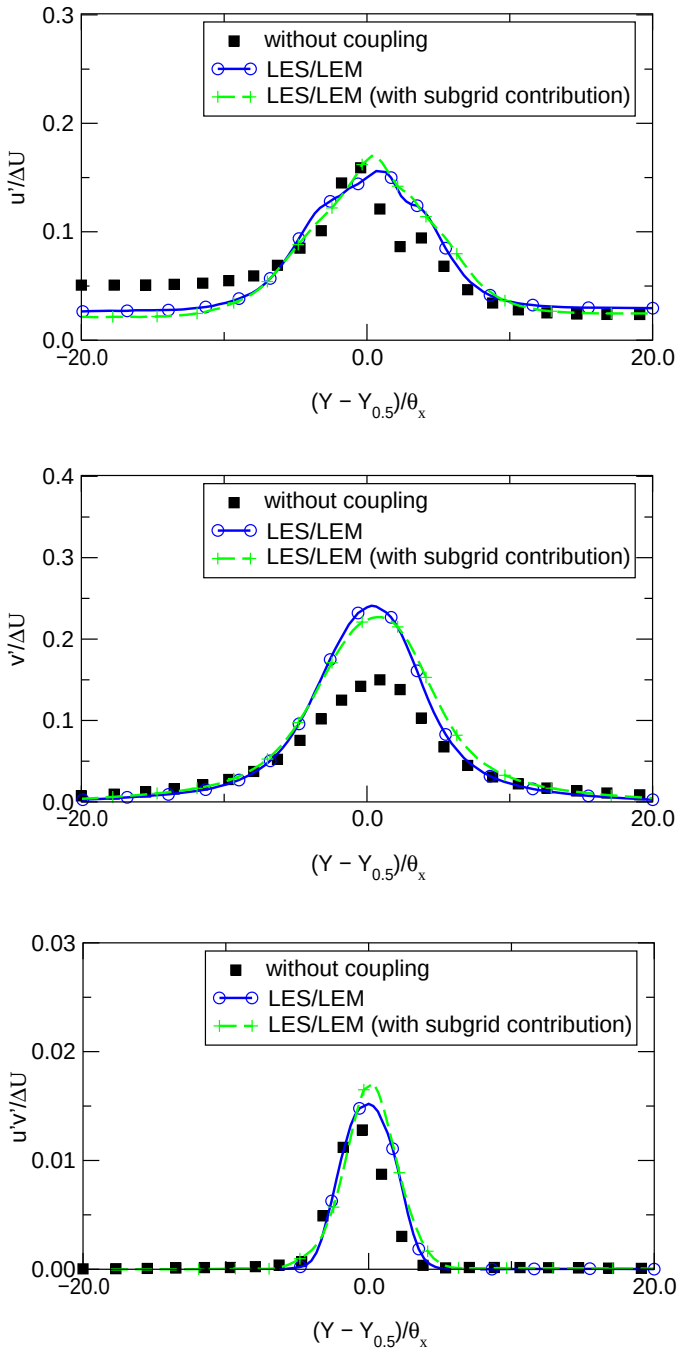

Figure 7.15 Comparisons of the fluctuating quantities with and without vaporization at 200 mm downstream location for the following quantities: a) Normalized streamwise fluctuations, b) Normalized cross-stream fluctuations and c) Reynolds stress.

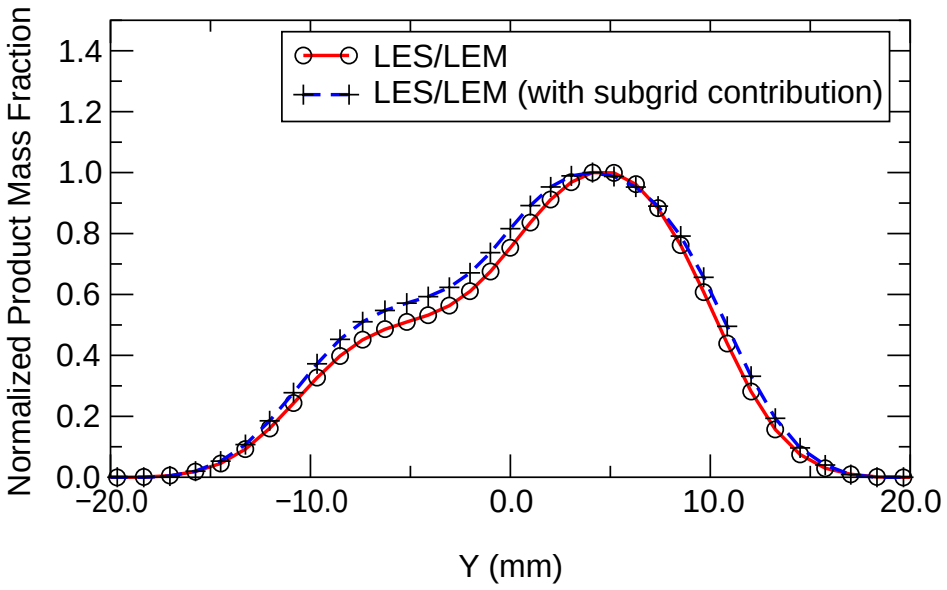

Figure 7.16 Cross-stream variation of normalized product mass fraction for vaporizing droplets with and without subgrid contribution.

CHAPTER VIII

CONCLUSIONS AND RECOMMENDATIONS

8.1 Conclusions

The primary focus of this thesis was on development of models for studying liquid-fuel and air mixing downstream of a fuel injector in a gas turbine, spark-ignition and diesel combustors. This study employed the technique of large eddy simulations as fuel-air mixing is highly unsteady.

The approach outlined in this thesis combines the best features of both Eulerian-Eulerian (gas-liquid) and Eulerian-Lagrangian (gas-liquid) modeling approaches. Gas phase calculations are carried out using an Eulerian LES method, while the liquid droplets are tracked within the Eulerian gas phase using a Lagrangian particle tracking method. The droplet properties are integrated in time in each of the gas phase LES cells and are transported across the Eulerian domain. In this process, the droplets exchange mass, momentum and energy with the local gas phase.

In conventional two-phase modeling, all droplets smaller than a prespecified cut-off size are assumed to instantaneously vaporize and mix. However, results have confirmed that this assumption is highly erroneous unless the cutoff size is very small. Increasing the cutoff size without sacrificing accuracy is of great interest since this would

reduce the computational time significantly. Therefore, in the new model, this issue has been addressed such that the droplets below the cut-off are carried into the subgrid using a void fraction Eulerian formulation. The subgrid model simulates the effect of droplets all the way till the liquid phase completely vaporizes and mixes at the smallest scales using a one-dimensional (1D) domain within each LES cell.

In this thesis, three different problems that constitute the building-blocks of a realistic combustor were addressed. The three problems that have been studied are:

- Two-phase isotropic flows with and without vaporization.
- Two-phase temporal mixing layers.
- Two-phase spatial shear layers.

Two-phase isotropic flows: Simulations of two-phase isotropic flows are carried out using DNS to form a database to compare the LES results. Both DNS and LES (with the closures obtained in this work) results agree very well over the range of parameters chosen in this study. It has been found that the droplets transfer energy from the large scales to the small scales and this process is stronger with increased mass loading of the droplets. The transfer energy spectra also suggests that the energy transfer through gas-phase energy cascade plays less important role in the presence of droplets. The vaporization cases also suggest similar behavior and the transfer of energy is enhanced. Due to periodic conditions the current cases were restricted to very low vaporization rates. The new hybrid subgrid approach could not be evaluated in this set-up because of the low vaporization rates. The computational requirements also limited the study to reasonably low Reynolds numbers compared to practical devices. These studies have to

be re-evaluated at higher Reynolds numbers.

Two-phase temporal mixing layers: Simulations of two-phase temporal mixing layers are carried out in order to study the effects of large-scale motion. These studies corroborate earlier work (both experimental and numerical) that the particles of Stokes number of order one disperse the most. The mixing layers with vaporizing droplets have indicated that the vaporization inhibits the growth of large scale structures. Further analysis of the various terms in the vorticity transport equation suggests that significant baroclinic torque is generated and this curtails the growth of the coherent vortical structures. This phenomena is very similar to the one observed in mixing layer with heat release, though heat is absorbed through the vaporization process. The vaporizing cases also suggest that it is erroneous to assume that droplets below certain cut-off size vaporize instantaneously. It has been found that the method developed in this thesis gives consistently better results as the physical process below the droplet cut-off is explicitly modeled in the two-phase subgrid domain. These studies also indicate that this approach can be computationally more efficient as it avoids tracking the droplets to very small sizes.

Two-phase spatial shear layers: Spatial shear layers are the essential building blocks of all combustors and they are usually more complicated to study with the additional requirement to provide good inflow conditions. This translates to a bigger problem for two-phase flows, as all the information needed for simulations is not generally available from experiments. In addition, treating inflow-outflow boundary conditions accurately is difficult and still an active area of research in computational fluid

dynamics (CFD). Simulations of particles in a NIST combustor are performed and it has been found that crucial primary air gas-phase velocities are missing. The studies indicate that the particle properties have highly non-linear dependence on the gas phase properties and a good set of inflow conditions is needed validate CFD codes. The spatial mixing layer of Hishida *et al.* is simulated and there has been reasonable agreement between the experiments and simulations for both gas phase properties and particle properties. The studies also indicate the need to have more exact specification of the inflow conditions in order to have more deterministic evaluation of LES models. Due to resource constraints, only a few grid points are used in the spanwise direction and there is a need to evaluate the model with higher resolution. The reacting vaporization case suggests that the new LES two-phase model gives consistent results even when the droplets fall below the cut-off.

In summary, a new mixed Eulerian-Lagrangian model for the dispersed phase has been implemented and tested for a wide variety of problems. The new model is computationally more efficient and also less sensitive to changes in droplet cut-off size. The fact, that the dispersed phase transfers kinetic energy from large scales to small scales where it is eventually dissipated is clearly demonstrated. This implies that two-phase models have to explicitly include the effects of dispersed phase on both the large scale and small scale flow features and vice-versa.

8.2 Recommendations

The two-phase flow methodology adopted in this thesis is applicable to dilute spray regime. This is because there are no interactions between the droplets and the droplets are small enough such that secondary break-up is rare. Limitations of this work include the absence of interaction of droplets with the walls and the use of some simplified models governing the heat transfer and vaporization processes in the droplets themselves. Some features that can be included in the spray Lagrangian tracking scheme to extend the scope of applicability are:

- Droplet-droplet collision models: Insight through various experiments using the LES with levelsets for droplet-droplet interactions along with some of the recent work (Chen, *et al.* [80] [81]) can be bundled to incorporate the droplet-droplet collision models. Droplet-droplet break-up and coalescence is also exhibited in the dense spray regions of the spray. Some of the droplet interaction models (e.g. Georjon and Reitz [82]) can be incorporated into the Lagrangian scheme to increase the applicability over a wide range of conditions.
- Droplet-wall interaction models: Inclusion of droplet-wall interaction is of great consequence in automotive and other engines. Some of the simple models (Mundo, *et al*. [83]) can be easily implemented in current LES formulation.
- Particle dispersion models: This thesis uses a simple stochastic model (Faeth [28]) to calculate the instantaneous velocity from the averaged and subgrid fields available from the gas-phase LES solution. Considerable progress has been made in the

so-called eddy-interaction models (Shirlokar, *et al*. [84]) and some of those models can be implemented and evaluated in LES. Since the subgrid fields are more accurate in LES, considerable improvements can be captured in terms of particle/droplet dispersion characteristics.

- Charged particle interaction: Fast-multipole or field approximation theories can be incorporated to study and analyze the behavior of charged injectors and other applications involving the charge interactions.
- Circulation: Most of the droplets in practical systems are multicomponent with vaporization. Additional models based on the previous research (Tong and Sirignano [85]; Bellan and Harstad [86]) need to be incorporated into the Lagrangian tracking scheme to model the chemical reactions and circulation.

The work carried out in this thesis is currently limited to chemical reactions with no heat release. The work has to be extended and evaluated under heat release. In the presence of heat release, it is expected to have very tight and more non-linear coupling between the two-phases. The vaporization of the liquid fuel is going to produce fuel in gas phase, which is going to react and release heat. This, in turn will vaporize more fuel. The vaporization process will absorb part of the heat released during the chemical process and affect the reaction rates. Both the vaporization and chemical reactions are going to interact closely in modifying the characteristics of the two phases.

The eventual goal of two-phase flow modeling is the ability to simulate the physical processes all the way from the injector into the combustion chamber and into the exhaust in a very closely coupled fashion. Based on the work in this thesis and with

inclusion of the suggested extensions, a plausible approach is outlined here which can provide a framework to model liquid-fuel combustors. Some of the simulation and implementation issues pertaining to the same are discussed below, using a diesel engine as a sample problem.

Figure 8.1, illustrates the various modeling regimes of a typical diesel engine. Some details of the physical problem at hand along with the modeling requirements and plausible approaches are given in this schematic.

The two-phase LES framework described in this thesis along with the extensions suggested earlier can be adapted to model the fuel injector and spray formation (both charged and non-charged) as a design tool for the next generation of high efficiency engines with low emissions. LES on unstructured/adaptive grids with level-sets is a viable approach to model the fuel injector and spray formation. The accurate interface tracking capabilities of level sets, along with accurate fluid flow computations using LES, makes the solution very feasible. These computations coupled with the Lagrangian tracking capability can be used to study downstream evolution of spray, both in charged and uncharged cases.

The fuel injector modeling effort provides initial conditions to model the downstream spray combustion process. The hybrid Eulerian-Lagrangian LES methodology developed in this work can be adapted to simulate the physical processes such as fuel-air mixing, vaporization and phase-change downstream in the combustor.

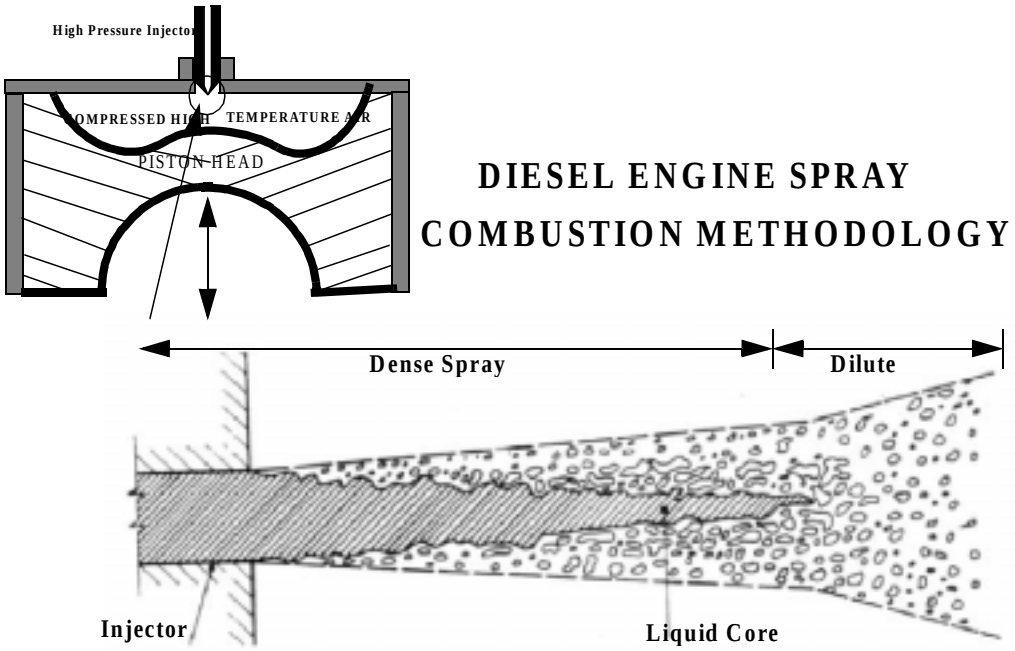

Inside and Near Injector Modeling	Dense Spray Regime	Dilute Spray Combustion Regime
•Liquid Core •Droplet Formation •Shear between the liquid and ambient air	•Liquid Core and large droplets near the center line •Dilute regime away from the centerline •Droplet interaction very prominent	•Droplet break-up and interaction very limited •The spray is very dilute (void fractions of the dispersed phase < 0.01) •Vaporization, Mixing, Combustion in highly swirling flow
•LES on adaptive, unstructured grids with level sets to track the fluid-liquid interface •The output is supplied to the next regime modeling	•Use Eulerian approach for the dispersed phase in the dense regions •Use Lagrangian approach for small droplets •The gas-phase is solved using LES which accurately depicts for the flow characteristics	•Use Lagrangian tracking for medium sized droplets •Smaller droplets go into the subgrid in an Eulerian form as void fraction •Turbulence and scalar mixing are captured by LES •Further droplet break-up and collisions are modeled by simple models

Figure 8.1 Modeling regimes in a diesel engine

APPENDIX A

ZERO-MACH NUMBER EQUATIONS

Zero Mach number approximation of the Navier Stokes equations

The equations governing the flow of a reacting perfect gas are reduced to the following non-dimensional form:

$$\frac{\partial \rho}{\partial t} + \frac{\partial}{\partial x_j}(\rho u_j) = 0 \tag{A.1}$$

$$\gamma M^2 \rho \frac{Du_i}{Dt} = -\frac{\partial p}{\partial x_i} + \frac{\gamma M^2}{Re}\frac{\partial}{\partial x_j}(\tau_{ij}) \tag{A.2}$$

$$\rho \frac{DE}{Dt} = -\frac{\partial}{\partial x_i}(\gamma - 1)(pu_i) + \frac{(\gamma - 1)\gamma M^2}{Re}\frac{\partial}{\partial x_j}(\tau_{ij} u_i) - \frac{1}{PrRe}\frac{\partial q_i}{\partial x_i} + CeQ \tag{A.3}$$

$$\frac{\partial C_\alpha}{\partial t} + \frac{\partial}{\partial x_j}(C_\alpha u_j) = DaR_\alpha + \frac{1}{Pe}\frac{\partial^2 C_\alpha}{\partial x_j^2} \tag{A.4}$$

$$p = \rho T \tag{A.5}$$

In the above equation set, $Re(=\rho_0 U_0 L_0/\mu)$, $Pr(=\mu C_p/\kappa)$, $Da(=L_0 R_\alpha/U_0)$, $Pe(=\rho_0 U_0 L_0/D_\alpha)$, $M(=U_0/\sqrt{\gamma R T_0})$ are, respectively, the Reynolds number, Prandtl number, Damkohler number, the Peclet number and the flow Mach number corresponding to the reference quantities. Note that all the material properties such as the various diffusivities (corresponding to momentum, mass and energy) and γ are assumed to be constant in obtaining the above equation set. These assumptions constitute a mere convenience and are not absolutely necessary. $Ce=Q_0 L_0/(U_0 C_v T_0 \rho_0)$ is the non-dimensional number quantifying the effects of heat release against the effects of convection on the energy transport.

The parameter γM^2 quantifies the effects of compressibility on the flow field. This can be shown by considering the limiting case when $\gamma M^2 \to 0$. In this limit, by definition (of M), the acoustic speed is infinite and the fluid velocity is finite. The acoustic speed is obtained as the rate of change of thermodynamic pressure with respect to density variations at constant entropy $a = \partial p/\partial \rho|_s$. If this quantity is infinite, one would need infinite thermodynamic pressure change to compress the fluid (i.e. change it's density).

A perturbation technique is adopted for the current purpose using the parameter γM^2. Each of the dependent flow variables is expanded as a power series of this parameter. For e.g., $\rho = \rho^{(0)} + \gamma M^2 \rho^{(1)} + \gamma^2 M^4 \rho^{(2)} + ...$. On substitution of these expansions into Eqs. A.1-A.5, and using perturbation analysis, solutions that satisfy the

governing equations up to any required order of γM^2 can be obtained.

The transport equations for continuity, momentum, chemical concentration(s) and equation of state, to the zeroth order (incompressible) approximation, reduce to the following set of equations.

$$\frac{\partial \rho}{\partial t} + \frac{\partial}{\partial x_j}(\rho u_j) = 0 \tag{A.6}$$

$$\frac{\partial p^{(0)}}{\partial x_k} = 0 \tag{A.7}$$

$$\frac{\partial C_\alpha}{\partial t} + \frac{\partial}{\partial x_j}(C_\alpha u_j) = DaR_\alpha + \frac{1}{Pe}\frac{\partial^2 C_\alpha}{\partial x_j^2} \tag{A.8}$$

$$p^{(0)} = \rho T \tag{A.9}$$

The superscripts corresponding to zeroth order terms of all variables except pressure are dropped for convenience. The reason for the exception of pressure variable is made clear in the arguments that follow.

It is seen (from Eq. A.7) that the zeroth order approximation of the momentum equation has reduced to a gradient free condition for zeroth order pressure. At the zeroth

order approximation of the governing equations, there is no equation for the velocity variables. In order to obtain an equation for the velocity field, (at least) the first order approximation of the momentum equation A.2 is needed. Such an approximation yields the following equation for leading order velocity field.

$$\rho \frac{Du_i}{Dt} = -\frac{\partial p^{(1)}}{\partial x_i} + \frac{1}{Re}\frac{\partial}{\partial x_j}(\tau_{ij}) \tag{A.10}$$

As seen in the above equation, the first order pressure is required in order to obtain the leading order velocity field. The leading order approximation to the continuity equation A.6 can be used to express the leading order approximation to the energy equation as follows.

$$\frac{\partial u_i}{\partial x_i} = \frac{1}{\gamma p^{(0)}}\left[\frac{\gamma}{PrRe}\frac{\partial q_k}{\partial x_k} - \frac{\partial p^{(0)}}{\partial t} + CeQ\right] \tag{A.11}$$

The heat release Q is a function of the reaction rate(s) R_α and is determined by the chemical kinetic mechanism used for reaction rate modeling. The six equations (A.6-A.11) form a closed system of equations for the leading order approximations of the six variables, ρ, $p^{(0)}$, C_α, T, u_i and $p^{(1)}$. For simplicity, p_0 is used $p^{(0)}$ and p is used for $p^{(1)}$.

Energy Equation for Two-Phase Flows in the Zero-Mach Number Limit

The energy equation in terms of the total internal energy is of the following form:

$$\frac{\partial}{\partial t}(\rho e_t) + \frac{\partial}{\partial x_i}(\rho e_t u_i) = -\frac{\partial q_i}{\partial x_i} + \dot{Q} + \frac{\partial}{\partial x_i}(\sigma_{ji} u_i) + \rho \sum_{k=1}^{N} Y_k f_{k,i}(u_i + V_{k,i}) + \dot{Q}_s \qquad \text{(A.12)}$$

Neglecting work due to body forces, dropping terms due to chemical heat release and expanding LHS Eq. A.12 reduces to:

$$\rho \frac{\partial e_t}{\partial t} + e_t \frac{\partial \rho}{\partial t} + e_t \frac{\partial}{\partial t}(\rho u_i) + \rho u_i \frac{\partial e_t}{\partial x_i} = -\frac{\partial q_i}{\partial x_i} + \frac{\partial}{\partial x_i}(\sigma_{ji} u_i) + \dot{Q}_s \qquad \text{(A.13)}$$

Invoking the continuity equation (Eq. 2.1):

$$\rho \frac{\partial e_t}{\partial t} + e_t \dot{\rho}_s + \rho u_i \frac{\partial e_t}{\partial x_i} = -\frac{\partial q_i}{\partial x_i} + \frac{\partial}{\partial x_i}(\sigma_{ji} u_i) + \dot{Q}_s \qquad \text{(A.14)}$$

Multiplying the momentum equation (Eq. 2.2) by u_i we have

$$\rho u_i \frac{\partial u_i}{\partial t} + \rho u_j u_i \frac{\partial u_i}{\partial x_j} = u_i \frac{\partial}{\partial x_j}(\sigma_{ji}) + u_i \dot{F}_{s,\,i} \tag{A.15}$$

Subtracting Eq. A.15 from Eq. A.13 we get,

$$\rho \frac{De}{Dt} + \dot{\rho}_s e_t = -\frac{\partial q_i}{\partial x_i} + \sigma_{ji} \frac{\partial u_i}{\partial x_j} + \dot{Q}_s - \dot{F}_{s,\,i} u_i \tag{A.16}$$

The viscous/pressure work term in Eq. A.16 is as follows:

$$\sigma_{ji} \frac{\partial u_i}{\partial x_j} = \frac{1}{2}\left(-p - \frac{2}{3}\left(\mu \frac{\partial u_k}{\partial x_k}\right)\right) \delta_{ji} \left(\frac{\partial u_i}{\partial x_j} + \frac{\partial u_j}{\partial x_i}\right) + 2\mu e_{ij} e_{ij} \tag{A.17}$$

Neglecting dissipation by viscous forces in the above equation we get the following:

$$\sigma_{ji} \frac{\partial u_i}{\partial x_j} = -p \frac{\partial u_j}{\partial x_j} \tag{A.18}$$

Substituting Eq. A.18 into Eq. A.16 we get the following simplification:

$$\rho\frac{De}{Dt} + \dot{\rho}_s e_t + p\frac{\partial u_j}{\partial x_j} = -\frac{\partial q_i}{\partial x_i} + \dot{Q}_s - \dot{F}_{s,i}u_i \tag{A.19}$$

From the definitions of enthalpy, we have:

$$h = e + \frac{p}{\rho} \tag{A.20}$$

Casting total derivative of the internal energy in term of enthalpy we have:

$$\frac{De}{Dt} = \frac{Dh}{Dt} - \frac{1}{\rho}\frac{Dp}{Dt} + \frac{P}{\rho^2}\frac{D\rho}{Dt} \tag{A.21}$$

The continuity equation can be recast into the following form:

$$\frac{1}{\rho}\frac{D\rho}{Dt} = -\frac{\partial u_j}{\partial x_j} + \frac{\dot{\rho}_s}{\rho} \tag{A.22}$$

By invoking continuity equation, we can reduce the Eq. A.21 to the following:

$$\rho\frac{De}{Dt} = \rho\frac{Dh}{Dt} - \frac{Dp}{Dt} + \frac{P}{\rho}\left(-\frac{\partial u_j}{\partial x_j} + \frac{\dot{\rho}_s}{\rho}\right) \tag{A.23}$$

plugging Eq. A.23 into Eq. A.19 we have:

$$\rho\frac{Dh}{Dt} + p\frac{\dot{\rho}_s}{\rho} + \dot{\rho}_s e_t - \frac{Dp}{Dt} = -\frac{\partial q_i}{\partial x_i} + \dot{Q}_s - \dot{F}_{s,i}u_i \tag{A.24}$$

Invoking the zero-Mach number approximation (Eq. A.7), we can reduce the above equation to:

$$\rho\frac{Dh}{Dt} + p_0\frac{\dot{\rho}_s}{\rho} + \dot{\rho}_s e_t - \frac{\partial p_0}{\partial t} = -\frac{\partial q_i}{\partial x_i} + \dot{Q}_s - \dot{F}_{s,i}u_i \tag{A.25}$$

The total derivative for a calorific perfect gas can be reduced to the following

form invoking the perfect gas relations and the zero Mach number approximation:

$$\begin{aligned}
\rho\frac{Dh}{Dt} &= \rho\frac{DC_pT}{Dt} = \frac{\rho C_p}{R}\frac{D}{Dt}\left(\frac{p}{\rho}\right) \\
&= \frac{\rho C_p}{R}\frac{1}{\rho}\frac{Dp}{Dt} - \frac{\rho C_p}{R}\frac{p}{\rho^2}\frac{D\rho}{Dt} \\
&= \frac{\gamma}{\gamma-1}\frac{Dp}{Dt} - \frac{C_p}{R}\frac{p}{\rho}\left(-\frac{\partial\rho}{\partial t} + u_i\frac{\partial\rho}{\partial x_i}\right) \\
&= \frac{\gamma}{\gamma-1}\frac{Dp}{Dt} - \frac{\gamma}{\gamma-1}p\left(-\frac{\partial u_j}{\partial x_j} + \frac{\dot{\rho}_s}{\rho}\right) \\
&= \frac{\gamma}{\gamma-1}\frac{\partial p_0}{\partial t} + \frac{\gamma}{\gamma-1}p_0\frac{\partial u_j}{\partial x_j} - \frac{\gamma p_0}{\gamma-1}\frac{\dot{\rho}_s}{\rho}
\end{aligned} \tag{A.26}$$

On substituting Eq. A.26 into Eq. A.25 we have the following:

$$\left(\frac{\gamma}{\gamma-1}-1\right)\frac{\partial p_0}{\partial t} + \frac{\gamma p_0}{\gamma-1}\frac{\partial u_j}{\partial x_j} + \left(1-\frac{r}{r-1}\right)\frac{p_0\dot{\rho}_s}{\rho} + \dot{\rho}_s e_t = -\frac{\partial q_i}{\partial x_i} + \dot{Q}_s - \dot{F}_{s,i}u_i \tag{A.27}$$

On simplification we get:

$$\frac{\gamma}{\gamma-1}\frac{\partial p_0}{\partial t} + \frac{\gamma p_0}{\gamma-1}\frac{\partial u_j}{\partial x_j} - \frac{1}{\gamma-1}\frac{p_0\dot{\rho}_s}{\rho} + \dot{\rho}_s e_t = -\frac{\partial q_i}{\partial x_i} + \dot{Q}_s - \dot{F}_{s,i}u_i \tag{A.28}$$

On further re-arrangement we get:

$$\frac{\partial p_0}{\partial t} = (\gamma - 1)\left[\left(-\frac{\gamma p_0}{\gamma - 1}\frac{\partial u_j}{\partial x_j}\right) + \frac{1}{\gamma - 1}\frac{p_0 \dot{\rho}_s}{\rho} - \dot{\rho}_s e_t - \frac{\partial q_i}{\partial x_i} + \dot{Q}_s - \dot{F}_{s,\,i} u_i\right] \tag{A.29}$$

From continuity we have the following:

$$\frac{\gamma p_0}{\gamma - 1}\frac{\partial u_j}{\partial x_j} = \frac{\gamma p_0}{\gamma - 1}\frac{1}{\rho}\left(\frac{\partial \rho}{\partial t} + u_j \frac{\partial \rho}{\partial x_j} - \dot{\rho}_s\right) \tag{A.30}$$

On substituting Eq. A.30 in Eq. A.29 and some rearrangement we have the following for the dilatation term:

$$\frac{\partial u_j}{\partial x_j} = \frac{\gamma - 1}{\gamma p_0}\left[\frac{1}{\gamma - 1}\frac{\partial p_0}{\partial t} + \frac{1}{\gamma - 1}\frac{p_0 \dot{\rho}_s}{\rho} - \dot{\rho}_s e_t - \frac{\partial q_i}{\partial x_i} + \dot{Q}_s - \dot{F}_{s,\,i} u_i\right] \tag{A.31}$$

Heat flux in the above equation is:

$$q_i = -\kappa \frac{\partial T}{\partial x_i} \tag{A.32}$$

Substituting Eq. A.32 in Eq. A.31 we get the following for computing the dilatation term:

$$\frac{\partial u_j}{\partial x_j} = \frac{\gamma-1}{\gamma p_0}\left[\frac{1}{\gamma-1}\frac{\partial p_0}{\partial t} + \frac{1}{\gamma-1}\frac{p_0\dot{\rho}_s}{\rho} - \dot{\rho}_s e_t + \kappa\left(\frac{\partial^2 T}{\partial x^2} + \frac{\partial^2 T}{\partial y^2} + \frac{\partial^2 T}{\partial z^2}\right) + \dot{Q}_s - \dot{F}_{s,i}u_i\right] \quad \text{(A.33)}$$

So the final set of equations to be solved for the change in thermodynamic pressure and the corresponding dilatation term are given as follows:

$$\frac{\partial p_0}{\partial t} = (\gamma-1)\left[\frac{\gamma p_0}{\gamma-1}\frac{1}{\rho}\left(\frac{\partial \rho}{\partial t} + u_j\frac{\partial \rho}{\partial x_j} - \dot{\rho}_s\right) + \frac{p_0\dot{\rho}_s}{\rho} - \dot{\rho}_s e_t + \dot{Q}_s - \dot{F}_{s,i}u_i\right] \quad \text{(A.34)}$$

$$\frac{\partial u_j}{\partial x_j} = \frac{\gamma-1}{\gamma p_0}\left[\frac{1}{\gamma-1}\frac{\partial p_0}{\partial t} + \frac{1}{\gamma-1}\frac{p_0\dot{\rho}_s}{\rho} - \dot{\rho}_s e_t + \kappa\frac{\partial^2 T}{\partial x_i \partial x_i} + \dot{Q}_s - \dot{F}_{s,i}u_i\right] \quad \text{(A.35)}$$

There are several new terms appearing in the equations due to the presence of droplets which have to appropriately included. These are the fully resolved equations for energy and the filtered equations which are used for computations are arrived at in a similar procedure and are listed in Chapter II.

APPENDIX B

SEMI-IMPLICIT SCHEME FOR NON-STAGGERED GRIDS

A numerical method for integrating the Navier Stokes equations in the zero-Mach number limit earlier implemented and validated by Chakravarthy [64], is presented here. The time-integration is conducted using a two-step, semi-implicit, second order accurate fractional step method. A collocated grid system is used for the finite-difference spatial discretization of governing equations.

In fractional step methods, a split procedure is adopted. In the first step, the momentum equations are updated without the pressure gradient terms. The pressure is then obtained by using a Poisson equation which couples the momentum equation to the continuity equation. In the last step, the momentum equations are updated with the pressure gradient thereby, leading to a coupled solution. The means to obtain pressure, thus holds the key to fast convergence.

Unlike most fractional step methods that are formulated on staggered grids, the method here is formulated using a collocated (non-staggered) grid layout for variable definitions. The pressure-velocity decoupling that is common to collocated grid arrangements is overcome and strong elliptic coupling is achieved through a scheme that mimics the finite-volume formulation. A discussion on the spatial discretization schemes used for this coupling is presented following the time-integration scheme.

Time integration scheme

The trapezoidal (Crank-Nicholson) scheme is presented here for the zero-Mach number equations. All the terms in the governing equations (including the non-linear terms) are updated semi-implicitly in order to retain stability at both the inviscid and the Stokes limits.

Consider the continuity and the momentum equations in their non-conservation form.

$$\frac{\partial \rho}{\partial t} + u_j \frac{\partial \rho}{\partial x_j} + \rho \frac{\partial u_j}{\partial x_j} = 0 \tag{B.1}$$

$$\frac{\partial}{\partial t}(\rho u_i) + u_j \frac{\partial}{\partial x_j}(\rho u_i) + \rho u_i \frac{\partial u_j}{\partial x_j} = -\frac{\partial p}{\partial x_i} + \frac{\partial}{\partial x_j}(\tau_{ij}) \tag{B.2}$$

For convenience, the following notation is adopted henceforth.

$$A = -u_j \frac{\partial \rho}{\partial x_j} - \rho \frac{\partial u_j}{\partial x_j} \tag{B.3}$$

$$B_i = -u_j \frac{\partial}{\partial x_j}(\rho u_i) - \rho u_i \frac{\partial u_j}{\partial x_j} + \frac{\partial}{\partial x_j}(\tau_{ij}) \tag{B.4}$$

For simplicity, the additional subgrid stress is assumed to be included in τ_{ij}. Since the volumetric dilatation is explicitly obtained (from Eq. 2.3) and used in the above equations, conservation (divergence) forms can not be used in solving the zero-Mach number equations. This presents a difficulty in building a finite-volume scheme and hence a finite-difference scheme is used. The semi-implicit scheme produces the following difference equations.

$$\frac{\rho^{n+1} - \rho^{n}}{\Delta t} = \frac{1}{2}\left[A^{n} + A^{n+1}\right] \tag{B.5}$$

$$\frac{(\rho u_i)^{n+1} - (\rho u_i)^{n}}{\Delta t} = \frac{1}{2}\left[B^{n} + B^{n+1}\right] - \frac{\partial p}{\partial x_i}^{n+\frac{1}{2}} \tag{B.6}$$

The following two step iterative procedure is used to converge the solution at each time step.

$$\frac{\rho^{n+1} - \rho^{n}}{\Delta t} = \frac{1}{2}\left[A^{n} + A^{n+1}\right] \tag{B.7}$$

$$\frac{(\rho u_i)^{*} - (\rho u_i)^{n}}{\Delta t} = \frac{1}{2}\left[B^{n} + B^{n+1}\right] - \frac{\partial p}{\partial x_i}^{n+\frac{1}{2}} \tag{B.8}$$

followed by

$$\frac{(\rho u_i)^{n+1} - (\rho u_i)^{*}}{\Delta t} = -\frac{\partial p}{\partial x_i}^{n+\frac{1}{2}} \tag{B.9}$$

As usual, the pressure gradient couples the conservation equations for mass and momentum. Before solving for $(\rho u_i)^{n+1}$ in Eq. B.9, the pressure gradient is required. The pressure needs to be determined between the two steps of the split scheme (Eqs. B.7-B.9). An elliptic equation for the pressure is obtained by using the divergence operator on Eq. B.9.

$$\frac{\partial^2 p}{\partial x_k \partial x_k}^{n+\frac{1}{2}} = \frac{1}{\Delta t}\frac{\partial}{\partial x_i}\left[(\rho u_i)^{n+1} - (\rho u_i)^{*}\right] \tag{B.10}$$

The above equation is a second order approximation to the equation for pressure.

The equation for pressure and its second order accurate discrete form are shown below.

$$\frac{\partial^2 p}{\partial x_k \partial x_k} = -\frac{\partial^2}{\partial x_i \partial x_t}(\rho u_i) + \frac{\partial B}{\partial x_i} \tag{B.11}$$

$$\frac{\partial^2 p^{n+\frac{1}{2}}}{\partial x_k \partial x_k} = \frac{1}{\Delta t}\frac{\partial}{\partial x_i}\left[(\rho u_i)^{n+1} - (\rho u_i)^{*}\right] + \frac{1}{2}\frac{\partial}{\partial x_i}\left[B_i^{n} + B_i^{n+1}\right] \tag{B.12}$$

Using the semi-implicit trapezoidal updating procedure, a second order scheme is obtained without any complicated pressure updating. A Poisson equation is obtained for pressure unlike the higher order equations encountered in other formulations. The equation set B.7-B.9 is solved using a fixed point iteration. Initial estimates for the flow quantities at time step "n+1" can be obtained using forward extrapolation in time.

In case of reacting flows, species conservation equations also need to be integrated in time. These are handled in much the same way as the mass conservation equation, except that ρ is now replaced by species concentrations and the extra diffusion and destruction (/production) terms are also updated using a trapezoidal scheme. This procedure is followed here only in simulations where the scalar transport equations are solved using finite difference methods.

Spatial discretization

The finite-difference grid layout is identical to the finite-volume grid layout. The half points ([i+1/2,j,k], [i,j+1/2,k] etc.) and the grid points ([i,j,k], [i+1,j,k] etc.) on the finite-difference grid used here correspond respectively to grid cell faces and grid cell centers of a finite-volume grid.

Here, an upwind biased (QUICK) interpolation along the grid lines is used to obtained the required quantities at half points. The error involved in such interpolations does not affect the second order accuracy of the scheme except when using highly skewed grids. In such cases, a multi-dimensional upwind interpolation can be used.

Consider the terms in A as defined in the previous section. The volumetric dilatation (divergence of velocity field) is explicitly known. The remaining term is discretized as follows.

$$u_j \frac{\partial \rho}{\partial x_j} = u_j \frac{\partial \xi_k}{\partial x_j} \cdot \frac{\partial \rho}{\partial \xi_k} \tag{B.13}$$

where ξ_k is the coordinate on the computational domain. $\frac{\partial \xi_k}{\partial x_j}$ is the metric of transformation and is calculated using a second (or fourth) order finite-difference approximation.

The terms that account for the velocity acceleration due to advection and

volumetric dilatation in B_i are also transformed into computational coordinates as follows.

$$u_j \frac{\partial}{\partial x_j}(\rho u_i) - \rho u_i \frac{\partial u_j}{\partial x_j} = -u_j \frac{\partial \xi_k}{\partial x_j} \cdot \frac{\partial}{\partial \xi_k}(\rho u_i) - \rho u_i \frac{\partial u_j}{\partial x_j} \tag{B.14}$$

The volumetric dilatation is obtained explicitly in the zero Mach number approximation. So the second term on the right needs no differencing. The derivatives of ρ and ρu_i along the computational coordinate (required in last two equations) are evaluated using a finite-difference approximation that is at least third order accurate.

Central differencing of the convective terms is preferable since the truncation error involved would add to the dispersion of the solution and the numerical dissipation is relatively low.

In the current numerical method, the velocity discontinuities (across the vaporization zones) are better captured with out any destabilizing oscillations if an upwind biased approximation is used for the convective terms. The two requirements of a numerical scheme (for LES), low numerical dissipation and oscillation free flame zones are mutually conflicting. In order to cater to these two requirements, a switch, θ, is used for determining the spatial stencil for discretizations. For the exothermic/endothermic

flow simulations, the computational derivative in the convective term is computed as follows.

$$\frac{\partial}{\partial \xi} = \theta \frac{\partial}{\partial \xi_L} + (1-\theta)\frac{\partial}{\partial \xi_R} \tag{B.15}$$

where, subscripts "L" and "R" respectively denote the left biased and the right biased fifth order finite-difference approximations. θ of 0.5 produces a central difference approximation. θ is computed from the contravariant velocity $u_j \frac{\partial \xi_k}{\partial x_j}$ and is designed to be 0.5 in regions where the flow is sufficiently smooth. In regions of strong flow gradients, it is closer to 0 or 1 depending on the contravariant velocity direction, thus producing a upwind biased finite-difference approximation for the gradient. Given that the upwind biased finite-difference operators are at least fifth order accurate, better than second order accuracy is maintained at all times.

The diffusive terms are calculated using central difference approximations. For a variable q with diffusivity D_q, the diffusion term is approximated as follows.

$$\frac{\partial}{\partial x_k}\left[D_q \frac{\partial q}{\partial x_k}\right] = J\frac{\partial}{\partial \xi_n}\left[G_{mn} D_q \frac{\partial q}{\partial x_m}\right] \tag{B.16}$$

where, J is the jacobian of the transformation $J^{-1} = \det[(\partial x_i)/(\partial \xi_j)]$ and G_{kl} is called the mesh skewness tensor computed as follows.

$$G_{kl} = \frac{1}{J}\frac{\partial \xi_k}{\partial x_m} \cdot \frac{\partial \xi_l}{\partial x_m} \tag{B.17}$$

A generic second order, 19-point stencil (discussed in the next section) is used to discretize the Laplacian operator on the computational grid.

Poisson solver

The Poisson equation in curvilinear coordinates has the form:

$$\frac{\partial}{\partial \xi_j}\left[G_{ij}\frac{\partial p}{\partial \xi_j}\right] = -\frac{1}{\Delta t}\frac{\partial F_i}{\partial \xi_i} \tag{B.18}$$

$$F_i = \left[\frac{1}{J}\frac{\partial \xi_k}{\partial x_j}\left[(\rho u_i)^{n+1} - (\rho u_i)^{*}\right]\right] \tag{B.19}$$

F_i's are evaluated at the half points [(i+1/2,j,k), (i,j+1/2,k), (i,j,k+1/2)] using upwind-biased, third-order QUICK interpolations from the grid nodes. If a symmetric interpolation scheme is used, the source term (in the above equation) and subsequently

the pressure at a given point are independent of the velocities at that point. Further, if the pressure update in the corrector step also uses a central difference approximation for the pressure gradient, the velocity at a given point depends only on the pressure values at neighboring nodes and not on the pressure at that point itself. The velocity and pressure fields can completely be decoupled in space. When a non-symmetric interpolation scheme (like QUICK) is used, the decoupling is prevented since the source term in the Poisson equation, at a given location, depends on the momenta $(\rho u_i)^{n+1}$ and $(\rho u_i)^{*}$ at that location.

Note that the metrics $J^{-1}\frac{\partial \xi_i}{\partial x_j}, j = 1, 2, 3$ and $G_{ij}, j = 1, 2, 3$ are required at half points along the ξ_i line. A second order scheme is used to discretize the source term in the above equation.

$$\begin{aligned}\frac{\partial}{\partial \xi_m}(F_m) = {} & (F_1)_{i+\frac{1}{2}, j, k} - (F_1)_{i-\frac{1}{2}, j, k} \\ & + (F_2)_{i, j+\frac{1}{2}, k} - (F_2)_{i, j-\frac{1}{2}, k} \\ & + (F_3)_{i, j, k+\frac{1}{2}} - (F_3)_{i, j, k-\frac{1}{2}}\end{aligned} \tag{B.20}$$

where the indices outside of regular brackets denote the location on the computational domain. A finite-volume discretization results in exactly the same

expression for the source term. In a finite-volume sense, F_i can be viewed as a correction to the mass flux vector across grid cell faces (half points). This correction ensures mass conservation within a virtual finite-volume centered around each grid node. In constant density flows, the velocity field at the advancing time step is divergence free. In order to ensure this upon completion of the split scheme, the source term is calculated by setting the divergence of u_i^{n+1} to zero in the above equation.

For discretization of the Poisson equation, we define Y_i as $G_{mn}\frac{\partial p}{\partial \xi_n}$. The Laplacian of pressure in the computational domain can now be discretized as shown below.

$$\frac{\partial}{\partial \xi_m}\left[G_{mn}\frac{\partial p}{\partial \xi_n}\right] = (Y_1)_{i+\frac{1}{2},j,k} - (Y_1)_{i-\frac{1}{2},j,k} + (Y_2)_{i,j+\frac{1}{2},k} - (Y_2)_{i,j-\frac{1}{2},k} + (Y_3)_{i,j,k+\frac{1}{2}} - (Y_3)_{i,j,k-\frac{1}{2}} \tag{B.21}$$

Y_i's are computed using second-order central-difference approximations leading to a 19 point stencil for the Laplacian operator. A successive line over-relaxation (SLOR) scheme is used as a solution procedure along with a four level multigrid scheme to accelerate the convergence. It is found that after initial stages of evolution, multigrid is

not needed. It has also been observed that in high vaporization cases, point Jacobi is more efficient than other schemes.

Order to accuracy

The order of accuracy of the present scheme is determined here by simulating a flow with a known unsteady, analytical solution. The flow corresponds to the single mode decay of a two-dimensional periodic velocity field.

$$u = -\cos(x)\sin(y)\exp\left(-\frac{2t}{Re}\right) \tag{B.22}$$

$$v = \sin(x)\cos(y)\exp\left(-\frac{2t}{Re}\right) \tag{B.23}$$

$$p = -\frac{1}{4}[\cos(2x) + \cos(2y)]\exp\left(-\frac{4t}{Re}\right) \tag{B.24}$$

This flow has often been used to test the accuracy of numerical methods designed for simulating laminar flows. A cubical domain is considered for these simulations. The initial solution is advanced for 20 non-dimensional time units using various grid resolutions. The maximum error in the u-velocity was plotted against the number of grid points used along each direction. It was found in the logarithmic plot for the error a slope less than -2.0 indicating that the second order accuracy of the scheme is retained for long

simulation times.

While the order of accuracy test shows that the present scheme is second order accurate, the nature of the error is unknown. Dispersive errors lead to spurious high wavenumber modes and dissipative errors lead to artificial damping of the fluid dynamic eddies. In unsteady turbulent simulations, the dissipative errors should be kept minimal in order to capture the energy dynamics accurately and at the same time, the high wavenumber modes should not be severely affected by the dispersive error. The results from the stochastically forced isotropic turbulence simulations (described in chapter V) indicate that the current DNS/LES solver is numerically accurate to model all the resolved scales of interest.

REFERENCES

[1] Poinsot, T. (1996) "Using Direct Numerical Simulations to Understand Premixed Turbulent Combustion," Symp. (Intn.) on Combustion, 26, pp. 219-232.

[2] Menon, S. (2000) "Subgrid Combustion Modeling for Large-Eddy Simulations," International Journal of Engine Research (to appear).

[3] Menon, S. and Calhoon, W. (1996) "Subgrid Mixing and Molecular Transport Modeling for Large-Eddy Simulations of Turbulent Reacting Flows," Symp. (International) on Combustion, 26, 59-66.

[4] Calhoon, W.H. and Menon, S. (1996) "Subgrid Modeling for Reacting Large-Eddy Simulations," AIAA 96-0516, 34th AIAA Aerospace Sciences Meeting.

[5] Calhoon, W.H. and Menon, S. (1997) "Linear-Eddy Subgrid Model for Reacting Large-Eddy Simulations: Heat Release Effects," AIAA 97-0368, 35th AIAA Aerospace Sciences Meeting.

[6] Pope, S.B., (1985) "PDF Methods for Turbulent Reactive Flows," Prog. Energy Combust., Vol. 11, pp. 119-192.

[7] Anand, M. S. and Pope, S. B., (1987) "Calculations of Premixed Turbulent Flames by PDF Methods", Combustion and Flame, Vol. 67, pp. 127-142.

[8] Miller, P.L. and Dimotakis, P.E. (1996) "Measurements of Scalar Power Spectra in High Schmidt Number Turbulent Jets," Journal of Fluid Mechanics, Vol. 308, pp. 129-146.

[9] Buch, K.A. and Dahm, W.J.A. (1996) "Experimental study of the fine-scale structure of conserved scalar mixing in turbulent shear flows. Part 1. Sc>>1," Journal of Fluid Mechanics, Vol. 317, pp. 21-71.

[10] Buch, K.A. and Dahm, W.J.A., (1998) "Experimental study of the fine-scale structure of conserved scalar mixing in turbulent shear flows. Part 2. Sc~1," Journal of Fluid Mechanics, Vol. 364, pp. 1-29.

[11] Smith, T. M. and Menon, S., (1998) "Subgrid Combustion Modeling for Premixed Turbulent Flows," AIAA Paper No. 98-0242, 36th Aerospace Sciences Meeting and Exhibit.

[12] Chakravarthy, K. and Menon, S., (1999) “Modeling of Turbulent Premixed Flames in the Flamelet Regime,” Proceedings of the Turbulence and Shear Flow Phenomena, First International Symposium, Santa Barbara, CA, Eds. J. Eaton And S. Banerjee, Begell House, New York, pp. 185-194.

[13] Chakravarthy, K. and Menon, S., (2000) “Subgrid Modeling of Turbulent Premixed Flames in the Flamelet Regime,” Invited paper submitted to the special issue of Flow, Turbulence and Combustion.

[14] Menon, S. and Jou, W.-H. (1991) “Large-eddy Simulations of Combustion Instability in an Axisymmetric Ramjet Combustor,” Combustion Science and Technology, Vol. 75, pp. 53-72.

[15] Smith, T. M. and Menon, S. (1996) “The structure of Premixed Flames in a Spatially Evolving Turbulent Flame,” Combustion Science and Technology, Vol. 119(1-6), pp. 77-106.

[16] Smith, T. M. (1998) “Unsteady Simulations of Turbulent Premixed Reacting Flows,” Ph. D. Thesis, Georgia Institute of Technology.

[17] Kim, W.-W., Menon, S. and Mongia, H. (1999) “Numerical Simulations of Reacting Flows in a Gas Turbine Combustor,” Combustion Science and Technology, Vol. 143, pp. 25-62.

[18] Menon, S. and Kim, W.-W. (1996) “High Reynolds Number Flow Simulations using the Localized Dynamic Subgrid-Scale Model,” AIAA 96-0425, 34th AIAA Aerospace Sciences Meeting.

[19] Kim, W.-W. and Menon, S. (1999) “A New Incompressible Solver for Large-Eddy Simulations,” International Journal of Numerical Methods in Fluids, Vol. 31, pp. 983-1017.

[20] Erlebacher, G., Hussaini, M. Y., Speziale, C. G. and Zang, T. A. (1992) “Toward the Large-Eddy Simulation of Compressible Turbulent Flows,” Journal of Fluid Mechanics, Vol. 238, pp. 155-185.

[21] Germano, M., Piomelli, U., Moin, P. and Cabot, W. H. (1991) “A Dynamic Subgrid-scale Eddy Viscosity Model,” Physics of Fluids A, Vol. 3(11), pp. 1760-1765.

[22] Smagorinsky J. (1963) “General Circulation Experiments with the Primitive Equations,” Monthly Weather Review, Vol. 91 (3), pp. 99-164.

[23] Oefelein, J. C. and Yang, V. (1996) “Analysis of Transcritical Spray Phenomena in Turbulent Mixing Layers,” AIAA 96-0085, 34th AIAA Aerospace Sciences Meeting, Reno, NV, Jan. 15-18.

[24] Wang, Q. and Squires, K. D. (1996) “Large Eddy Simulation of Particle Laden Turbulent Channel Flow,” Phys. Fluids, 8(5), pp. 1207-1223.

[25] Chen, X.-Q. and Pereira, J. C. F. (1998) “Computation of Particle-Laden Turbulent Gas Flows Using Two Dispersion Models,” AIAA Journal, Vol. 36, No. 4, pp. 539-546.

[26] Sommerfeld, M. (1994) “The Importance of Detailed Measurements for the Validation of Numerical Models and Methods for Dispersed Two-Phase Flows,” Experimental and Computational Aspects of Multiphase Flow CFD Codes, ASME, FED-Vol. 180.

[27] Faeth, G. M. (1983) “Evaporation and Combustion of Sprays,” Progress in Energy and Combustion Science, Vol. 9, pp. 1-76.

[28] Faeth, G. M. (1987) “Mixing, Transport and Combustion in Sprays,” Prog. Energy Combust. Sci., Vol. 13, pp. 293-345.

[29] Williams, F. A. (1985) “Combustion Theory,” 2nd Edition, Benjamin/Cummings.

[30] Crowe, C., Sommerfeld, M. and Tsuji, Y. (1996) “Multiphase Flows with Droplets and Particles,” CRC Press.

[31] Druzhinin, O. A. and Elgobashi, S. (1998) “Direct Numerical Simulations of Bubble-Laden Turbulent Flows Using the Two-Fluid Formulation,” Phys. of Fluids, Vol. 10 (3), pp. 685-697.

[32] Mostafa, A. A. and Mongia, H. C. (1983) “On the Modeling of Turbulent Evaporating Sprays: Eulerian versus Lagrangian Approach,” Int. J. of Heat Mass Transfer, Vol. 30, pp. 2583-2593.

[33] Amsden, A. A., O’Rourke, P. J., and Butler, T. D. (1989) “KIVA-II - A Computer Program for Chemically Reactive Flows with Sprays,” LA-11560-MS, Los Alamos National Laboratory.

[34] Chen, K.-H., Fricker, D., Lee, J. and Moder, J. (1998) “ALLSPD-3D User Guide,” Turbomachinery and Propulsion Systems Division, NASA Lewis Research Center.

[35] Mashayek F. (1998) “Droplet-Turbulence Interactions in Low-Mach-Number Homogeneous Shear Two-Phase Flows,” Journal of Fluid Mechanics, Vol. 367, 163-203.

[36] Boivin, M., Simonin, O. and Squires, K. D. (1998) “Direct Numerical Simulation of Turbulence Modulation by Particles in Isotropic Turbulence,” J. Fluid Mech., Vol. Elgobashi, S. E. and Truesdell, G. C. (1992) “Direct Simulation of Particle Dispersion in a Decaying Isotropic Turbulence,” Journal of Fluid Mechanics, Vol. 242, 655-700.

[37] Miller, R. S. and Bellan, J. (2000) “Direct Numerical Simulation and Subgrid Analysis of a Transitional Droplet Laden Mixing Layer,” Physics of Fluids, Vol. 12(3), pp. 650-671.

[38] Squires, K. D., and Eaton, J. K. (1990) “Particle Response and Turbulence Modification in Isotropic Turbulence,” Phys. Fluids A, Vol. 2 (7), 1191-1203.

[39] Squires, K. D., and Eaton, J. K. (1991) “Measurements of Particle Dispersion Obtained from Direct Numerical Simulations of Isotropic Turbulence,” Journal of Fluid Mechanics, Vol. 226, 1-35.

[40] Elgobashi, S. E. and Truesdell, G. C. (1992) “Direct Simulation of Particle Dispersion in a Decaying Isotropic Turbulence,” Journal of Fluid Mechanics, Vol. 242, 655-700.

[41] Elgobashi, S. E. and Truesdell, G. C. (1993) “On the Two-way Interaction Between Homogeneous and Dispersed Solid Particles. I: Turbulence Modification,” Phys. Fluids A, Vol. 5 (7), 1790-1801.

[42] Elgobashi, S. E. and Truesdell, G. C. (1994) “On the Two-way Interaction Between Homogeneous and Dispersed Solid Particles. II: Particle Dispersion,” Phys. Fluids A, Vol. 6 (3), 1405-1407.

[43] Lazaro, B. J., and Lasheras, J. C. (1992) “Particle Dispersion in the Developing Free Shear Layer. Part 1. Unforced Flow,” J. Fluid Mech., Vol. 235, pp. 143-178.

[44] Lazaro, B. J., and Lasheras, J. C. (1992) “Particle Dispersion in the Developing Free Shear Layer. Part 2. Forced Flow,” J. Fluid Mech., Vol. 235, pp. 179-221.

[45] Martin, J. E. and Meiburg, E. (1994) “The Accumulation and Dispersion of Heavy Particles in Forced Two-dimensional Mixing Layers. I. The Fundamental and Subharmonic Cases,” Phys. Fluids, Vol. 6 (3), pp. 1116-1132.

[46] Hishida, K., Ando, A. and Maeda, M. (1992) “Experiments on Particle Dispersion in a Turbulent Mixing Layer,” Int. Journal of Multiphase Flow, Vol. 18, No. 2, pp. 181-194.

[47] Menon, S. and Pannala, S. (1998) “Subgrid Combustion Simulations of Reacting Two-Phase Shear Layers,” AIAA Paper No. 98-3318, 34th AIAA/ASME/SAE/ASEE Joint Propulsion Conference and Exhibit, Cleveland, OH.

[48] Pannala, S., Henry, W. J., Kim, W.-W, and Menon, S. (1999) “Large-Eddy Simulation of Reacting Sprays,” 3rd ASME/JSME Joint Fluids Engineering Conference, San Francisco, CA.

[49] McMurtry, P. A., Riley, J. J., and Metcalfe, R. W. (1989) “Effects of Heat Release on the Large-scale Structure in Turbulent Mixing Layers,” Journal of Fluid Mech., Vol. 199, pp. 297-332.

[50] Maxey, M. R. and Riley, J. J. (1983) “Equations of Motion for a Small Rigid Sphere in a Nonuniform Flow,” Phys. of Fluids, Vol. 26, pp. 883.

[51] Gosman, A. D. and Ioannides, E. (1981) “Aspects of Computer Simulation of Liquid Fueled Combustors,” AIAA Paper No. 81-0323.

[52] Faeth, G. M. (1977) “Current Status of Droplet and Liquid Combustion,” Prog. Energy Combust. Sci., Vol. 3, pp. 191-224.

[53] Yuen, M. C. and Chen, L. W. (1976) “On Drag of Evaporating Liquid Droplets,” Combust. Sci. Tech., Vol. 14, pp. 147-154.

[54] Faeth, G. M., and Lazar, R. S. (1971) “Fuel Droplet Burning Rates in a Combustion Gas Environment,” AIAA Journal, Vol. 9, pp. 2165-2171.

[55] Chen, K-H. and Shuen, J.-S. (1993) “A Coupled Multi-Block Solution Procedure for Spray Combustion in Complex Geometries,” AIAA 93-0108, 31st AIAA Aerospace Sciences Meeting, Reno, NV.

[56] Wang, W. and Squires, K. D. (1998) “Transport of Heavy Particles in a Three-Dimensional Mixing Layer,” Journal of Fluids Engineering, Vol. 120, pp. 613-620.

[57] Frankel, S. H., Adumitroaie, V., Madnia, C. K., and Givi, P. (1993) “Large Eddy Simulation of Turbulent Reacting Flows by Assumed pdf Methods,” in Engineering Application of Large Eddy Simulations, Ragab, S. A., and Piomelli, U., ed., ASME, FED-Vol. 162, New York, pp. 81-101.

[58] Gao, F., and O'Brien, E. E. (1993) “A Large-Eddy Simulation Scheme for Turbulent Reacting Flows,” Physics of Fluids A, Vol. 5, pp. 1282-1284.

[59] Dimotakis, P. E. (1989) “Turbulent Free Shear Layer Mixing,” AIAA Paper 89-0262, 27th Aerospace Sciences Meeting, Reno, Nevada.

[60] Pope, S. B. (1979) “The Statistical Theory of Turbulent Flames,” Philosophical Trans. of the Royal Soc. of London, Vol. 291, pp. 529-568.

[61] Kerstein, A. R. (1989) “Linear-Eddy Model of Turbulent Transport II. Application to Shear Layer Mixing,” Combustion and Flame, Vol. 75, pp. 397-413.

[62] Kerstein, A. R. (1992) “Linear-Eddy Model of Turbulent Transport 4. Structure of Diffusion-Flames,” Comb. Sci. and Tech., Vol. 81, pp.75-96.

[63] Kerstein, A. R. (1991) “Linear-eddy Modelling of Turbulent Transport. Part 6. Microstructure of Diffusive Scalar Mixing Fields,” J. Fluid Mech, V 231, pp. 361-394.

[64] Chakravarthy, V. K. (2000) “Stochastic Subgrid Modeling of Premixed Flames,” Ph. D. thesis, Georgia Institute of Technology.

[65] Kerstein, A. R. (1991) “Linear-eddy Modelling of Turbulent Transport. Part 5. Geometry of Scalar Interfaces,” Physics of Fluids A, V 3(5), pp. 1110-1114.

[66] McMurtry, P., Gansauge, T., Kerstein, A. R., and Krueger, S. K. (1993) “Linear Eddy Simulations of Mixing in a Homogeneous Turbulent Flow,” Phys. of Fluids, Vol. 5, No. 4, pp. 1023-1034.

[67] Yeung, P. K. and Pope, S. B. (1989) “Lagrangian Statistics from Direct Numerical Simulations of Isotropic Turbulence,” J. Fluid Mechanics, Vol. 207, pp. 531-586.

[68] Eswaran, V. and Pope, S. B. (1988) “An Examination of Forcing in Direct Numerical Simulations of Turbulence,” Computers and Fluids, Vol. 16, No. 3, pp. 257-278, 1998.

[69] Comte-Bellot, G. and Corrsin, S. (1971) “Simple Eulerian Time Correlation of Full- and Narrow-Band Velocity in Grid-Generated, ’Isotropic’ Turbulence” J. Fluid Mech., Vol. 48, pp. 273-337.

[70] Kerr, R. M. (1985) “Higher-Order Derivative Correlations and the Alignment of Small-Scale Structures in Isotropic Numerical Turbulence,” J. Fluid Mech., Vol. 153, pp. 31-58.

[71] Van Atta C. W. and Chen W. Y. (1969) “Measurements of Spectral Energy Transfer in Grid Turbulence,” J. Fluid Mech., Vol. 38, pp. 743-763.

[72] Metcalfe, R. W., Orszag, S. A., Brachet, M. E., Menon, S., and Riley, J. J. (1987) "Secondary Instability of a Temporally Growing Mixing Layer," J. Fluid Mech., Vol. 184, pp. 207-243.

[73] Ling, W., Chung, J. N., Troutt, T. R., and Crowe, C. T. (1997) "Numerical Simulation of Particle Dispersion in a Three-dimensional Temporal Mixing Layer," 1997 ASME Fluids Engineering Division Summer Meeting, Vancouver.

[74] Bell, J. H. and Mehta, R. D. (1990) "Development of a Two-Stream Mixing Layer from Tripped and Untripped Boundary Layers," AIAA Journal, Vol. 28, No. 12, pp. 2034-2042.

[75] Chen, X.-Q. and Pereira, J. C. F. (1994) "Comparison of the Various Particle Dispersion Models in Plane Mixing Shear Layers," Numerical Methods in Multiphase Flows, FED-Vol. 185, ASME, pp. 217-225.

[76] Oster, D. and Wygnanski, I. (1982) "The Forced Mixing Layer between Parallel Streams," J. Fluid Mechanics, Vol. 123, pp. 91-130.

[77] Wilson, R. V. and Demuren, A. O. (1994) "Numerical Simulation of Two-dimensional Spatially-Developing Mixing Layers," ICASE Report No. 94-32, NASA Contractor Report 194911.

[78] Schwer, D. A., Tsuei, H.-H. and Merkle, C. L. (1995) "Computation and Validation of Spatially Developing Reacting Mixing Layers," AIAA 95-0261, 33rd Aerospace Sciences Meeting and Exhibit, Reno, NV.

[79] Schwer, D. A. (1999) "Numerical Study of Unsteadiness in Non-reacting and Reacting Mixing Layers," Ph. D. thesis, Pennsylvania State University.

[80] Chen, M., Kontomaris, K. and McLaughlin, J. B. (1998a) "Direct Numerical Simulation of Droplet Collisions in a Turbulent Channel Flow. Part I: Collision Algorithm," International Journal of Multiphase Flow, vol. 24 n 7, pp. 1079-1103.

[81] Chen, M., Kontomaris, K. and McLaughlin, J. B. (1998b) "Direct Numerical Simulation of Droplet Collisions in a Turbulent Channel Flow. Part II: Collision Rates," International Journal of Multiphase Flow, vol. 24 n 7, pp. 1105-1138.

[82] Georjon, T. L. and Reitz, R. D. (1999) "Drop-shattering Collision Model for Multidimensional Spray Computations," Atomization and Sprays, Vol. 9, No. 9, pp. 231-254.

[83] Mundo, C., Tropea, C. and Sommerfeld, M. (1997) “Numerical and Experimental Investigation of Spray Characteristics in the Vicinity of a Rigid Wall,” Experimental Thermal and Fluid Science, Vol. 15, pp. 228-237.

[84] Shirolkar, J. S., Coimbra, C. F. M. and McQuay, M. Q. (1996) “Fundamental Aspects of Modeling Turbulent Particle Dispersion in Dilute Sprays, Prog. Energy Combust. Sci., Vol. 22, pp. 363-399.

[85] Tong, A. Y. and Sirignano, A. Y. (1986) “Multicomponent Transient Droplet Vaporization with Internal Circulation: Integral Equation Formulation and Approximate Solution,” Numerical Heat Transfer, vol. 10, pp. 253-278.

[86] Bellan, J. and Harstad, K. (1987) “The Details of the Convective Evaporation of Dense and Dilute Clusters of Drops,” Int. J. Heat and Mass Transfer, vol. 30, No. 6, pp. 1083-1093.

VITA

Sreekanth Pannala was born in Hyderabad, India on October 20, 1971. He completed schooling at the Bharatiya Vidya Bhavans Public High School with the highest aggregate in the All India Senior School Certificate examination, 1989. He earned a bachelors degree in Aerospace Engineering at the Indian Institute of Technology, Kharagpur in May 1993 with Honors. He then joined the graduate program in Aerospace Engineering at Georgia Institute of Technology in September 1993 and graduated with a Master of Science degree in Aerospace Engineering in December, 1994. Since then, he has pursued doctoral research under the guidance of Professor Suresh Menon. He has been working as Post-graduate Research Fellow at Oak Ridge National Labs, Oak Ridge since March, 1999. He is a member of the AIAA and ASME.